Université de Montréal

To Salt or Not to Salt: Three MALDI-TOF IMS Protocols Where (De)Salting Proved Essential

Par

Ethan Yang

Département de chimie, Faculté des arts et des sciences

Thèse présentée en vue de l'obtention du grade de doctorat (Ph.D.) en chimie

Mai 2020

Université de Montréal

Département de chimie, Faculté des arts et des sciences

Cette thèse intitulée

To Salt or Not to Salt: Three MALDI-TOF IMS Protocols Where (De)Salting Proved Essential

Présenté par
Ethan Yang

A été évalué(e) par un jury composé des personnes suivantes

Prof. Pierre Thibault
Président-rapporteur

Prof. Pierre Chaurand
Directeur de recherche

Prof. Karen Waldron
Membre du jury

Prof. Kevin Schey
Examinateur externe

Résumé

Présentement, la désorption ionisation laser assistée par la matrice (MALDI) est la méthode d'ionisation préférentielle pour étudier les lipides par l'imagerie par spectrométrie de masse (IMS). Bien qu'il existe les matrices spécifiques aux lipides, tel que la 1,5-DAN pour les phospholipides et la 2,5-DHB pour les triacylglycérols, il est toujours nécessaire d'augmenter la sensibilité de cette technique pour les échantillons atypiques ou certaines classes de lipides.

Dans la première étude, nous avons amélioré la sensitivité pour les phospholipides sur les tubes de Malpighi de mouches prélevés par microdissection dans un tampon physiologique à base de sodium et potassium. Un protocole de lavage à deux étapes a était trouvé favorable : un premier rinçage dans le glycérol suivi d'un second rinçage dans l'acétate d'ammonium. Ce protocole permet de réduire au maximum la présence de sels sans délocalisation notoire des phospholipides. La détection et l'imagerie des phospholipides en ionisation négative et positive ont suggéré une distribution uniforme sur toute la longueur des tubes. Ces résultats ont été comparés à ceux obtenus sur des sections tissulaires minces de mouche entière acquis avec les deux polarités. Néanmoins, la structure tridimensionnelle complexe des tubes rénaux suggère que la microdissection est l'approche la plus favorable pour en étudier leur lipidome.

Dans la deuxième étude, nous avons déterminé que l'addition de formate d'ammonium (AF) peut améliorer la détection des gangliosides par IMS dans le cerveau. Curieusement, il est nécessaire de rincer l'échantillon dans une solution d'AF avant l'addition de ce même sel suivit d'une conservation de l'échantillon dans un congélateur pendant 24 heures après la déposition de la matrice afin d'obtenir la meilleure augmentation de sensibilité. En moyenne, cette approche a permis d'augmenter l'intensité d'un facteur dix avec trois fois plus d'espèces de gangliosides détectées. De plus, malgré l'étape de lavage, nous n'avons pas observé la délocalisation des

gangliosides puisqu'il est toujours possible d'obtenir les résultats d'IMS de qualité avec une résolution spatiale de 20 µm.

Finalement, nous avons établi que le nitrate d'argent permet l'analyse des oléfines par IMS, en particulier du cholestérol. En optimisant le protocole de déposition par nébulisation, il est possible de générer une couche mince et homogène de nitrate d'argent ce qui rend la possibilité d'effectuer l'IMS à haute résolution spatiale, jusqu'à 10 µm, sans perte de qualité comparativement aux autres approches publiées.

L'ensemble de ce travail démontre l'effet du sel sur la sélectivité et la sensibilité pour cibler les familles de lipides désirées, ce qui nécessite les études ultérieures sur le rôle de ces sels lors du processus de la désorption-ionisation.

Mots clés : MALDI, imagerie par spectrométrie de masse, lipidomique, sel, optimisation, ganglioside, phospholipide, cholestérol, tube de Malpighi

Abstract

Matrix-assisted laser desorption/ionization imaging mass spectrometry (MALDI IMS) is currently the ionization method of choice for elucidating the spatial distribution of lipids on thin tissue sections. Despite the discovery of lipid friendly matrices such as 1,5-DAN for phospholipids and 2,5-DHB for triacylglycerols, there is a continued need to improve sensitivity.

In the first study, we improved the overall sensitivity for phospholipids of entire fly Malpighian tubules microdissected in PBS with a two-step wash in glycerol followed by ammonium acetate that removed the bulk of the salt with minimal species delocalization and tubule displacement. We were able to detect phospholipids in both positive and negative ion modes and revealed an even distribution of most phospholipids along the length of this organ. We compared the method to the results from whole body fly sections acquired in dual-polarity mode at the same spatial resolution and found it to be more suitable for studying the tubules because of the complex three-dimensional structure of this organ within the fly.

In the second study, we observed a marked improvement in ganglioside signals on mouse brain tissue sections with ammonium salt addition. Specifically, when the sample was first desalted in a low concentration ammonium formate solution, spray-coated with the same salt, coated with matrix and finally left in the freezer overnight before data acquisition, we observed an average overall improvement in ganglioside signal intensity by ten-fold and the number of species detected by three-fold. This method also did not affect the spatial distribution of the gangliosides, as high spatial resolution IMS results acquired at 20 μm showed no species delocalization.

Finally, we sought to determine if salts could be employed directly as matrices. In this work, we tested silver-based metal salts and discovered that spray depositing silver nitrate alone is a viable method for the IMS detection of olefins, particularly cholesterol. With the optimized dry

spray parameter, the overall deposition is homogeneous and composed of microscopic salt crystals that allow for high spatial resolution IMS down to 10 μm while maintaining acceptable overall signal quality comparable to that of previously published protocols.

Overall, this thesis demonstrates we can manipulate the local salt distribution to influence the sensitivity and selectivity to target specific lipid subfamilies, opening the door for future research to understanding the role salts play during the laser desorption/ionization process.

Keywords: MALDI, Imaging Mass Spectrometry, Lipidomics, Salt, Optimization, Ganglioside, Phospholipid, Cholesterol, Malpighian Tubules, Brain

Table of Contents

List of Tables

List of Figures

Abbreviations

9AA:	9-Aminoacridine
AA:	Arachidonic Acid
ACN:	Acetonitrile
Ag:	Silver
AgAc:	Silver Acetate
AgLDI:	Silver-Assisted Laser/Desorption Ionization
$AgNO_3$:	Silver Nitrate
AmA:	Ammonium Acetate
AmB:	Ammonium Bicarbonate
AmF:	Ammonium Formate
Cer:	Ceramide
CHO:	Cholesterol
Da:	Dalton
1,5-DAN:	1,5-Diaminonapthalene
DG:	Diacylglyceride
DHA:	Docosahexaenoic Acid
2,5-DHB:	2,5-Dihydroxybenzoic Acid
2,6-DHA:	2,6-Dihydroxyacetophenone
2,5-DHA:	2,5-Dihydroxyacetophenone
CHCA:	α-Cyano-4-hydroxycinnamic
SA:	Sinapinic Acid
EtOH:	Ethanol

FA:	Fatty Acid
GA:	Asialoganglioside
GD:	Disialoganglioside
GG:	Gangliosides
GL:	Glycerolipids
GM:	Monosialoganglioside
GP:	Pentasialoganglioside
GQ:	Quadrosialoganglioside
GT:	Trisialoganglioside
H&E:	Hematoxylin and Eosin Staining
IMS:	Imaging Mass Spectrometry
ITO:	Indium Tin Oxide
LA:	Linoleic Acid
LDI:	Laser/Desorption Ionization
m/*z*:	Mass-to-Charge Ratio
MALDI:	Matrix-Assisted Laser/Desorption Ionization
MeOH:	Methanol
MS/MS:	Tandem Mass Spectrometry
MS:	Mass Spectrometry
MT:	Malpighian Tubule
MBT:	2-Mercaptobenzothiazole
NEG:	Negative Ionization Mode
nH:	Norharmane
OA:	Oleic Acid

PA:	Phosphatidic Acid
PBS:	Phosphate-Buffered Saline
PBT:	Phosphate-Buffered Saline with 0.1% Tween
PC:	Phosphatidylcholine
PE:	Phosphatidylethanolamine
PI:	Phosphatidylinositol
PL:	Phospholipid
POS:	Positive Ionization Mode
PS:	Phosphatidylserine
S/N:	Signal-to-Noise Ratio
SM:	Sphingomyelin
SP:	Sphingolipid
ST:	Sterol lipid
TFA:	Trifluoroacetic Acid
TG:	Triacylglyceride
TOF/TOF-MS:	Tandem TOF Mass Spectrometry
TOF:	Time-of-Flight

To our never-ending thirst for answers.

Acknowledgements

Cette aventure a commencé le 12 mars, 2015, cinq ans avant le confinement qui nous a tous forcé de rester chez nous pendant plus que deux mois. Nearly one year had passed since receiving my bachelor's degree from McGill University and I was jobless. Having received rejection letters from all medical schools I had applied for and only a few thousand dollars left in my bank accounts, I frantically applied for jobs so that I would not end up penniless. Back when Facebook was still the thing, Dawn discovered the 1st (and to this day, the only) McGill Chemistry Career Fair hosted by then Dean of Science, Prof. Martin Grant, at Thomson House on McTavish. An hour before the fair, Dawn and I were lounging in the McSWAY office on the 6th floor of the SSMU Building. Relaxed at first, I refused to leave the comfort of the beach chair when it became time to leave for the event. I was nervous. What was a biochemist doing in a chemistry career fair? Would I find any appropriate opportunities? Had I even the qualifications? Never mind that, Dawn reminded me, there was free pizza and drinks, as she shooed me away and up the hastily re-paved McTavish. I obediently obliged. Good thing, too, because I had left with a happy belly and a bright future.

Maintenant que le déconfinement se déroule pas à pas, ma nouvelle aventure débutera bientôt. Five years later, I am once again faced with the same dilemma, with even more possibilities than before. Indeed, beyond the specialized knowledge I gained in imaging mass spectrometry, I have also developed invaluable life skills in time management, verbal and written communication, and teamwork. While at first it may seem my options narrowed, upon introspection, I believe my career prospects have widened. I was fortunate to not have signed up to work in a fire pit, as some PhD studies could be, though I did have my fair share of crises to manage. I am grateful to have trained under a passionate and insightful supervisor who provided the necessary guidance along the way. I am certainly thankful to the seniors before me who led the way and the juniors after me

who will continue our great work. I am also blessed to have had a constant beacon of support along the way.

Thank you, Pierre, for taking that leap of faith in a biochemistry major and nurturing him into an analytical chemist. Merci, Martin, de m'avoir guidé dès ma première journée au laboratoire tout en français, même si mon niveau de français était pourri. Thanks, Heath, for your constant help with my data analytical needs, even to this very day. Merci, Nidia et Elisabeth, pour tous ce que vous m'avez enseigné en MS. Merci, Carine, pour m'avoir introduit à un laboratoire de chimie organique et de me conseiller. Merci, Sibylle, pour ton amitié et de m'avoir beaucoup aidé pour le cours CHM 2971. Danke, Timon, for the talks over beer that has certainly alleviated some of the necessary stress. Thank you to Let's Talk Science for keeping me inspired about science and giving the chance to develop my soft skills. Merci, Julie, Baptiste et Khalid, les trois stagiaires que j'ai eu la chance de diriger. Merci, Frédéric, pour avoir entrepris la maintenance du laboratoire quand je suis parti pour un stage. Je te souhaite le meilleur dans le nouvel espace au campus MIL avec Zari et Rachel. Thanks, Jackie, for the weekly check-ins that disciplined me while writing this thesis. Thanks, Liv, for the continued friendship and mentorship eight years and counting! 還有在台灣的那些好友們，希望你們都能平安、快樂、發論文順利畢業。在此也要感謝我的父母親從小到大不斷的陪伴還有嚴格的培養，我會繼續努力的！ Thank you, Zach and Caleb, for putting up with me for more than two decades. And of course, thank you, Dawn, for your unwavering support and relentless fun. I would not have made it this far without you and would love for you to be with me until the end. Merci aux travailleuses et travailleurs de la ligne de front. Finally, thank you to everyone else who I have forgotten or not named but have, one way or another, shaped me into who I am. Whatever the future holds, equipped with a PhD, I am more than prepared to meet these challenges thanks to each and every one of you.

Chapter 1: Introduction

1.1. What is Mass Spectrometry?

A little over a century ago, Sir Joseph J. Thomson, with the help of his assistant Francis W. Aston, developed a "positive ray method" that could "determine the masses of all the particles" of a cathode ray[1]. In this set-up, charged ions were sent traveling across a metal tube in the presence of parallel electric and magnetic fields towards a photographic plate at the end of the tube. The ions followed parabolic trajectories and marked distinctive bands on specific regions of the photographic plate respective of their mass-to-charge ratio in this environment[1]. This rudimentary instrument, widely recognized as the first mass spectrometer, provided the evidence for isotopes of neon and gave rise to the field of mass spectrometry (MS)[1].

Since this seminal publication in 1913, new ionization methods pushed MS into scientific relevance. The introduction of electron impact (EI) in 1918 by Dempster and chemical ionization (CI) in 1966 by Munson and Field provided powerful and complementary methods to analyze and identify small organic compounds[2-6]. The combination of inductively coupled plasma (ICP) to MS in 1980 by Houk *et al.* extended MS into the analysis of elemental and trace metals[7, 8]. Soon, the arrival of "soft" ionization techniques, electrospray ionization (ESI) in 1984 from Yamashita and Fennand and matrix-assisted laser/desorption ionization (MALDI) in 1988 from Karas and Hillenkamp, opened MS to the world of biomedical research[9-11]. Continuous innovations in mass analyzers further advanced the technical capabilities of MS. These include the double-focusing sector instruments such as the Nier-Johnson[12, 13], the small and versatile quadrupole[14] that is most often configured as a triple quadrupole (QqQ)[15, 16], the high mass resolving power Fourier-transform ion cyclotron resonance (FT-ICR) ion traps[17] and the orbitrap[18], and of course, the ultra high mass analyzer time-of-flight (TOF)[19, 20]. Consequently, MS has now become an inseparable part of our society, continually keeping us safe at airports[21], accurately identifying bacterial

infections[22, 23], regularly testing athletes for illegal doping[24], meticulously revealing clues of our past civilizations[25], systematically elucidating complex mechanisms behind countless diseases[26], cautiously leading the fight against the current opioid crisis[27, 28], and even continuously uncovering answers about other planets in our solar system[29].

1.1.1. The Anatomy of a Mass Spectrometer

From the very first to the latest, all mass spectrometers contain these four essential main components: an ionization source, a mass analyzer, a detector and a data recording system (**Figure 1-1**). Samples are introduced either continuously or in pulses into the source where they undergo ionization as gas phase molecules. These charged analytes enter the mass analyzer and are separated based on their mass-to-charge ratio (*m/z*). Once separated, the ions are released towards the detector, which translates the charge induced or the current produced by the ion hitting its surface into a mass spectrum that is displayed through instrument specific software on a computer. These main components are usually physically distinct. However, some mass analyzers can also act as the detector, such as FT-ICRs, in which case the ions are not sacrificed during detection[17].

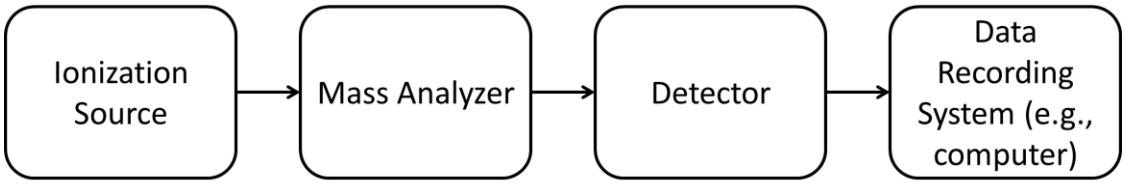

Figure 1-1: The Four Main Components of a Standard Mass Spectrometer. Mass spectrometers are composed of four main components: an ionization source, a mass analyzer, a detector and a data recording system.

Typically, the analysis of complex samples is preceded by a separation technique before mass spectral analysis. Currently, the two most popular approaches are gas chromatography (GC) and liquid chromatography (LC). In GC, vaporized compounds are separated along a long column based on their interaction with the stationary phase, while in LC, compounds in a liquid mixture

are separated on a much shorter column based on their interaction with both the stationary and mobile phase. High-performance liquid chromatography (HPLC) and ultra-performance liquid chromatography (UPLC) are the most popular LC techniques owing to their efficiency in separating samples and the large selection of analytical columns that cover nearly all separation needs. When small quantities are analyzed, nano-LC[30] and capillary electrophoresis (CE)[31], which separates ions based on their electrophoretic mobility under an applied electric field, are called upon. In cases where sample preseparation is insufficient or impossible, ion mobility spectrometry can provide the extra degree of separation post ionization. First described by McDaniel[32], ion mobility separates ions based on their drift velocity in the presence of an electric field rather than their *m/z*[33]. The vast possibilities have resulted in highly elaborate and arduous separation techniques that often take much longer than the MS analysis itself. MALDI, in its simplest form, can analyze complex samples with minimal separation.

1.1.2. Matrix-Assisted Laser Desorption/Ionization (MALDI)

1.1.2.1. History of MALDI

Like other pulsed ionization techniques, laser desorption/ionization (LDI) is particularly useful for analyzing solid samples. Instead of applying a beam of neutral atoms in fast atom bombardment (FAB)[34] or charged ions in secondary ion mass spectrometry (SIMS)[35], LDI employs high energy photons to irradiate and desorb a precise area of a solid sample to produce ions[36]. However, because of the strong laser energetics, LDI often leads to immediate fragmentation, particularly of labile bonds in large molecules such as proteins, limiting the applicability of this technique to low mass biomolecules[37, 38] and structural analysis[39, 40]. This changed in 1987 when Tanaka *et al.* published their work in which lysozyme suspended in metal-filled glycerol was detected intact after desorption and ionization with a pulsed N_2 laser[41]. This

initial report was quickly followed by the work of Karas and Hillenkamp that achieved the same results by firing an Nd:YaG laser at a dried mixture of the same enzyme co-crystallized with nicotinic acid[10]. While Tanaka received the Nobel Prize for this "soft ionization technique," it was Karas and Hillenkamp's approach that the scientific community embraced and came to define as matrix-assisted laser desorption/ionization (MALDI). With the development of multiple matrices and reliable instrumentation, MALDI has moved beyond protein analysis into studying phospholipids[42, 43], amino acids[44, 45], polysaccharides[46, 47], oligonucleotides[48, 49], polymers[50, 51] and viruses[52, 53]. This method has even become a routine analysis for identifying bacterial infections[22].

1.1.2.2. The Basics of MALDI

In general, MALDI requires the co-crystallization of the analyte and the matrix compound, which is achieved by adding the matrix to the analyte-containing sample in an excess of ~5000:1. The matrix is most often an organic molecule with strong absorbance at the laser wavelength, typically in the ultraviolet (UV) range. In many commercially available systems, such as the one used for all experimentation in this thesis, it is the frequency-tripled Neodymium-doped Yttrium Aluminum Garnet (Nd:YaG) laser at 355 nm which is used[54]. Multiple matrices have been discovered for specific classes of analytes. For example, α-Cyano-4-hydroxycinnamic (CHCA) is most often employed for peptide analysis[55], 2,5-dihydroxybenzoic acid (2,5-DHB) is common for proteins[56], phospholipids[57] and small metabolites[58], and sinapinic acid (SA) is the matrix of choice for protein analysis[59]. Nonetheless, novel matrices and matrix mixtures, such as the 1,5 diaminonaphthalene (1,5-DAN) discovered in this lab for phospholipids[60], the rationally-designed 4-Chloro-α-cyanocinnamic acid (CICCA) for improved peptide sensitivity[61], and a CHCA and 2,5-DHB solution mixture for protein analysis[62] are continually being pursued to broaden the scope of MALDI in biological research. As such, matrix selection is a critical aspect of this technique.

There are various approaches to preparing the MALDI sample. The original method is the

dried-droplet approach[10], wherein the analyte and matrix solution are mixed before a microlitre volume of this mixture is deposited onto the target plate. Other approaches, such as the thin-layer[63] and the sandwich method[64], require the sequential addition of the matrix solution and the analyte solution onto the target plate. Numerous adaptations and variations of these approaches have been described in the literature[63-67] with the aim to improve the matrix-analyte co-crystallization and sample homogeneity.

Despite continuous efforts, the MALDI mechanism is not fully known. Multiple theories and pathways have been studied and explored regarding both ionization and desorption[68-71]. Generally, the entire process is described in these following steps, as shown in **Figure 1-2**. First, the laser ablates the analyte-matrix mixture. This mixture contains both neutral analytes as well as

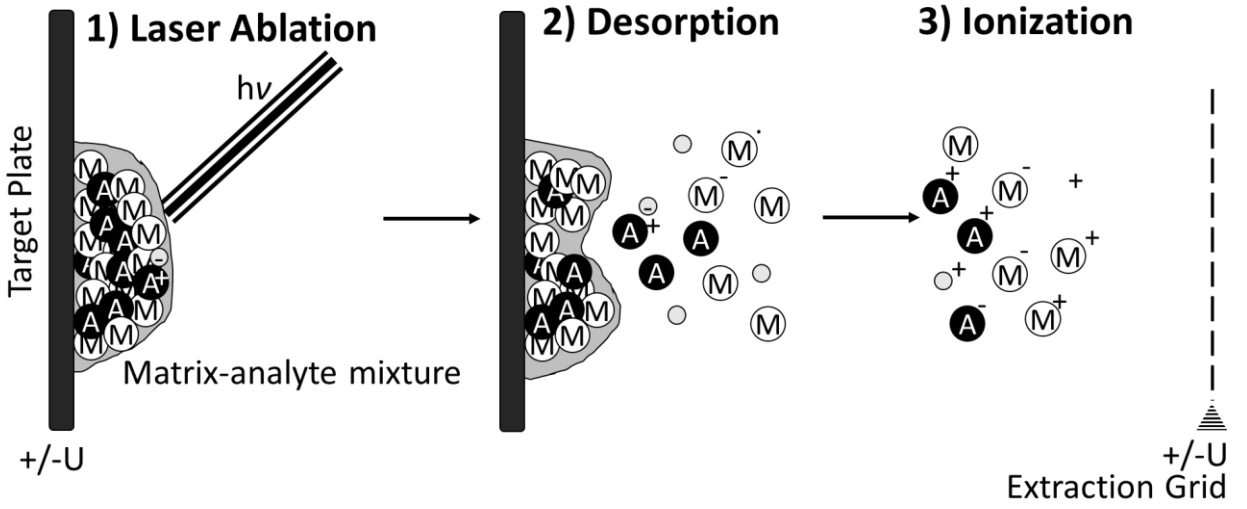

Figure 1-2: General MALDI Mechanism. 1) Laser ablates the analyte-matrix mixture containing neutral and precharged analytes. 2) The matrix absorbs and releases the bulk of the energy heat, leading to the sublimation of matrix molecules and the desorption of analytes and other impurities. 3) Desorbed molecules undergo proton exchange, most notably between matrix and analyte, to create ionized species. Some pre-charged analytes survive the desorption event and dissociate from their counterion to form charged analytes.

precharged analytes formed during sample preparation. The matrix molecules absorb most of this energy and release the bulk of it to the surrounding in the form of heat. This thermal expansion leads to the desorption of the matrix and analyte from the surface, creating a hot plume of gaseous molecules containing a mix of charged and neutral matrix molecules. The reactive matrix species undergo protonation or deprotonation events with analyte molecules, leading to their ionization. At the same time, some of the desorbed precharged analytes retain their charge after dissociating from their counterions, producing the "lucky survivors." Experimental results have found evidence supporting both mechanisms, for example, that of Jaskolla and Karas 2011 which investigated the preferred mechanism as a consequence of laser fluency, the acidity of the analyte and the pH of the sample preparation solution [72]. Finally, depending on the extraction voltage, either cations or anions are propelled into the mass analyzer, typically a time-of-flight (TOF).

1.1.3. Time-of-Flight (TOF) Mass Analyzer

The concept of a linear time-of-flight (TOF) system was first described by Stephens in 1946 as "a pulsed mass spectrometer with mass dispersion" at the annual meeting of the American Physical Society at the Massachusetts Institute of Technology in the United States[73]. Soon after, Cameron and Eggers (1948) managed to build such a system, dubbed the "Velocitron," to study mercury gas[74]. However, this was not a true TOF because the ions were not introduced with equal momentum. It was not until 1953 that Stephens himself introduced the TOF with an accelerator, albeit with a low mass resolution of twenty[20]. Since then, advancements in electronic circuitries, innovations that counter the effects of energy spread[75-77] have steadily improved the mass resolving power of TOF analyzers to rival that of orbitraps[78].

A TOF analyzer measures the amount of time ions take to travel across a high vacuum, field-free drift tube of a fixed length (L) post acceleration in an electric field (V_s/L). This measurement,

known as the time of flight (t), can be used to determine the *m/z* given the mathematical relationship described in **Equation 1-1**:

$$m/z = \left(\frac{2eV_s}{L^2}\right)t^2$$

Equation 1-1: Relationship between *m/z* and Time (t) in a TOF Mass Analyzer. With the length of the flight tube (L), the elementary charge (*e*), and the electric field fixed, the time an ion spends in the TOF before reaching the detector reveals its *m/z*.

This equation dictates that ions of the same charge with higher mass will have a longer time-of-flight than those with a lower mass. Indeed, since ions experience the same initial acceleration voltage, they possess the same kinetic energy during their flight and therefore travel at a velocity that is inversely proportional to their mass.

The most simplistic kind of TOF analyzer is the linear TOF system, shown in **Figure 1-3**, composed of an accelerator, a metal flight tube, and a detector. Linear TOF systems offer certain advantages over other types of mass analyzers. For one, linear TOF systems have no theoretical mass range limit. Commercial systems are mostly limited by ion stability in the source and the choice of detector[19, 79, 80]. A meter-long flight tube under constant vacuum is characteristic of linear

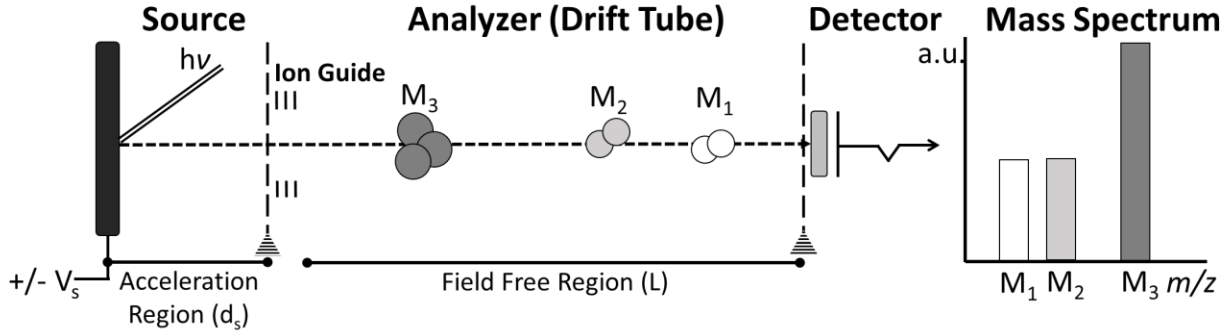

Figure 1-3: Linear TOF MS System Schema. A linear TOF MS is composed of an accelerator embedded in the ion source, ion guides that lead the ion to the linear flight tube, and an ion detector at the other end of the flight tube.

TOF systems. A long flight path improves the mass resolution by elongating the flight time between ions of similar *m/z*. A high vacuum environment reduces peak broadening due to loss of kinetic energy or fragment ion formation upon collision with ambient gas molecules. However, there are practical limits to the flight tube length and the vacuum strength. Other approaches are needed to improve the mass resolution of TOF MS.

1.1.3.1. Improvements to TOF: Delayed Extraction (DE) and the Reflectron (rTOF)

Two problems that plagued early TOF systems was the initial spatial distribution and energy spread of ions. These two problems are inherent in the MALDI process since not all analytes are positioned flat against the target plate and are further subject to different laser energy levels depending on the laser ablation pattern. Both issues lead to a greater distribution in initial velocity and therefore flight time, resulting in broader peaks and lower mass resolution. Thankfully, the

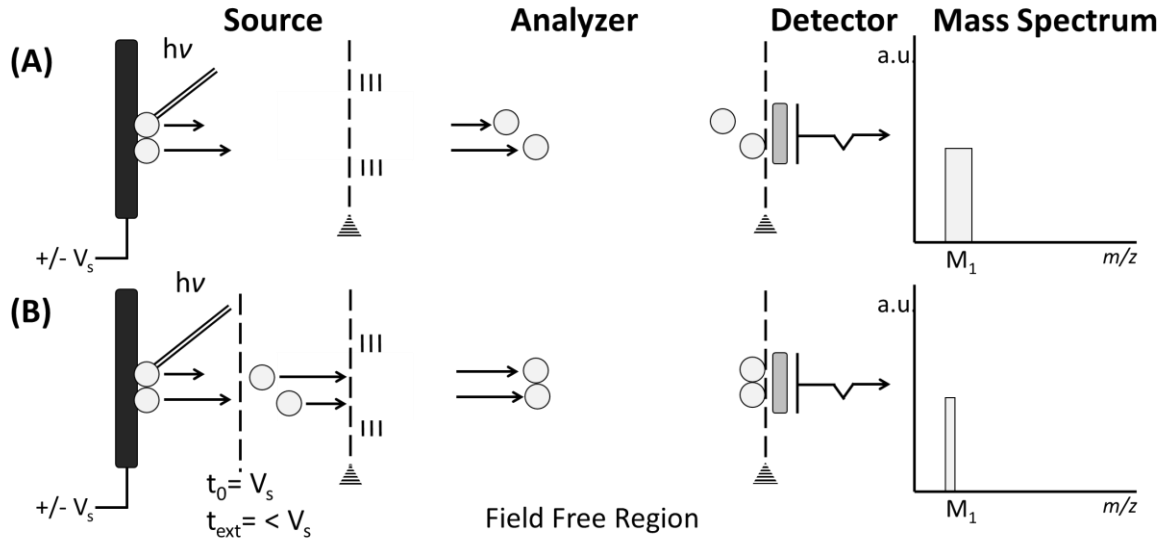

Figure 1-4: Delayed Extraction Schema. (A) With constant field extraction, ions of the same *m/z* but differing initial kinetic energy will arrive at the detector at slightly different times. (B) Delayed extraction corrects for the initial spatial distribution of ions of the same *m/z* by applying the acceleration voltage a few nanoseconds after the laser pulse. This results in the time focusing of the ions on the plane of the detector and improve mass resolution.

development of delayed extraction[81] and the reflectron TOF[77] have helped mitigate these issues.

Delayed extraction (DE) compensates for the initial spatial distribution among ions of the same *m/z* caused by the difference in their initial velocity[82]. As shown in **Figure 1-4**, instead of applying the acceleration voltage immediately upon laser pulse, the electric field is switched on some nanoseconds later so that ions with higher initial kinetic are further away from the extraction plate and receive less energy, while those with lower kinetic energy receive more. The closer level of kinetic energy helps to center these ions in time, decrease peak width, leading to an increase in mass resolution. DE can be applied for both low mass[83] and high mass molecules[84].

The reflectron corrects for the difference in initial kinetic energy of ions (ε) of the same *m/z* through lengthening their flight time according to their kinetic energy. As seen in **Figure 1-5**, through a series of electrostatic mirrors, the reflectron deflects the ion beam and forces ions with a higher kinetic energy (and higher velocity) to penetrate more deeply into the electric field,

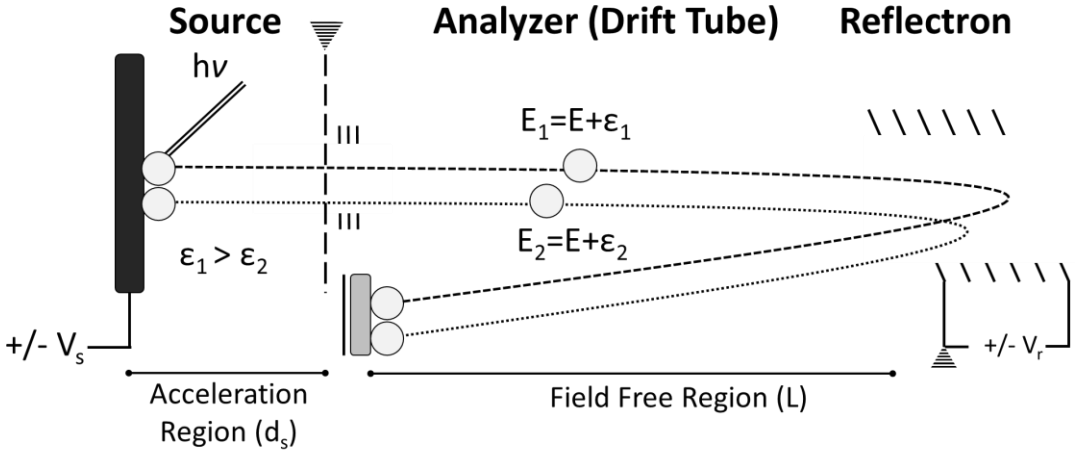

Figure 1-5: General Schema of reflectron TOF MS. The reflectron is composed of a series of electrostatic grids whose voltage (V_r) is higher than the source voltage (V_s). Specifically, the end plate voltage is higher than the source voltage so that the ions will be ejected out of the reflectron in the opposite direction. This configuration provides ions with a greater initial kinetic energy (ε) a longer flight path, resulting in ions of the same *m/z* arriving simultaneously at the detector.

effectively allowing those with a lower kinetic energy to "catch up" when reaching the detector[77]. This results in a decrease in peak width and consequently, an improvement in mass resolution, as shown in **Figure 1-5**. TOF analyzers with multiple reflectrons offer multiple instances of rectifying the initial kinetic energy spread. The most common is the W formation that contains two electrostatic grids at the end of each junction to guide the ions[85, 86]. However, more complex geometries and flight paths have been developed to reach higher mass resolutions, such as the multi-reflecting TOF by Verechikov *et al.* that claimed 500k mass resolution at *m/z* 500[87] and the commercially available spiral TOF mass spectrometer that claimed 80k mass resolution at *m/z* 2564[88]. These approaches are invariably compromised by the loss in sensitivity, since not all ions—particularly those of high mass—are stable enough to survive the reflectron event.

1.1.3.2. TOF/TOF Tandem Mass Spectrometry (MS/MS)

Tandem mass spectrometry couples two mass analyzers within a single mass spectrometer to provide structural information on the target analyte ions. This is achieved by isolating the precursor ion in the first mass analyzer, inducing its fragmentation, and detecting the product ions using the second mass analyzer. Because ionized molecules tend to dissociate in characteristic ways based on the fragmentation technique and their chemical composition, the product ions provide information on the structure of the precursor ion. Scientists have taken advantage of this phenomenon to create MS/MS databases to better identify proteins[89, 90], metabolites[91] and other compounds[92, 93].

In most common situations, MS/MS is achieved inside a collision cell, during which a small amount of helium is introduced to induce fragmentation[94, 95]. In the MALDI-TOF/TOF system used for all work presented in this thesis, however, no such cell exists. Rather, the TOF/TOF system relies on excess laser energy uptake from the precursor ion to generate metastable decomposition and induce post-source fragmentation, a timed ion selector that only allows these ions to pass

through for secondary acceleration and a secondary reflectron TOF for final separation. This set-up is known as the "LIFT" technique because of the "lift" in potential by 19 kV upon entering the LIFT device[96] shown in **Figure 1-6**. This approach takes advantage of the phenomenon that fragment ions produced post-source retain the same velocity as their parent ion, since the total kinetic energy is shared among these fragment ions in proportion to their mass. TOF/TOF MS is powerful for peptide sequencing and other large molecules ($m/z \leq 4000$) but is less effective for small molecules, which are inherently more stable. This approach is also non-ideal for complex mixtures with compounds of similar *m/z*, since a large precursor ion mass window of approximately 4 Da is necessary to achieve substantial MS/MS results**.**

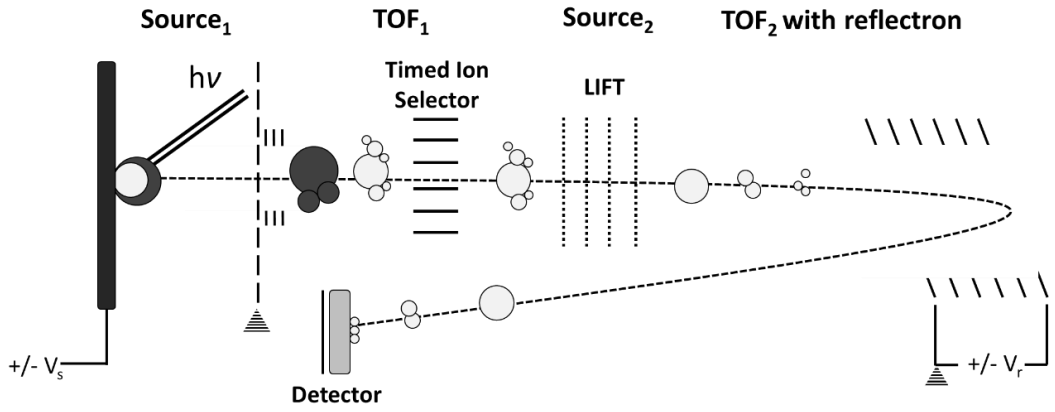

Figure 1-6: LIFT-TOF/TOF Schema. In LIFT-TOF/TOF, an initial strong laser pulse leads to metastable formation post-source. The timed ion selector allows ions of a certain velocity in the first TOF to enter the LIFT cell, where the metastable fragment ions from the selected precursor ion undergo secondary acceleration before entering the second TOF for mass separation.

Sequential or multistage mass spectrometry, dubbed MS^n, is an extension of tandem mass spectrometry whereby the isolation-fragmentation cycle is performed "n" number of times before being sent to the detector. This technique is needed to obtain in-depth structural information on a specific region of a molecule, for example, the determination of double-bond positions of triacylglycerol (TAG)[97]. MS^n is not possible with TOFs but can be realized on set-ups that can eject

product ions for further fragmentation, such as sector instruments [98], quadrupole ion traps[99] and quadrupole FT-ICRs [100].

1.2. From MS to Imaging MS

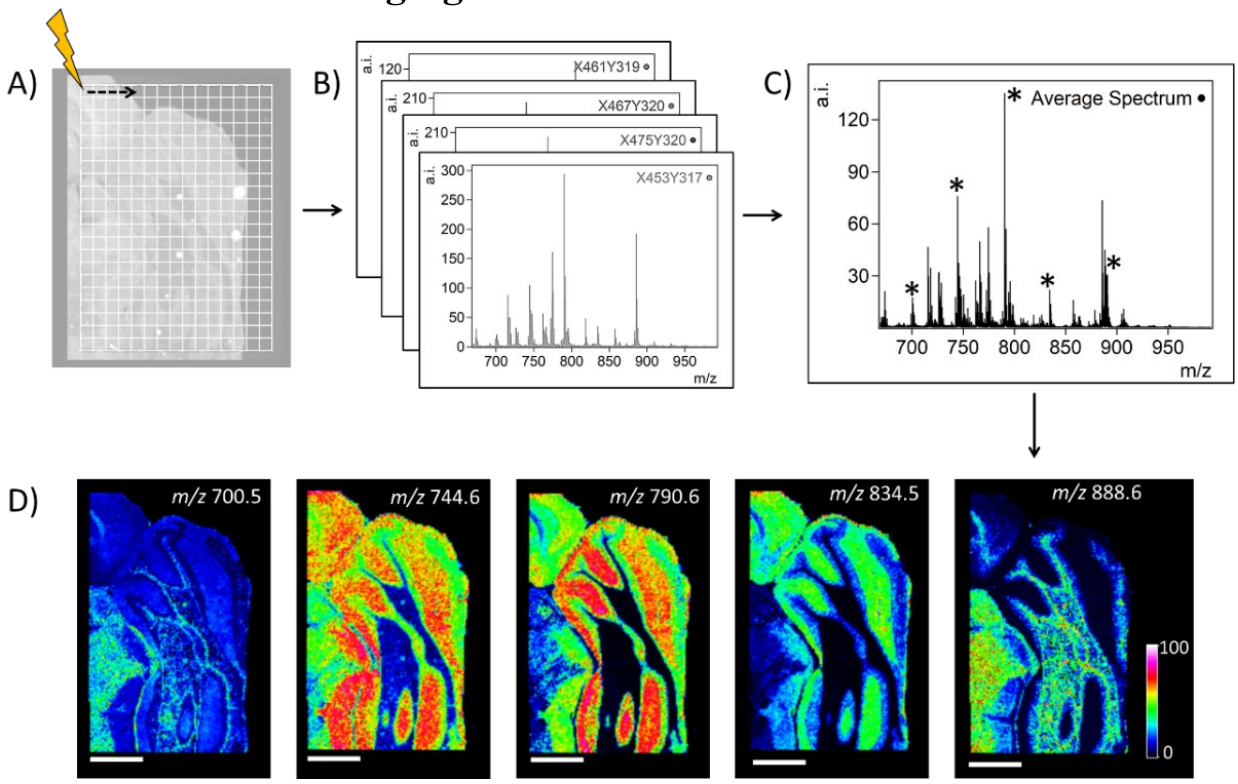

Figure 1-7: General Overview of Imaging Mass Spectrometry. A) To begin, the selected measurement region is divided into a grid. B) A mass spectrum is acquired at each point, or pixel, along the grid as shown in Panel A. C) Once all mass spectra have been acquired, an average spectrum representing the entire analysis can be visualized in specialized software. D) Selecting an *m/z* signal of interest will generate the corresponding ion heat map of interest, giving insight into the spatial distribution of that signal. The sample here is a horizontal mouse brain cerebellum acquired in negative ion mode at 30 µm spatial resolution and 100 laser shots per pixel and 1,5-DAN as the matrix. The scale bar represents 1 mm.

Imaging MS (IMS) is a powerful technique for investigating the surface molecular profile of any sample, for example, a thin tissue section. As shown in **Figure 1-7**, to achieve this, the area

to be analyzed, the measurement region, is divided into a grid of a fixed dimension. The instrument scans across the grid, sampling at each point, commonly referred to as pixels. The distance between each pixel defines the spatial resolution, though this is only true of pulsed ionization techniques. Once completed, the IMS dataset contains the relative abundance of the *m/z* signals at each pixel position. The spatial distribution of any *m/z* signal can be mapped out on a Cartesian coordinate plane where each pixel is represented by a coordinate and at each coordinate the intensity is represented by the appropriate colour schema. In short, IMS simply repeats the same analysis across a given area at a precise and regular spatial interval to provide ion heat maps of the species present on a surface. Currently, three major IMS approaches exist: secondary ion mass spectrometry (SIMS), MALDI and desorption electrospray ionization (DESI). SIMS achieves ionization through the bombardment of the sample surface with an ion beam[101], while DESI sprays the sample with a stream of electrically charged solvent that both desorbs and ionizes the sample[102].

1.2.1. Imaging MS: From Proteomics to Lipidomics

The first IMS results were obtained as early as 1962 by Castaing and Slodzian on isotopic distribution of elements[35]. However, IMS as a biomolecular imaging tool was not fully realized until the advent of MALDI, for reasons specified in previous sections. While the first MALDI IMS results could very well be that of salts on pine tree roots obtained with a laser microprobe mass analyzer (LAMMA) presented in 1994 at the 42nd Annual Meeting of the American Society of Mass Spectrometry from Spengler[103, 104], it was the IMS results of proteins and peptides from an aggregate of human buccal mucosa from Caprioli *et al*. published in 1997 that spurred the era of MALDI IMS in biology[105].

MALDI IMS applications in proteomic studies has since exploded. The technique has been applied to studying nearly all mammalian organs[26, 106-109]. Optimized sample preparation protocols

for manipulating fresh frozen[110] as well as formalin-fixed paraffin embedded (FFPE) tissues[111] also emerged. On top of this, the ability to accomplish whole-body IMS on rat[112, 113], obtain high resolution IMS data with an FT system[114], conduct bottom-up proteomics with tryptic digest[111, 115], trace drugs and their metabolites[116, 117] and correlate the ion signals to distinct histological features[109, 118] further fueled the widespread adoption of this technique.

At the same time IMS made headways into proteomics, it also began to contribute to the nascent field of lipidomics. Much of this was driven by a growing awareness towards the importance of lipids in disease states and the power of MS[119] and IMS[120] in tracking and visualizing this dysregulation. The earliest reports of lipid IMS were conducted by SIMS[116, 121] in the early 2000s, though these were mostly lipid fragments rather than intact molecules. While MALDI MS of lipids was already demonstrated in the 1995[122, 123], more effort at that time was focused on resolving isobars through ion mobility[42, 124] and understanding ion suppression effects[125] than IMS. It was not until the arrival of fine matrix deposition approaches[126] and other sample optimization techniques[60, 127] that pushed MALD-TOF IMS into the center of lipidomic studies. It is important to note that around the same time, DESI arrived on the scene[102]. This ambient ionization technique offers the ability to detect lipids and other small metabolites with minimal sample preparation and has been the driving technology behind real-time cancer diagnosis and grading[128]. However, because of limitations in mass range and spatial resolution inherent in the technique[129], DESI is still not as popular as MALDI today.

1.2.2. MALDI Imaging Mass Spectrometry of Lipids

Lipids are small hydrophobic or amphiphilic molecules important in living organisms. Beyond maintaining the structural integrity of most cells[130], they act as specialized signalling molecules[131] whose dysregulation often lead to inflammation[131] and are implicated in diseases ranging from

metabolic disorders[132, 133] to neurological diseases[134, 135] and even cancer[136, 137]. Indeed, as of March 25, 2020, Lipid Maps, the most comprehensive MS lipid database, contained 43,645 unique lipid structures, nearly 50% of which were manually curated and confirmed (see in Table 1-1).

Table 1-1: Total Lipid Species in Lipid Maps by Category as of March 25, 2020. Nearly 45,000 species are included in this database, over 21,000 of which are curated. Curated species have been confirmed by the literature, while computationally generated ones are theoretically possible.

Lipid Category	Curated	Computationally Generated	All
Fatty acyls	7582	1792	9374
Glycerolipids	229	7379	7608
Glycerophospholipids	1606	8312	9918
Sphingolipids	1262	3176	4438
Sterol lipids	2828	0	2828
Prenol lipids	1353	0	1353
Saccharolipids	22	1294	1316
Polyketides	6810	0	6810
TOTAL	**21692**	**21953**	**43645**

Classified into eight categories based on their function and structure[92], the largest of these curated groups are the fatty acyls and polyketides with more than 6000 species each, followed by sterol lipids with nearly 3000 species,. While many of these classes have been investigated previously by MALDI IMS, this introduction will focus on four particular (sub)classes relevant to the thesis: (a) sterols, a class of sterol lipids, (b) fatty acids, a class of fatty acyls, (c) glycerophospholipids, also known as phospholipids, and (d) gangliosides, a subclass of sphingolipids.

1.2.2.1. MALDI IMS of Free Fatty Acids and Sterols

Fatty acids (FAs) are carboxylic acids with a hydrocarbon chain. Saturated FAs contain no double bonds, while those with at least one on the aliphatic tail are unsaturated. Within unsaturated FAs, those with only one double bond are monosaturated and those with more are polyunsaturated.

De novo FA synthesis occurs in the liver from excess carbohydrates[138]. The resulting FAs are stored for future use as triacylglycerols (TAGs) or incorporated into other lipids, such as phospholipids and sphingolipids. Interestingly, FAs can be cleaved from TAGs and released as free fatty acids (FFAs) into the bloodstream to act as signalling molecules in regular physiological processes[139].

FAs are named based on the carbon chain length, the number of double bonds and each double-bond stereochemistry. For example, the fatty shown in **Figure 1-8** can also be referred to as FA(20:4(5Z,8Z,11Z,14Z)) because it has 20 carbons and four cis unsaturations at the 5th, 8th, 11th and 14th carbon position. Due to the difficulty of ascertaining the stereochemistry and the exact position of the double-bond through standard MS and MSMS, in most cases, only the chain length and total number of double bonds are reported, so FA(20:4). When existing as FFAs, most are referenced by their conventional names rather than the prescribed nomenclature, for example, arachidonic acid (AA) rather than FA(20:4) or the IUPAC nomenclature (5Z,8Z,11Z,14Z)-5,8,11,14-Eicosatetraenoic acid.

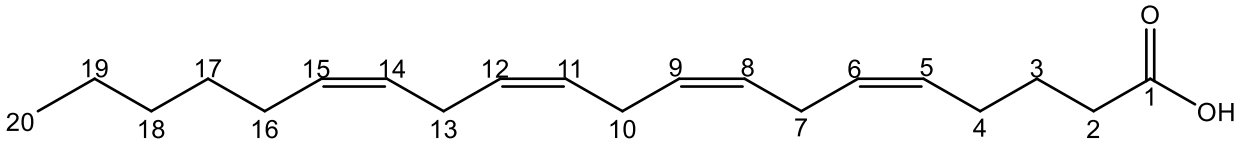

Figure 1-8: An Example Fatty Acid. Fatty acids are defined by the length of their aliphatic tail, the number of double bonds and the stereochemistry. This FA is known as FA(20:4(5Z,8Z,11Z,14Z)) when bound to another structure and commonly referred to as arachidonic acid (AA) when free floating. The carbon number for this fatty acid is shown.

MALDI MS of FFAs were first conducted with meso-tetrakis(pentafluorophenyl)porphyrin (MTPP)[140], a high molecular weight matrix with little background signal in the low mass range. However, this method only worked for saturated FAs. Later, two highly basic matrices, 1,8-Bis(dimethylamino)naphthalene (DMAN)[141] and 9-aminoacridine (9-AA)[142], were demonstrated

to work for detecting FFAs in negative ion mode, the later of which has been employed in an IMS context[143]. More recently, 1,6-Diphenyl-1,3,5-hexatriene (DPH), a fluorescent probe, has been discovered to be suitable for detecting FFAs and phospholipids with little matrix noise[144]. Another avenue for IMS of FFAs avoids organic matrices altogether in favor of metals, particularly silver. This includes specialized silver nanoparticles spray-coated on tissue sections[145] and sputter deposition of a nano-layer of silver aggregates[146]. Because of silver's preferential chelation to double bonds, this method also works spectacularly well for cholesterol, a sterol[146]. Sterols represent a family of polycyclic compounds whose general structure is shown in **Figure 1-9.** A component of all eukaryotic cell membranes, cholesterol regulates the cell membrane fluidity[130] and assist in lipid raft domain function and assembly[147]. It is an important component of the myelin sheath, the reason for which 25% of all cholesterol in the human body is found in the brain[148].Cholesterol is the simplest of all sterols. It can be transformed into a cholesterol ester with the addition of a fatty acid, a reaction catalyzed by lecithin:cholesterol acyltransferase (LCAT)[149], and be transported in the blood as needed while bound to lipoproteins[149]. It is also a precursor for steroid hormones[150] and certain bile acids[151]. Thus, cholesterol homeostasis is crucial and its dysregulation has been linked cardiovascular diseases such as atherosclerosis[152] and stroke[153], and

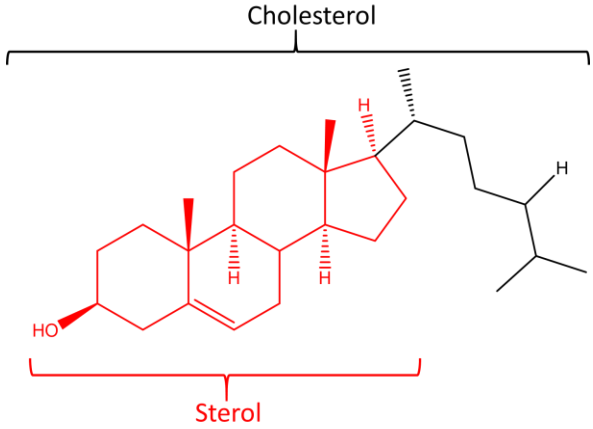

Figure 1-9: Structure of Cholesterol. Cholesterol is one of the main types of sterol, the polycyclic structure in red. Ubiquitous in animals, it is obtained from diet or synthesized *de novo*.

various types of cancer[154].

The earliest IMS of cholesterol was obtained by SIMS on freeze-fractured membranes of liposomes[155]. In both SIMS and MALDI, however, cholesterol is most readily detected as a dehydrated species[119, 156, 157], making it impossible to differentiate between a true cholesterol and a sterol fragment ion issued from a cholesterol ester. Silver adducts in both LDI and SIMS overcame this challenge as cholesterol is detected intact in its argentinated ion form[146, 158]. With MALDI, however, should the sample be low in TAGs, it is also possible to detect cholesterol as a sodiated species after doping the samples with excess sodium[159].

1.2.2.2. IMS of Phospholipids

Phospholipids (PLs) are amphiphilic molecules composed of a hydrophobic diglyceride fatty acid tail and one of six possible polar head groups that determine their subclass. Phosphatidylcholines (PCs) represent the major constituents of the cell's lipid bilayer[130, 160] and is therefore highly abundant in biological systems. The other subclasses, namely phosphoethanolamines (PEs), phosphatidylserines (PSs), phosphotidic acids (PAs), and phosphoinositides (PIs) can also be found on the cellular membrane and provide more specialized signalling functions[161-163]. Their structures are shown in **Figure 1-10**.

PLs were first detected by MALDI in 1995 by Harvey[123] with 2,5-DHB. In this work, Harvey investigated the ionization of all PL classes in both positive and negative ion mode. While this work demonstrated the ability to detect all PLs in positive ion mode, later work by Petković *et al.* revealed that in complex mixtures such as a cell extract, PCs dominate the positive spectra[125]. This is of concern for IMS because the PLs cannot be readily separated prior to analysis except with ion mobility, which limits the acquisition speed and worsens the detection limit. Thankfully, the discovery of 9-AA for negative ion mode detection allowed for the detection of the remaining species, such as PIs, PAs and PSs, without ion suppression from PCs[142]. However, this meant that

two samples are needed to obtain the full PL profile, which pose technical and sometimes practical challenges for IMS experiments.

This problem was solved with the advent of dual-polarity matrices such as 1,5-DAN[60] developed in our laboratory and more recently in a different group, luminol[164]. Beyond the obvious benefit of only needing one matrix, it is also possible to conduct dual-polarity experiments on a single tissue section to obtain the global phospholipid profile. This can be achieved by artificially setting an offset in both the x and y dimension that is equivalent to half of the spatial resolution to avoid resampling the same tissue surface[60, 165]. In certain cases, it is also possible to conduct dual-

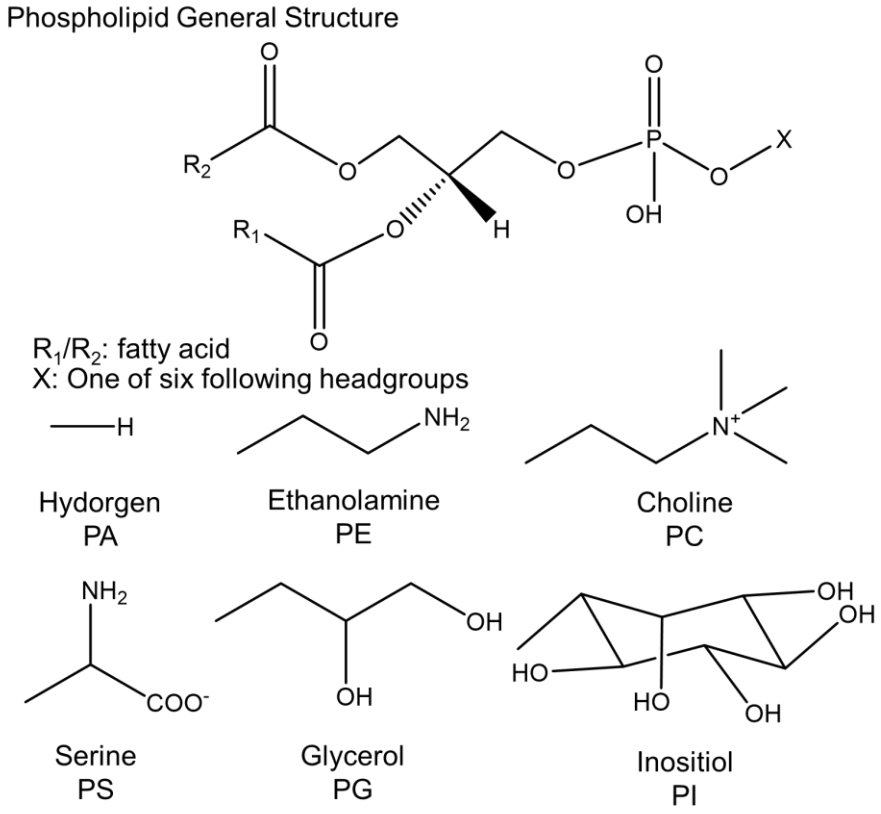

Figure 1-10: The Six Phospholipid Classes and Their Headgroups. Phospholipids share the same general structure shown and can have six different head groups: hydrogen (PA), ethanolamine (PE), choline (PC), serine (PS), glycerol (PG) and inositol (PI).

polarity IMS results without an offset by minimizing the number of laser shots per imaging coordinate and therefore conserving enough samples for subsequent analyses[166]. This approach can attain a resolution as high as 10 μm, though this method has yet to be demonstrated by other researchers[166].

PL confirmation by MS/MS are possible thanks to their characteristic fragmentation from their headgroup. Nearly all headgroups provide unique *m/z* values upon fragmentation either in positive or negative ion mode[167]. The remaining mass after removal of the headgroup, as well as the parent ion mass, provide information on the DG. MS^3 can provide further details on the DG to discern the fatty acid tails while specific derivatization approaches can help identify the double-bond position[168, 169]. However, in situations where no information about the fatty acid can be derived, a summed value representing the overall fatty acid length and double bond count is provided. For example, PC (34:2) is preferred over PC (18:1/16:1), since the former denotes a DG of a total of 34 carbons and two double bonds, rather than two FA, one of C18:1 and the other C16:1.

1.2.2.3. IMS of Phospholipids on *Drosophila*

MALDI IMS of PLs have been successfully conducted on a wide variety of samples beyond mammalian tissue. These include black rice seeds[170], cotton seeds[171], mosquitoes[172] and *Drosophila*[173]. Also referred to as the common fruit fly, *Drosophila* has, for more than a century, revolutionized our understanding of biological development and the inheritance of genetic disorders[174]. Their high genetic resemblance with mammalian systems[175], relative ease in inducing and controlling genetic mutations[176], and their short reproductive cycle[177] have continued to attract researchers to conduct important genetic and drug screening tests on them before advancing to more complex and expensive models[178]. MALDI IMS is a potential approach that can help provide information on the drug localization and other metabolic changes in the fly organs.

Unfortunately, published MALDI IMS studies on *Drosophila* are limited[173, 179, 180]. The first

example was that of Urban *et al.* in 2011 which investigated the phospholipid distribution of a dissected fly organ, namely the egg chamber, by MALDI IMS[173]. This was followed by two other studies that revealed organ-specific distribution of phospholipids, fatty acids and other metabolites in the organism[179, 180]. These publications also investigated the embedding media and organic washes to help with the cryosectioning of such a fragile organism[179, 180]. While no revolutionary phospholipid species were revealed during their work, these feasibility studies remind researchers of the possibility to conduct IMS studies of fruit flies.

1.2.2.4. IMS of Gangliosides

Gangliosides are glycosphingolipids marked by one or more sialic acid residues attached to the galactose moiety of the sugar backbone[181]. Highly expressed in neural cells of the grey matter, these signalling molecules are most abundant on the outer leaflet of the cellular membrane of the lipid raft domain[182]. All gangliosides are synthesized from lactosylceramide (LacCer) in a step-wise manner through a series of enzymes into four different series[183], as shown in **Figure 1-11**.

Gangliosides are named based on the number and position of sialic acid residues, the length of the sugar backbone, and, if known, the length of the fatty acid chains on the ceramide. GA, GM, GD, GT, GQ and GP represent zero to five sialic acid residues, respectively. This is followed by a number 1, 2 or 3, which signifies the length of the sugar backbone, where the smallest number represents the longest backbone. Positional isomers of sialic acid residues are indicated by a lower-case letter following the number, which generally fall within the series. The fatty acid chain nomenclature follows those of the FAs. As such, the ganglioside GD1a (d18:1/18:0) is a ganglioside of series a containing two sialic acid residues, a full sugar backbone, and a ceramide with a sphingosine and a fatty acid chain of 18. While it is generally accepted that ceramides are composed of a sphingosine and a fatty acid, in cases where no MS/MS data is present, the fatty acid information is condensed, for example, (d36:1) instead of (d18:1/18:0).

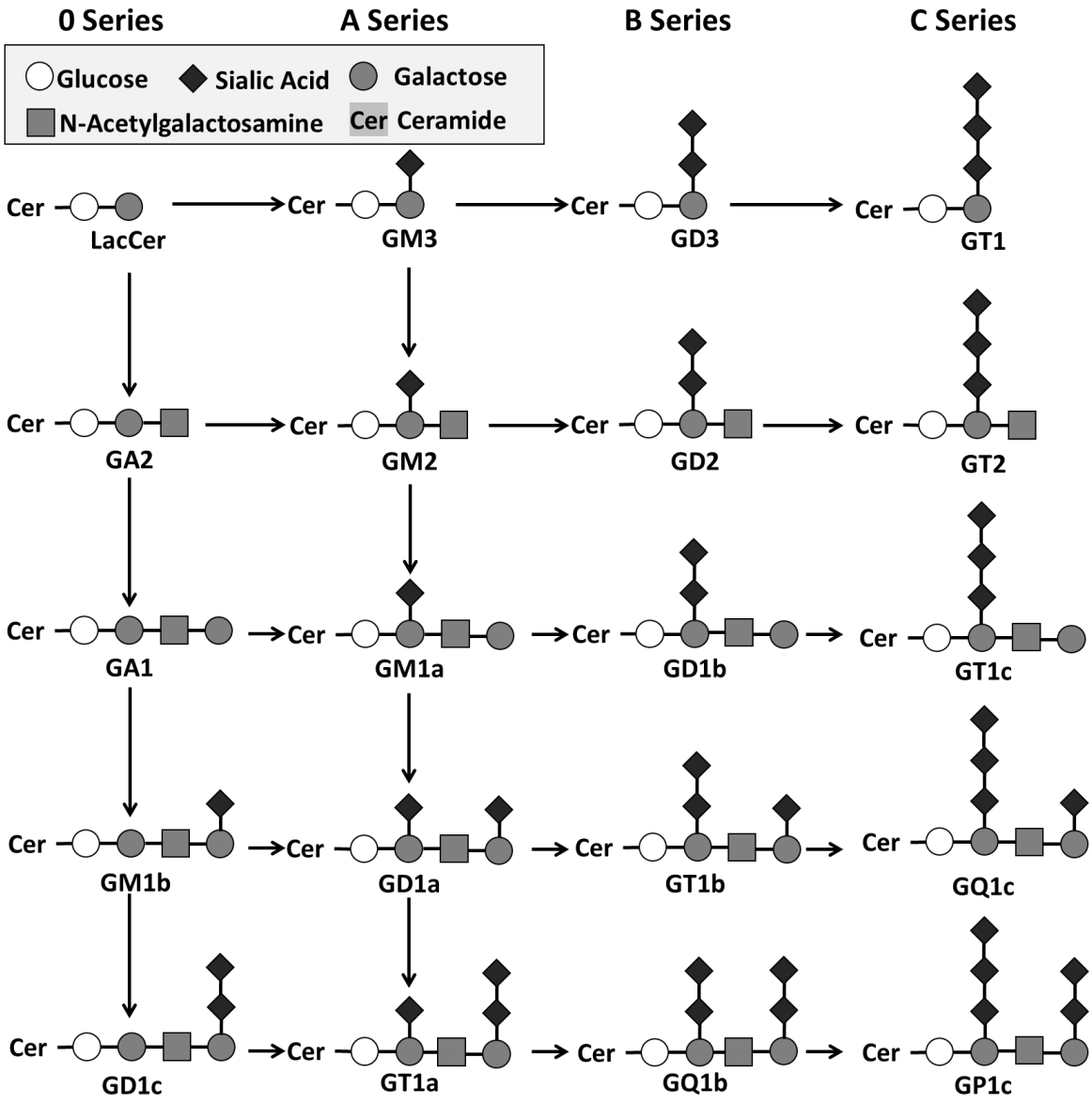

Figure 1-11: Ganglioside Synthesis Pathway. Gangliosides are synthesized from and degraded into LacCer with the help of specific enzymes for each addition or removal of a sugar moiety. The a and b series gangliosides are the most abundant in the brain and most widely studied in IMS.

Unsurprisingly, IMS of gangliosides are mostly focused on the brain[184], with studies revolving around neurodegenerative diseases such as Alzheimer's[134] and Parkinson's[185] and traumatic events such as stroke[186, 187]. Most are focused on the a- and b-series gangliosides, the most abundant in this organ. Novel matrices[188-191], derivatizations[192, 193], high pressure systems[194, 195] and ion

mobility[196-198] have also been proposed to lower the detection limit and increase the stability of these molecules during analysis, some of which have been applied for IMS applications.

MS/MS determination of gangliosides is most certainly characterized by the sialic acid residue, which readily fragments in the MALDI experiment to provide a strong signal at *m/z* 290.1[194]. This is followed by the sequential losses of the sugar backbone, leaving only the ceramide. In cases where multiple sialic acids are present, MS/MS data will reveal the sequential loss of these residues before fragmentation from the sugar backbone. Examples can be seen in **Supplemental Information of Chapter 3.**

1.2.3. Advantages and Drawbacks of MALDI IMS

IMS is a label-free technique capable of detecting hundreds of biomolecules in one single analysis. By comparison, immunohistochemistry (IHC) usually target one molecule of interest, while molecular fluorescent probes can at most provide results for three molecules of interest from the same tissue section[199, 200]. Although more recent techniques such as co-detection by indexing (CODEX), a fluorescent multiplex immunohistochemistry, and imaging mass cytometry (IMC) have overcome this limitation, the former achieves high multiplexing through multiple staining cycles that provide images of three molecules each time, while the latter is limited to around the forty available rare metal elements[201, 202]. As such, the high abundance of analytes detected and the untargeted nature of MALDI IMS continue to make it an ideal tool for biomarker discovery[203, 204]. IMS is also uniquely positioned as the sole method that can provide localization of individual lipid species, such as PLs, GGs and TAGs. In the case of gangliosides, for example, the IHC antibody recognizes the oligosaccharide moiety, and thus cannot differentiate between the long chain and short chain version of the same ganglioside[205]. MALDI IMS also enabled the localization of drug candidates and their metabolites[117], a feat nearly impossible with standard radiography. With 10

kHz laser technology and auto laser focus, MALDI IMS data acquisition has reduced significantly, capable of acquiring a coronal rat brain section at 50 μm spatial resolution in approximately 45 mins[206]. Continued advances in ion mobility coupled to IMS[207, 208] also promises to revolutionize the capabilities of this technique.

Of course, IMS has its shortcomings. High signal intensity in IMS is not directly correlated with its absolute abundance. Rather, species with greater ionization efficiencies will be more abundant and suppress other species present in the same local environment. This ion suppression effect also greatly diminishes the dynamic range, particularly for MALDI-TOF IMS where no analyte separation occurs[209]. The matrix-analyte crystals also play a critical role in influencing the ionization event, sometimes leading to variability in signal intensity of the same species across one sample[210]. Because of these limitations, in most situations, IMS can only be appreciated as a semi-quantitative approach. IMS also falls short of the spatial resolution attainable by fluorescence and IHC. IMS operates mostly at the micron level. While submicron MALDI IMS has been demonstrated[211], the spatial resolution is limited by the laser focus size and the dramatic loss in sensitivity due to the small irradiation surface. SIMS imaging can readily produce images at the nanometer scale[212], but is highly limited in mass range. Nonetheless, advanced sample preparation techniques have overcome some issues in preferential ionization, while technological advancements continue to push the limits of spatial resolution and improve overall dynamic range[213].

1.2.4. MALDI IMS Sample Preparation

1.2.4.1. Thin Tissue Sections

A standard MALDI IMS experiment conducted on thin tissue sections can be divided into four parts: sample processing and sectioning, matrix deposition, data acquisition and data analysis,

as shown in **Figure 1-12**:

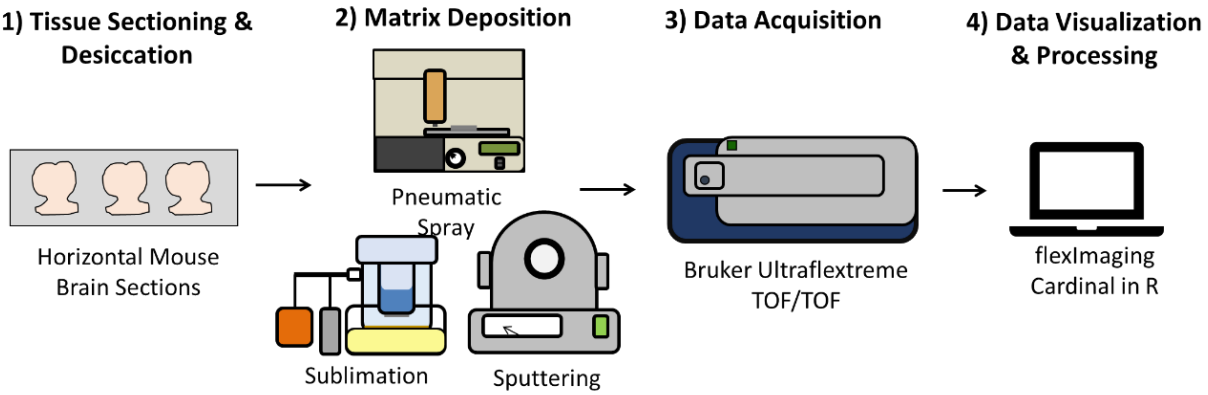

Figure 1-12: MALDI IMS Workflow. 1) Tissue samples are sectioned and left to desiccate. This step can be followed by a series of washing protocols to enhance analyte signal. 2) Matrix is homogeneously deposited onto the section. Several matrix deposition approaches are available. 3) Samples are introduced into the instrument for data acquisition. 4) Data is visualized and analyzed on a computer using specialized software.

First, the sample is sectioned into micrometer thicknesses. This is conducted in a cryotome for fresh frozen samples, or a microtome for FFPE samples. The thickness depends greatly on the sample, though for mammalian tissues, it is generally between 10-20 µm for fresh frozen samples[214] and ~5 µm for FFPE samples[111]. The sections are then typically mounted on indium-tin oxide (ITO) conductive glass slides and left to desiccate at room temperature. After desiccation, a series of washes or sample preparation protocols may be required before matrix deposition. For example, FFPE samples need to be deparaffinated, rehydrated, antigen retrieved and enzymatically digested[111], while a series of organic washes are necessary for high quality protein studies[214]. Some washes have been proposed to improve the detection of certain phospholipids in negative ion mode and gangliosides[215], though minimal sample preparation is suggested to minimize lipid delocalization. Once the protocols are completed, a homogeneous layer of matrix is deposited onto

the sample, either through a wet or dry deposition approach.

In the wet approach, the matrix is dissolved in a volatile solvent solution and typically applied with an automatic pneumatic sprayer[127] or a hand-held airbrush[216], though variations such as a humidifier[217] have also been tested. The spray system employed in this thesis is shown in **Figure 1-13**. With this system, an external syringe pump introduces the matrix solution and the TM-Spayer conducts multiple passes at a relatively high pressure and temperature to achieve a homogeneous deposition of fine crystalline matrix. The dry approach removes the solvent completely and is achieved through sublimation[126] or dry-coating[218]. While dry-coating can be thought of as dusting a cake, sublimation is more complex and requires a set-up similar to what is shown in **Figure 1-13**. To start, a thin layer of solid matrix is placed in the outer chamber while the sample slide is taped to the bottom of the inner lid so that, once sealed, the sample faces the matrix. The hot oil bath and the vacuum creates a low-pressure, high-temperature environment that induces the matrix to sublimate. Because the inner lid is chilled with an ice slurry, the gaseous matrix deposits onto the sample slide upon reaching the inner lid, forming a homogeneous deposition of fine matrix crystals.

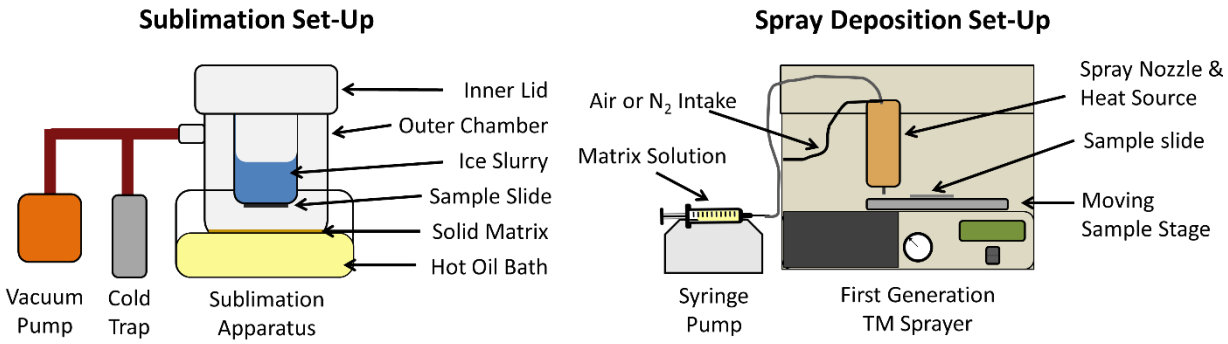

Figure 1-13: Sublimation and Spray Matrix Deposition Set-Up. The sublimation system requires a sublimation apparatus, a cold trap and a vacuum pump to achieve dry matrix deposition in a low-pressure environment, whereas the pneumatic spray system uses a robotic sprayer and a syringe pump to coat the sample homogeneously with layers of matrix.

The wet approach is suitable for all matrices and aids in the co-crystallization of analytes, a critical aspect of protein analysis, while the dry approach is mostly used for lipid studies, which have been shown to migrate naturally to the matrix surface to allow for easy detection[219]. The dry approach is also more amenable to high spatial resolution IMS analyses given the much smaller matrix crystals formed during sublimation as compared to spray deposition, though recent publications with robust automatic spray systems have demonstrated low-micron IMS results[166, 220]. Because matrices have varying sensitivities for different classes of lipids, the choice of matrix and deposition method can greatly influence the final result[127, 221].

Finally, the sample is introduced into the mass analyzer, where the region of interest can be selected for IMS data acquisition. The data is visualized in specialized software that displays the selected *m/z* values of interest as ion heat maps. Data analysis such as normalization, smoothing, peak picking, peak realignment and segmentation can be accomplished through proprietary software from vendors, such as SCiLS[222]. However, with the ability to export all IMS data into the standard open source imzML format[223] adopted since 2012, it is possible to accomplish the same data visualization and analyses with open source approaches. These include specialized packages in R, particularly Cardinal[224], created for IMS data analysis. The versatility with R has made it a popular choice for IMS data analysis. Indeed, most data analyses presented were accomplished with the Cardinal package in the R environment. Other free options include Matlab-based MSiReader[225] and msIQuant[226].

1.2.4.2. Microdissected Organs

Microdissection is a common approach to extract organs from small organisms for further analysis. Unlike laser capture microdissection (LCM), which employs a laser to excise specific cells of interest from an intact tissue section after staining[227], microdissection separates an organ in its entirety with sharp tools such as fine tweezers. IMS analysis of microdissected organs follow

the same workflow as thin tissue sections. In most cases, the microdissected organs are embedded into polymer before undergoing cryosectioning. Microdissection is particularly useful when it is difficult to study the organ with the other anatomical structures present. For example, OuYang *et al.* revealed the distribution of neuropeptides across microdissected supraesophageal ganglia (brain) and the paired commissural ganglia from rock crabs, *Cancer irroratus*, and blue crasbs, *Callinectes sapidus*[228]. It would have been difficult to section the hard shells without causing damage to the thin neural structures. Organs that have complex 3D structures would also be a challenge to interpret with one single cross section, while a 3D reconstruction of the sections solely to visualize this organ would also be tedious and unnecessary.

Despite these advantages, there have been limited IMS studies on microdissected organs[173, 228, 229]. One explanation could be that the most popular IMS samples—tumours and other mammalian organs—do not require microdissection. Another possibility is that microdissection is commonly accomplished in buffered saline solutions. While the bulk of this salt would be removed by the successive washes for protein IMS analysis, extensive washing will lead to lipid delocalization and signal loss.

1.2.5. Effect of Salts on MALDI IMS of Lipids

Salts are omnipresent in biological samples. The two highly abundant salt cations, sodium and potassium, adduct with analytes to form sodiated and potassiated species that are readily detected alongside the protonated species[125, 230]. This phenomenon is especially problematic for IMS lipidomic studies in positive ion mode where all three adducts can be observed[221]. Indeed, alkali salt adducts complicate an already crowded spectrum and lead to multiple isobaric species that are very difficult to separate by mass spectrometry. Further, the total signal of a species is divided among these adducts, leading to lower intensities that may fall below detection limits

within the noise level as well as complicating quantitative efforts[231]. Finally, while salts play an important role in homeostasis, the different adducts can skew the true spatial distribution of the species of interest.

This problem can be resolved through two approaches. The first and most obvious would be a desalting wash to maximize salt removal. This was first demonstrated by Wang *et al.* for PCs with an ammonium acetate wash[232]. This protocol has been adopted for a recent IMS study[233]. Interestingly, the same protocol could also enhance phospholipids in negative ion mode[215], though there is no literature on the effects of salts on lipids detected in the negative ion mode. Despite their simplicity, washes are generally avoided for lipid IMS because of the high risk of lipid delocalization and tissue distortion during the washing procedure. The second approach does the complete opposite. It dopes the sample with even more salt to enhance the formation of a single salt adduct. Both potassium salts[234] and sodium salts[159] have been doped into matrix solutions to successfully simplify the spectrum either by enhancing the particular salt adduct formation or suppressing the formation of other salt adducts[235], though lithium salts[230, 236] were the first to be exploited. In a surprising twist, the addition of an ammonium-based salt, ammonium formate, can also minimize sodium salt adduct formation[191].

Doping samples with salt has added benefits. Salts alter species stability. For example, lithiated species produce more fragmentation than sodiated or protonated species for phospholipids, which is highly exploited for MS/MS analysis[236]. Cesium, on the other hand, stabilizes large molecules with more labile bonds, such as, gangliosides[194, 237]. Salts can also affect the ionization efficiencies of each species. A 2008 study doped 9-AA with sodium acetate for the detection of neutral lipids, notably TAGs[238]. A previous doctoral student in our research group later adapted this protocol for IMS applications[159, 239]. Metallic salts such as silver salts have also been exploited in MALDI MS[240-242] and explored for its IMS potential[145]. However, metal nanoparticles

remain more popular than metal salts for IMS applications[145, 243].

It is also important to consider the counterions when selecting the salt, as they will affect the efficacy and mechanism of salt adduct formation. Griffiths and Bunch surveyed an array of common salt additives and reported that acetate and chloride alkali salts effectively suppressed the formation of other salt adducts without demonstrating any improvements in signal intensity, while nitrate alkali salts favored the formation of adducts with the doped cation[235]. Indeed, of the lithium salts available, Cerruti *et al.* found lithium trifluoroacetate to be the most effective for MALDI IMS of phospholipids in combination with DHB[230], while the most recent sodium-assisted MALDI approach by Dufresne *et al.* specifically determined sodium phosphate or sodium carbonate to be the more effective sodium salt[159]. The counterion can also influence the matrix homogeneity[235], though it appears to be less critical when matrices are applied by sublimation or excessively dry sprays. With so many different factors, salts have an undeniable influence on the MALDI desorption/ionization event and should be carefully taken into strong consideration when preparing samples for IMS and interpreting IMS results.

1.3. Research Objectives

The goal of this thesis is to investigate the effects of salt in three different IMS contexts. The work aims to answer the following questions:

1. What is an effective desalting wash that can be applied to microdissected organs for IMS lipidomic studies?
2. How can ammonium-based salts enhance the detection of gangliosides on thin tissue sections for MALDI IMS?
3. Can silver-based metal salts be used directly as a MALDI matrix for IMS of olefins without the addition of organic matrices?

Chapter 2 responds to the first question by testing a series of desalting protocols on microdissected *Drosophila* Malpighian tubules (MT). Composed of four strands of single cells, this organ tests the limit of desalting washes on an extremely fragile sample. This is especially true for lipidomic studies, where any form of washing can lead to phospholipid delocalization. As such, the goal is to determine a suitable washing protocol that balances between salt removal and phospholipid signal loss due to delocalization or cell rupture. This chapter also examines the possibility of studying the PL distribution of this organ through classical sectioning with high spatial resolution dual-polarity IMS. The aim is to identify PL signals unique to the MTs with regards to other organs so that this structure can be directly distinguished based on ion signals.

Chapter 3 responds to the second question through examining mouse brain sections. While highly abundant in the brain, only the major gangliosides have been readily visualized by MALDI-TOF IMS. The goal is to elaborate a sample preparation protocol that applies ammonium-based salts to enhance the overall ganglioside signals on these sections compared to standard MALDI IMS approaches. Specifically, the effects of ammonium-based washes and ammonium-based salt addition were examined separately and in conjunction to determine the protocol that provided the best overall improvement. High spatial resolution IMS were conducted to determine the extent of delocalization caused by the optimal sample preparation protocol.

Chapter 4 answers the last question that seeks to understand the possibility of applying metal salts directly as matrix. This study sought to determine an appropriate silver salt for the IMS of olefins and presents a methodical approach to developing a highly reproducible spray protocol. Specifically, this research examines the degree to which the amount of salt deposition, the silver solution solvent system and the various spray parameters affect the olefin signal intensity and the IMS signal homogeneity. As such, instead of mouse brain sections, this study employs mouse brain homogenates to minimize signal variability from one section to the next. This optimized approach

was compared to the sputtered silver deposition approach previously developed in our laboarotry[146]. High spatial resolution IMS experiments were also conducted to better assess the highest possible spatial resolution attainable.

Chapter 2: Mapping the Fly Malpighian Tubule Lipidome by Imaging Mass Spectrometry

Ethan Yang, Chiara Gamberi and Pierre Chaurand

Journal of Mass Spectrometry, Volume 54, Issue 6, Pages 557-566, June 2019

Author Contributions:

- Ethan Yang conducted the entirety of all imaging mass spectrometry experiments (minus the fly microdissection), analyzed and interpreted the results and put together the manuscript.
- Prof. Chiara Gamberi, co-author, provided the fly samples, conducted the tubule microdissections, and provided guidance and feedback on the manuscript, especially in areas related to fly microdissection.
- Prof. Pierre Chaurand, doctoral supervisor, helped design the experiment and provided feedback and mentorship during the data analysis and manuscript publication process.

2.1. Abstract

Matrix assisted laser/desorption ionization imaging mass spectrometry (MALDI IMS) is an analytical technique for understanding the spatial distribution of biomolecules across a sample surface. Originally employed for mammalian tissues, this technology has been adapted to study specimens as diverse as microbes, cell cultures, food such as strawberries and invertebrates including the vinegar fly *Drosophila melanogaster*. As an ideal model organism, *Drosophila* has brought greater understanding about conserved biological processes, organism development and diseased states and even informed management practices of agriculturally and environmentally important species. *Drosophila* displays anatomically separated renal (Malpighian) tubules that are the physiological equivalent to the vertebrate nephron. Insect's Malpighian tubules are also responsible for pesticide detoxification. In this article, we first describe an effective workflow and sample preparation method to study the phospholipid distribution of the Malpighian tubules that initially involves the manual microdissection of the tubules in saline buffer followed by a series of washes to remove excess salt and enhance the phospholipid signals prior to matrix deposition and IMS at 25 μm spatial resolution. We also established a complementary methodology for lipid IMS analysis of whole-body fly sections using a dual-polarity data acquisition approach at the same spatial resolution after matrix deposition by sublimation. Both procedures yield rich signal profiles from the major phospholipid classes. The reproducibility and high-quality results offered by these methodologies enable cohort studies of *Drosophila* through MALDI IMS.

2.2. Introduction

The *Drosophila melanogaster* (also called vinegar or fruit fly) is a popular model system for investigating the fundamental processes that occur during development and other cellular functions. Despite its tiny size, it shares conserved basic biological, physiological and neurological properties with mammals[177, 178]. The relative ease of inducing mutant variants and large genetic collections empowered applications in studying genetic basis of disorders, ranging from neurological diseases, such as amyotrophic lateral sclerosis (ALS), Parkinson's and epilepsy[244, 245] to other applications, such as diabetes, metabolism[246] and even drug screening[178]. With 75% homology at the gene and pathway level, the list continues to grow[174, 175, 247].

Matrix-assisted laser desorption/ionization imaging mass spectrometry (MALDI IMS) is a powerful technique that can provide information on the spatial distribution of lipids, proteins and metabolites found within a sample tissue[108-110, 115, 214, 248-250]. While highly employed for studying mammalian tissues, MALDI IMS has gained traction for investigating invertebrates such as mollusks, snails, crabs [251-253] and insects ranging from bees and beetles to cockroaches and mosquitoes[172, 254-256].

The first IMS publication of *Drosophila* by Niehoff *et al.* in 2014 characterized organ-specific distributions of phospholipids and triacylglycerols on cross sections of the entire fly[179], followed by a broader study by the Spengler's group in 2017 that included fatty acids and other metabolites[180]. While these publications provided a strong basis for future IMS studies, neither focused on the *Drosophila* renal system, particularly the Malpighian tubules. Functionally equivalent to the human nephron, the tubules branch out from the junction between the mid and hindgut and are the fly's detoxification and filtering system consisting of two tubule pairs. Each tubule is made of arrays of single cells facing each other[257]. The seemingly simple organ has been

found to display great functional complexity, making it a viable model for various renal diseases[257]. Examples include nephrolithiasis, or kidney stones, and polycystic kidney disease (PKD), an uncurable degenerative genetic malady that leads to kidney failure in 50% of the patients[176, 257]. To our knowledge, this is the first report of MALDI IMS analyses dedicated to the *Drosophila* Malpighian tubules.

In this work, the development of two complementary IMS approaches for studying the *Drosophila* tubule lipidomics is presented. The first protocol employed whole tubule pairs microdissected in buffered solution prior to matrix deposition and IMS analysis. This method analyzes analyses of the entire organ at once and allows for comparison of lipid expressions in physiologically distinct regions along the tubule length. The second protocol featured classical whole-body sagittal cryosectioning of the fly as conducted previously, with a novel targeted effort to detect and characterize the tubules. We detail here the sample preparation protocol for each approach and compare as well as discuss the results obtained with the two methods.

2.3. Experimental

2.3.1. Materials & Reagents

Matrices and salts, specifically, 1,5-diaminonapthalene (DAN), 2,5-dihydroxybenzoic acid (DHB), ammonium formate (AF), ammonium acetate (AA), ammonium bicarbonate (AB), were obtained from Sigma-Aldrich Canada (Oakville, ON). Phosphate-buffered saline (PBS) and 1X PBS with 0.1% Tween (PBT) were made in house using standard protocols. The embedding media, Richard-Allan Scientific Neg-50 Frozen Section Medium (OCT), gelatin and carboxymethyl cellulose (CMC), the Jazzmix *Drosophila* food as well as all remaining solvents were purchased from Thermo Fisher Scientific (Ottawa, ON). The Jazzmix is a prepared mixture of brown sugar, corn meal, yeast, agar, benzoic acid, methyl paraben and propionic acid.

2.3.2. Malpighian Tubule Microdissection Protocol

Oregon^{R} wild-type flies were grown on cornmeal agar (Jazzmix) at room temperature (~23°C). Zero to two days old flies were collected and passed into fresh vials every two days until 7-9 days old. The flies were anesthetized with CO_2 and the Malpighian tubule pairs with a section of the connecting hindgut were micro-dissected in 1X PBS. Upon microdissection, the tubules were dipped in a 10 µL drop of PBS and slowly distended on poly-lysine coated indium-tin-oxide (ITO) coated slides (Delta Technologies, Loveland, CO) using ultrafine forceps (Dumont nb. 5). For minimal sample disturbance, excess buffer was removed first with a thin pipette tip and then a capillary (see **Supplemental Table 2-1** for poly-lysine coating protocol). The sample was then subject to two more washes: 40% glycerol (v/v) followed by cold 150 mM ammonium acetate. In both cases, a 20 µL drop of the solution was deposited onto the sample for 15 seconds and removed with a micropipette equipped with a small tip. The sample was then dried in a desiccator for ~1 hr. Other microdissection buffers (1X PBT, 50 mM AF, 50 mM AA and 50 mM AB) and sample washing solutions (150 mM AB and 150 mM AF) were also tested for comparison. A general workflow of the microdissection protocol is summarized in **Figure 2-1**.

2.3.3. Fly Embedding and Cryosectioning Protocol

Flies grown in the same condition as those above were used for these experiments. After anesthesia with CO_2, flies were flash frozen on dry ice and stored at -80°C until embedding. For embedding, frozen flies were submerged in optimal cutting temperature (OCT) polymer in an embedding mold. Upon proper sample orientation, the block was placed in a closed container with dry ice for a complete freeze-over. The embedding process usually took less than two minutes. Afterwards, the sample was placed at -80°C overnight before cryosectioning at a thickness of 12 µm at -20°C using a Leica CM3050 cryostat (Leica Microsystems GmbH, Wetzlar, Germany). The

sections were then thaw-mounted onto ITO-coated slides and desiccated for ~1 hr before matrix deposition. Other embedding media found in the IMS literature, namely gelatin and carboxymethyl cellulose (CMC), were also tested for their ease of cyrosectioning, quality of section morphology and quality of MS signals [113, 172, 179, 180, 251, 258].

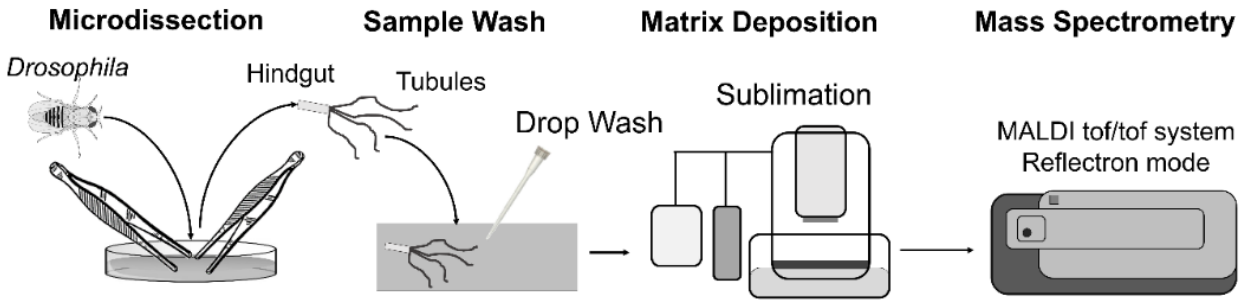

Figure 2-1: Malpighian Tubule MALDI IMS Workflow. Workflow for analyzing the lipid content of fly Malpighian tubules by IMS consists of: 1) A manual microdissection step in PBS to extract the tubules along with a small portion of the hindgut from the animal; 2) The tubule is then carefully placed in a drop of PBS onto a poly-L lysine ITO-coated glass slide and untangled. Excess PBS is removed with a micropipette and capillary, and the tubule washed with two 20 µL drops of 40% glycerol followed by two 20 µL drops of 150 mM ammonium acetate (AA). 3) Upon drying, matrix is deposited onto the slide by sublimation, optically scanned and immediately analyzed by MALDI-TOF IMS.

2.3.4. MALDI IMS Sample Preparation

For microdissected Malpighian tubules, approximately 200 µg/cm^2 of either DHB or DAN matrix was deposited onto the samples by sublimation for data acquisition in positive or negative mode, respectively, according to previously published protocols[60]. In our case, the temperature and pressure were kept constant at 180°C and 0.5 mbar throughout the experiments. The same protocol was used to deposit approximately 150 µg/cm^2 of DAN matrix onto fly sections for positive and negative ion data acquisition. Matrix thickness was calculated by measuring the weight of the slides

before and after matrix deposition and by dividing the difference by the area subjected to sublimation. Hematoxylin and eosin (H&E) staining was performed on the microdissected tubules post mass spectrometry after matrix removal in 95% ethanol solution (the detailed protocol is given in Supplemental Table 2-2)

2.3.5. MALDI-TOF Mass Spectrometry

Profiling and IMS of all samples were performed using a MALDI-TOF/TOF ultrafleXtreme mass spectrometer in reflectron geometry (Bruker Daltonics, Billerica, MA). This particular model is equipped with a 1 kHz SmartBeam II Nd:Yag/355 nm laser that has a focus of ~15 μm in diameter for the "minimum" focus setting. To acquire the MS and IMS data, flexControl 3.4 and flexImaging 4.1 were used, respectively (Bruker Daltonics, Billerica, MA). For the MS data, on-tissue measurements were obtained from the microdissected tubules whereas off-tissue measurements were acquired to 1~2 mm adjacent to the length of the tubules. Visualization and localization of the samples were confirmed with flexImaging 4.1 that allows for the matching of the scanned image of the samples to the actual target position in the instrument. The same function was applied for IMS data to select the region of interest. Unless otherwise stated, the following instrumental parameters were used throughout the entire study. First, the acceleration voltage was set to +25 or −20 kV for data acquisition in the positive or negative ion polarity respectively, while all other instrumental parameters (delayed extraction parameters, source voltages, detector gain, laser energy, etc.) were optimized for maximum S/N over the *m/z* 500 – 1000 range. Second, the number of shots for every MS spectrum and per IMS array position was kept at 150 for both ion polarities. Third, IMS measurements of the microdissected tubules were acquired at a lateral spatial resolution of 25 μm, while IMS measurements were performed at the same spatial resolution but acquired across the entire fly cross section using a dual polarity strategy as described in Thomas *et*

al.[60] In short, IMS measurements in both ion polarities are acquired for the same section with an offset between the positive and negative array grids; in this case, a 12-µm offset was applied. Lastly, external calibration was carried out using a known lipid signals from liver homogenate to obtain five points of calibration over the considered mass range. This resulted in a mass accuracy of 40 ppm or better for all on-tissue measurements.

Finally, putative assignments for observed phospholipid signals were determined by comparing mass measurements with the LIPID MAPS prediction tool (http://www.lipidmaps.org/tools/index.html), previous literature and by MALD MS/MS using the LIF-TOF/TOF instrument mode[167, 179, 180].

2.3.6. IMS Data Analysis

IMS data were exported into the vendor neutral imzML format and visualized in the R environment (v3.4.1) using the Cardinal package (v2.1) [224]. All images presented were normalized linearly and contrast enhanced using the option "suppression," an option in Cardinal to reduce the effects of hotspots. The same package was also used to run an unsupervised ion distribution segmentation analysis. For this analysis, data was preprocessed to remove all signals below a S/N of 3 found in less than 0.0001% of all spectra. Afterwards, spatial shrunken centroids clustering was employed to obtain the segmentation of the data [259]. The parameters for the smoothing radius (r), the number of cluster (k), and the shrinking parameter (s) were determined based on the histology and kept constant throughout the sample set. The package RegCombIMS was used to combine the positive and negative IMS datasets from the same section before statistical analysis[260].

2.4. Results & Discussion

The following sections detail the optimization process along each step of IMS sample preparation for microdissected fly Malpighian tubules and whole-body cryosections. For each step,

no strict statistical analyses were conducted; however, the results described below are all based on triplicate analyses. Representative qualitative results are presented.

2.4.1. Buffer Selection for Malpighian Tubule Microdissection

First, the ease of tubule microdissection using different buffer systems were compared. Microdissection in ammonium-based buffers, even at lower isotonic salt concentrations (50 mM), were found to cause tubule hardening and tubule breakage. Overall, the tubules were much more difficult to manipulate than those microdissected in tissue-friendly phosphate-based buffers (PBS or PBT), making it difficult to obtain high quality reproducible results suitable for cohort studies. On the other hand, excess salts have been known to degrade signals in MALDI experiments[261]. Moreover, some signal delocalization was observed for samples in both PBS and PBT, marked by the presence of phospholipid signals off-tissue. However, to preserve crucial sample integrity, PBS, the phosphate-based buffer causing less signal delocalization, was chosen for microdissection. Spectral results of this section are summarized in Supplemental Figure 2-1 for positive ion mode and Supplemental Figure 2-2 for negative ion mode for both on-tissue and off-tissue measurements.

2.4.2. Sample Washing Wash Optimization for Microdissected Malpighian Tubules

Washing procedures were also investigated to minimize ion suppression and ion delocalization effects from the 1X PBS microdissection buffer. Initial tests with deionized water to remove excess salt as suggested in the literature caused the tubules to coil, extrude their contents, harden and fragment[258]. Therefore, three MALDI-friendly ammonium-based solutions at physiological salt concentration (150 mM) were tested. Of these, AF-washed tubules displayed the least amount of remaining MS lipid signals. In addition, a greater number of delocalized signals were detected from AF-washed tubules. After AA- and AB- washes, MS signal quality and

intensity were comparable in positive ion mode, with a slightly higher number of signals detected in the former. In negative ion mode, signals from AB-washed tubules were found superior to AA-washed tubules in overall intensity, but overall spectral patterns remained similar. From here, the sample quality was examined. AB-washed tubules turned white after washing and occasionally detached from the slide. In contrast, AA-washed tubules did not turn white and adhered to the slides more consistently. Furthermore, AA has been previously reported in the literature to enhance phospholipid signals in negative mode [215]. AA was therefore chosen as the washing buffer. Spectral results of these washing procedures from a representative sample are shown in Supplemental Figure 2-3 for the positive ion mode and Supplemental Figure 2-4 for the negative ion mode.

Despite promising results from the ammonium-based washes, a solution was needed to help stabilize the tubules on the slides during the washing step and poly-L lysine ITO-coated slides were chosen. While there are options for different fixatives in the IMS insect literature, these were optimized for cryosectioned, rather than microdissected, samples[179, 180]. Indeed, attempts to fix the samples with these solutions (i.e., ethanol, chloroform) led to significant signal loss in negative ion mode and minimal improvements in positive ion mode (data not shown). As such, a different approach was necessary and a 30% glycerol solution in artificial seawater wash described in the IMS literature to stabilize neurons was adapted for the tubules[253, 262]. It was chosen because of their similar fragile nature. Upon comparing washes with 30%, 40% and 50% glycerol solutions (v/v in water), 40% glycerol was found to be optimal (see Supplemental Figure 2-5). It removed the most amount of salt whilst limiting species delocalization and was also relatively easy to wash away by rinsing the tubules with 150 mM AA drops.

2.4.3. Matrix Selection for Microdissected Malpighian Tubules

Several matrix candidates for the detection of phospholipids included DAN or DHB for positive ion mode, and DAN or 9AA for negative ion mode [60]. For matrix deposited by sublimation, the signal quality from DAN in positive mode upon the introduction of phosphate-based buffer washes remained poor, with fewer signals detected when compared to DHB (see panel 3 and 4 in Supplemental Figure 2-1). The DAN matrix, however, was sufficient for negative ion mode (see Supplemental Figure 2-2). 9-AA was not fully tested because it is known to be less suited for phospholipids than DAN when sublimated[60].

Based on these findings, the following optimized protocol was adapted for IMS of microdissected tubules: tubule microdissection in 1X PBS buffer, sample placement on poly-lysine ITO-coated slide, wash in two drops of 20 µL 40% glycerol, drop wash with 150 mM AA, and deposition of DHB (positive ion mode) or DAN (negative ion mode) by sublimation. The MS and IMS results from these samples are described in the next section.

2.4.4. On-tissue characterization of Microdissected Malpighian Tubules

The microdissected Malpighian tubule is rich in signals, as seen in **Figure 2-2**. In positive ion mode, the tubule signals are dominated by three sets of peaks between *m/z* 700 – 850. Based on the exact mass, MS/MS data and previous publications, most of these belong to the phosphatidylcholine (PC) family [179, 180]. The same can be said of the hindgut. In the negative ion mode, signals are mostly dominated by phosphatidylethanolamines (PEs) and phosphatidylinositols (PIs), followed by much weaker signals for phosphatic acids (PAs) and phosphatidylglycerol (PGs). There are some spectral differences between the tubules and the hindgut, most notably in the presence of lower mass species between *m/z* 600 – 700 in the hindgut region. A table with tentative lipid assignments of the major species observed based on their

MS/MS profile can be found in **Supplemental Table 2-3**.

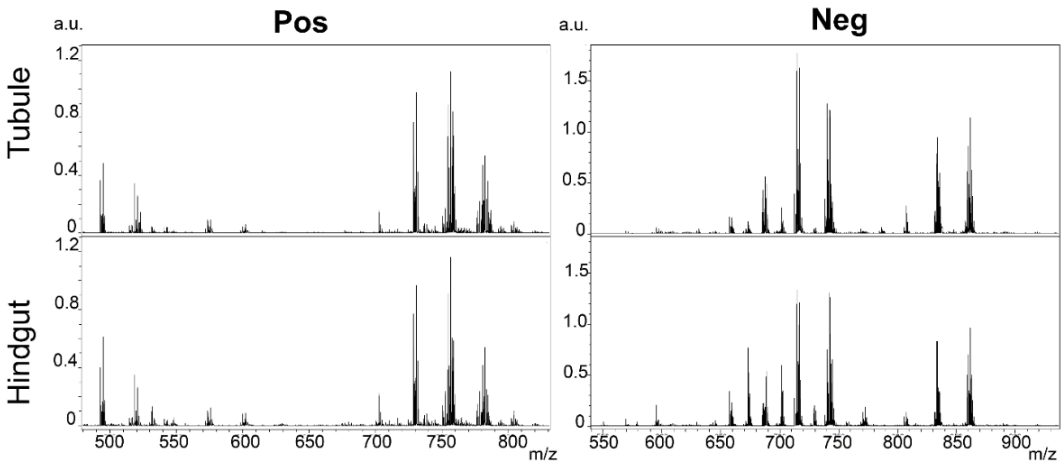

Figure 2-2: Positive and Negative ion Polarity MALDI-TOF MS Lipid Profiles. Acquired from Microdissected Malpighian Tubules and the Hindgut. DHB matrix was used to acquire the data in the positive ion mode, while DAN was used for the negative ion mode. The overall MS profiles between the tubules and the hindgut remained highly similar. In the positive mode, there is no obvious distinction, whereas in negative mode, the hindgut had more species below m/z 700 compared to the tubule.

With hints of differential species distribution, it is of interest to assess if there is any phospholipid signal colocalizing to the tubule or hindgut region. This can be achieved through spatially-aware segmentation analysis that clusters signals based on their spatial distribution and relative intensity. In positive ion mode, the first round of spatially-aware segmentation analysis revealed only two meaningful segments: the background signal and the microdissected tubule sample (results not shown). An increased number of segments of the entire IMS data led to greater divisions in the background due to the presence of random residual salt patterns. To better segment the positive mode data, the background segment was removed, and the remaining "sample" was further clustered. As shown in **Figure 2-3**, the tubule clustered into three segments, one for the hindgut, one for the tubules, and a third demonstrating "edge effects" around the entire sample.

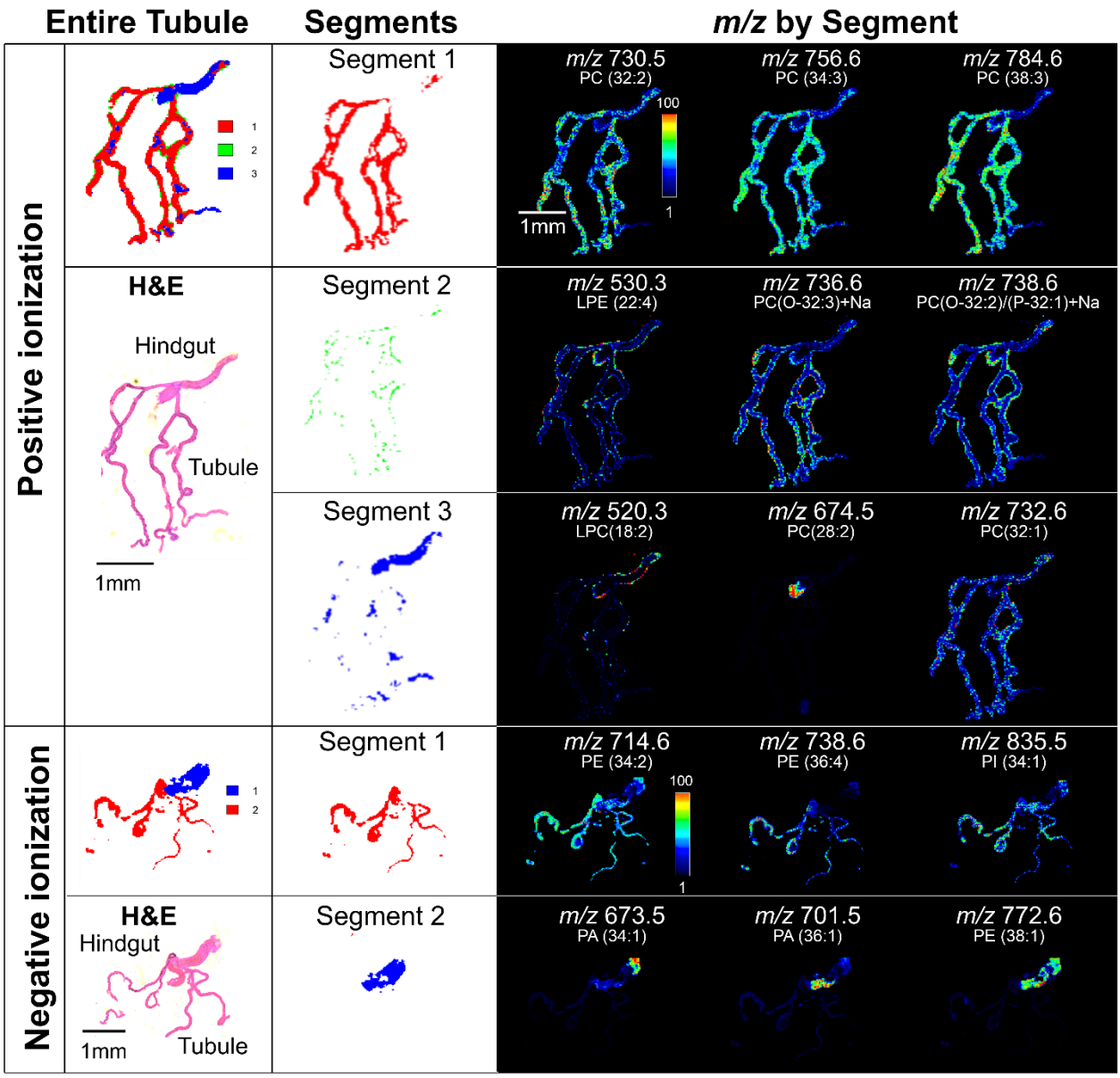

Figure 2-3 MALDI IMS Results of Microdissected Malpighian Tubules. Positive ionization (top panel) and negative ionization (bottom panel) mode lipid IMS results from representative microdissected tubules. Spatially-aware centroid shrunken untargeted segmentation results and corresponding H&E stainings are shown in the first column, the breakdown of each segment are shown in the second column and three representative IMS results of each segment are shown the last column. Putative assignments based on exact mass and MS/MS for each species are given. Unless otherwise noted, all positive ion species are [M+H]+ and negative ion species [M-H]-

Based on the top markers from the segmentation results, the hindgut and tubule clearly shared more similarities than differences, since the results for Segment 3 mostly consisted of signals not localized to the hindgut. A deeper investigation into the signals from Segment 3 in fact, showed that they were generally localized throughout the entire background, suggesting that despite the extreme care taken to minimize delocalization, some species appeared to have nonetheless migrated. This may not come as a surprise because hydrophobic species such as triacylglycerols are soluble in the glycerol solution and would probably tend to migrate during the glycerol washes, as suggested by the relatively clean off-tissue spectra with 150 mM AA wash alone shown in the top right panel of **Supplemental Figure 2-3** and the top panel of **Supplemental Figure 2-4**. The subsequent introduction of water-based solvents could then lead to the potential delocalization of the more hydrophilic phospholipids.

A similar observation was made in negative ion mode, whereby the signals from the Malpighian tubules were dominated by higher molecular weight species (*m/z* 700 – 900), while the hindgut was dominated by lower molecular species (*m/z* 600 – 700). In the Malpighian tubule, PEs and PIs were the major species detected and identified, whereas PAs were found to be more localized to the hindgut. For the negative ion mode data, the tubule and the hindgut segmented cleanly without the need to remove the background segment. Further signal segmentation of the negative ion data did not yield additional information. The negative ion mode results are also presented in Figure 2-3. A noteworthy observation from both positive and negative ion mode data is that all the tubules clustered into one segment, despite there being two distinct sets of tubules, one in the anterior and another in the posterior position. The results therefore suggest that the different tubules appeared to have similar or identical phospholipid expressions.

2.4.5. Choice of Embedding Medium and Matrix for Fly Sections

Fly embedding proved to be straightforward. It was possible to manipulate and place the flies in the desired orientation in all cases. This was true even when using 5% CMC, the most viscous of the tested embedding media. The difference was noticeable, however, during cryosectioning. While 20-µm thick sections as described in the literature were easily attainable with all media, consecutive 12-µm sections were only feasible after embedding in OCT. At this thickness, the CMC and gelatin did not hold the flies tightly enough during cryosectioning, leading to poor section recovery. Therefore, to demonstrate results from thinner sections, OCT was used.

An issue with OCT noted in the literature is the presence of contaminating MS peaks coming from this medium [258]. While this may be the case for native peptide analyses or for protein analyses without sample washing steps, the overall MS signals from the OCT-embedded fly sections had just as much, if not greater, overall intensity, quantity and mass resolution, as those embedded in the other tested embedding media (see Supplemental Figure 2-6). To ensure high quality sections, the orientation and quality of the embedding was important. In short, the media had to be free of air bubbles, the OCT block had to be precisely rectangular, and the cut should be made from the abdomen towards the head. For reproducibility and the generation of serial sections, removing the wings as per Khalil *et al.* was found helpful[180].

The matrices were selected using the same rationale as for the microdissected tubules. In other words, DAN and DHB were the most suitable candidates for sublimation for positive mode, whereas DAN would be favored for negative mode. Spectral results from the entire fly section suggested DHB was suitable for positive mode (see Supplemental Figure 2-6). However, because the DAN matrix allows for dual-polarity IMS experiments on the same section, it was ultimately chosen and overall provided richer IMS data[60].

2.4.6. On-tissue Characterization of the Fly Sections

Dual polarity lipid IMS results acquired from a *Drosophila* fly whole-body tissue section are presented in Figure 2-4. Similar to the microdissected tubules, the positive and negative ion mode sum spectra displayed a great abundance of phospholipid signals in the *m/z* 700 – 900 range. In the positive ion mode, the majority of identifiable signals came from PCs, the main component of the cellular membrane. In negative ion mode, the most intense signals observed consisted of a distribution of PEs and PIs. Like microdissected tubules, PAs and PGs were also observed. Unlike the microdissected Malpighian tubules, analyses of whole-body sections displayed overall more signals across the phospholipid mass range, most likely due to differential phospholipid expression of the various organs that are simultaneously present in one tissue section. For each ion polarity, the ion density maps of the three most intense ions hinted at such unique distributions (Figure 2-4).

Segmentation analysis of the combined dataset corroborated colocalization of ion species to major fly anatomical regions. Summarized in Figure 2-5, ion species were localized to the head and thorax (green), the brain, lower thorax and upper abdomen (orange), the muscular region at the top of thorax (purple), the lower abdomen (grey), the extremities around the fly (red) and the legs and wings (blue). While nine segments could be generated, only these six were correlated to the anatomy. The other three were mostly consisting of noise and matrix signals or did not have patterns that matched the segment representation. This indicates that matrix and other patterned background signals impacted the segmentation analysis with noise that led to unnecessary clusters. The same segmentation analysis after having discarded wings and legs confirmed the presence of six major segments, indicating that the original segmentation analysis, despite the background noise, was valid (see Supplemental Figure 2-7). It is interesting to note that the top ion markers in the microdissected tubules were colocalized in different segments, explaining why there were no

m/z signals found to be unique to the fly tubules despite many attempts and approaches. This is not surprising, given that previous research on invertebrates, including *Drosophila,* have either not identified signals specific to the Malpighian tubules or found lower mass metabolites rather than higher mass lipid signatures as a defining feature of this organ[180, 254, 263]. It is also important to note

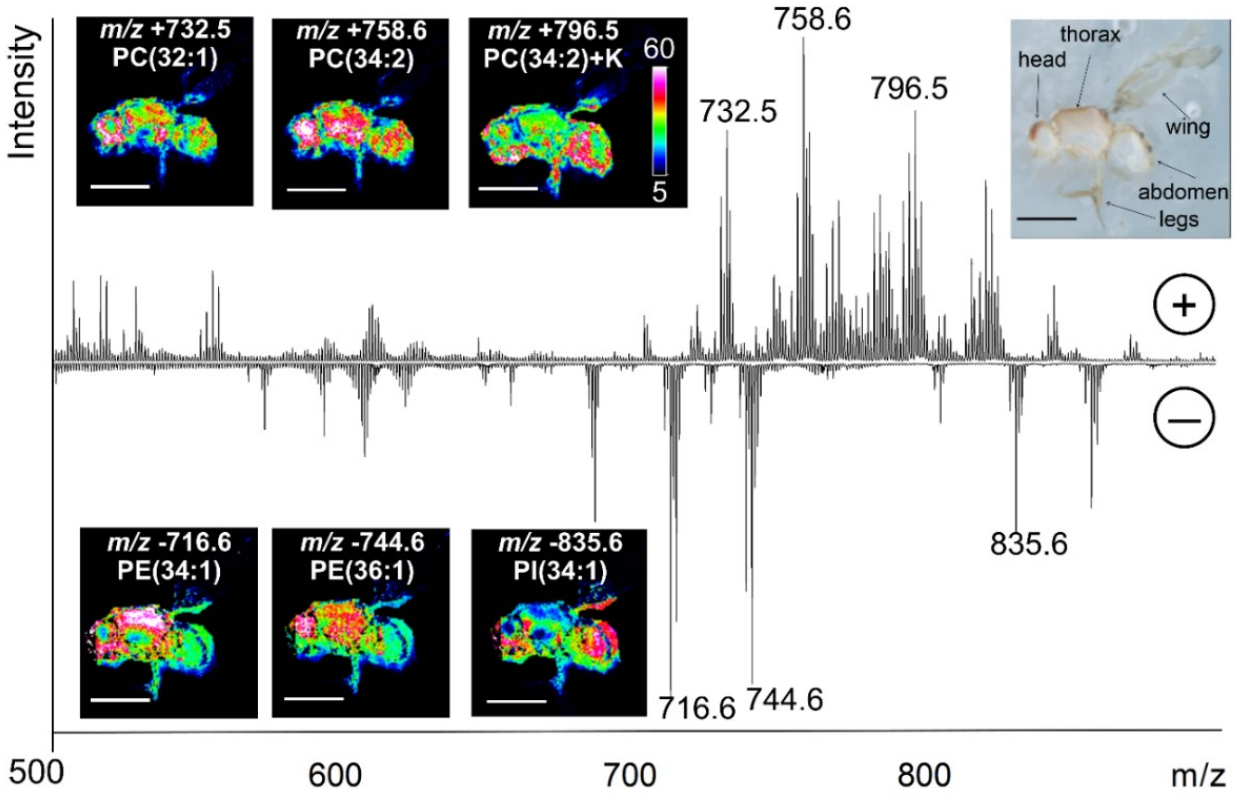

Figure 2-4: Dual Ion Polarity MALDI IMS acquired from a Whole-body Drosophila Section. The IMS data was acquired at 25 µm spatial resolution with a 12 µm offset in the x and y direction allowing dual polarity imaging. The optical image of the section is shown in the top right insert. The mean IMS spectra for both polarities reveal a high abundance of signals from m/z 500-900 corresponding to the phospholipid range. For each polarity, ion density maps of the three highest intensity species are also displayed with the corresponding peaks identified in the spectra. Scale bar indicates 1 mm. Unless otherwise noted, all positive ion species are $[M+H]^+$ and negative ion species $[M-H]^-$.

here that previous publications suggest the presence of phosphatidylserines (PSs)[179, 180]. Our instrument does not have enough mass resolution to differentiate most PSs from PCs in positive ion mode. Further, the exact mass given by the instrument and form of the peaks suggest PCs to be the dominant species. In negative ion mode where these species were observed previously with DAN, no PSs were detected either[60].

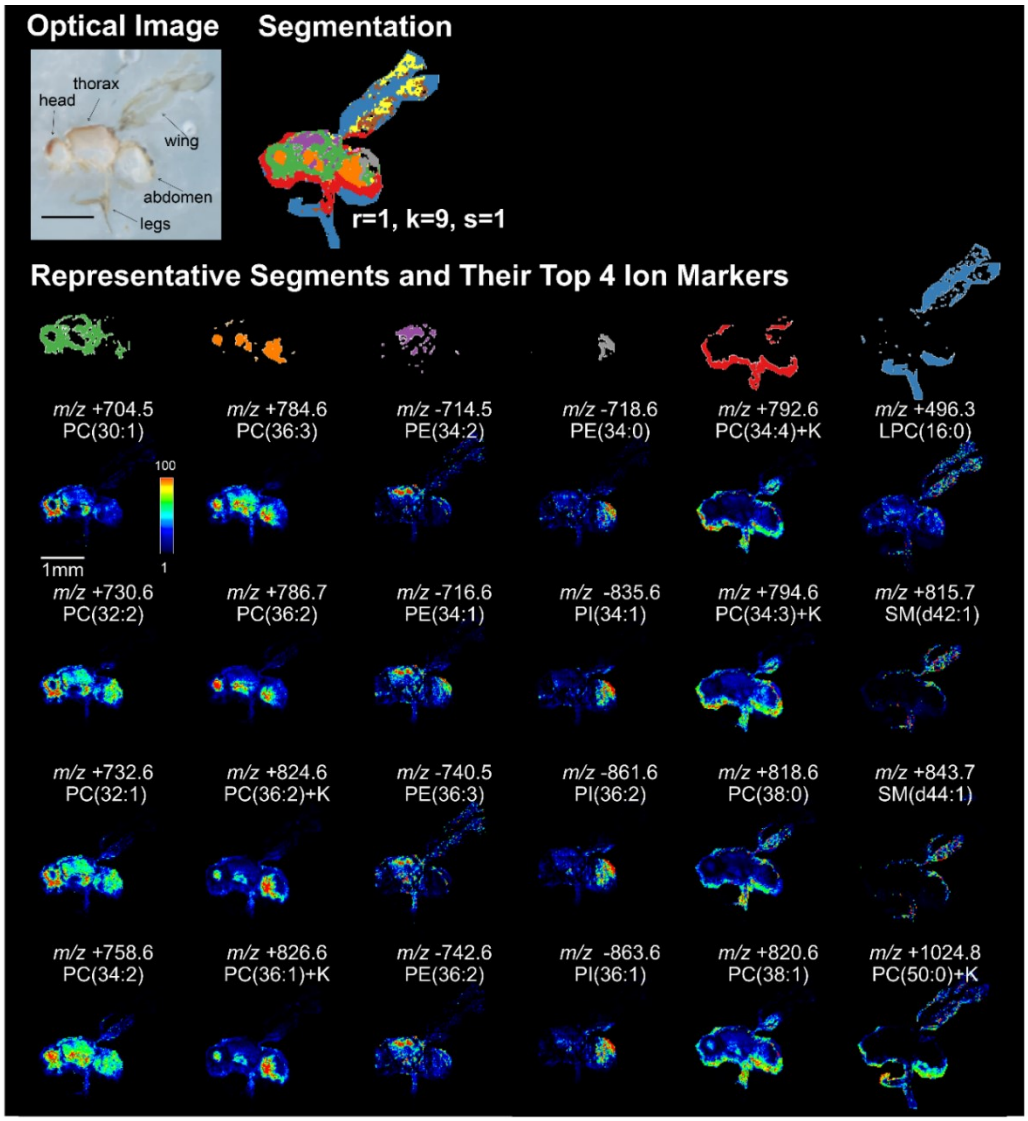

Figure 2-5: Dual Ion Polarity MALDI IMS acquired from a Whole-body Drosophila Section. The IMS data was acquired at 25 µm spatial resolution with a 12 µm offset in the x and y direction allowing dual polarity imaging. The optical image of the section is shown in the top left insert. Segmentation results (along with the parameters used) were generated after combining the positive

and negative polarity IMS data. Of the nine segments generated (three are different patterns of noise), six showed represent IMS signals co-localized to different regions of the fly. Individual segments and the corresponding top four ion markers are also shown. Putative assignments based on exact mass and MS/MS for each species are given. Unless otherwise noted, all positive ion species are $[M+H]^+$ and negative ion species $[M-H]^-$.

2.4.7. Advantages and Limitations of Each Approach

Both microdissected tubules and fly sections provided quality lipidomic data. However, each presents their own advantages and challenges. Microdissected tubules provide information on the entire organ in one IMS experiment, whereas 50 to 80 perfect serial sections would be needed to obtain the same information in three dimensions, provided that the tubules can be identified within each section. While this could be potentially achieved via reporter gene expression[264], this limitation renders the cyrosectioning approach cumbersome. With effective tubule visualization within the sections, its lipidomic content could be contextualized and understood in relation to the rest of the organism. In this case, cryosectioning could be favored over microdissection because of its minimal sample preparation and manipulation, greatly reducing signal delocalization or loss. In terms of spatial resolution, cryosectioning also has an upper hand. The application of matrices that require less ionization energy such as DAN has allowed for dual-polarity experiments at 25 µm with minor overlaps in the ablation area (see Supplemental Figure 2-9) in the positive and negative ion polarity array grids. Moreover, no noticeable signal intensity loss was found when compared to results from serial sections acquired in a single polarity at the same spatial resolution. Based on the work of Kaya *et al.*, dual polarity IMS acquired at a 10 µm spatial resolution may be possible without an offset[166]. On the other hand, microdissected tubules were limited to 25 µm spatial resolution because the multiple washing steps involved have led to a certain degree of species

delocalization. Overall, we found that due to uneven removal of glycerol, excessive washing, sample warping during wash and other potential preparation artefacts, ~1/3 of the microdissected tubules were lost or unsuitable for IMS analyses. Although fly samples are typically abundant, a non-negligible number of samples are currently wasted, implying the need for a proportionally higher number of samples for cohort studies. Regardless, the microdissection method eliminates the difficulty to identify the Malpighian tubules in the cryosections and enables higher analysis throughput.

2.5. Conclusions

In this work, we have demonstrated two different approaches for obtaining lipidomic information about the *Drosophila* fly renal system through IMS. The first allows for detection and IMS of numerous phospholipids at spatial resolutions as low as 25 μm and consists of extracting the Malpighian tubule from the fly through microdissection in PBS, followed by washes in 40% glycerol and 150 mM of ammonium acetate, and MALDI matrix deposition by sublimation (DHB or DAN for positive or negative ion mode IMS analyses, respectively). The second approach is whole-body cyrosectioning of flies embedded in OCT at a thickness of 12 μm followed by DAN matrix deposition by sublimation. This protocol allows for dual ion polarity detection and IMS of phospholipids at 25 μm spatial resolution (and possibly higher), as well as the simultaneous analysis of all the major organ compartments of the fly. However, this approach makes it nearly impossible to unambiguously identify the tubules among all the other organs present in the abdomen at present. Hence, we recommend the microdissection approach to study the *Drosophila* renal system and potentially other organs of interest. Finally, while the work presented herein is focused on phospholipids, the same sample preparation protocols can be adapted for IMS analyses of other biomolecules such as proteins, peptides and other metabolites. This may be more

accessible for whole-body cryosections rather than the microdissected tubules due to some signal delocalization and species loss during the washing steps. The development of these methods will provide even richer information about the molecular composition of the Malpighian tubules from flies of different genotypes or subjected to different treatments.

2.6. Acknowledgements

EY and PC acknowledge funding from the Natural Sciences and Engineering Research Council of Canada (NSERC Post-graduate scholarship-Doctoral and Discovery grant, respectively). CG is the recipient of a Professional Development Award from the Concordia University Part Time Faculty Association (CUPFA, www.cupfa.org).

2.7. Supplemental Information

Supplemental Table 2-1: Poly-Lysine Application Protocol.

Step	Solution	Time
1	Spread 1mL of 0.01% (w/v) poly-lysine on ITO slide	5 mins
2	Immerse in de-ionized water	30 seconds
3	Air dry	As needed

Supplemental Table 2-2: H&E Protocol. Detailed protocol for H&E staining as optimized for the microdissected tubule samples.

Step	Solution	Time
1	95% ethanol	30 seconds
2	70% ethanol	30 seconds
3	De-ionized water	30 seconds
4	Gill 3 Hematoxylin	15 seconds
5	De-ionized water	10 seconds
6	0.007% Sodium Bicarbonate in H_2O	5 dips
7	70% ethanol	30 seconds
8	95% ethanol	30 seconds
9	Eosin	5 dips
10	95% ethanol	30 seconds
11	100% ethanol	30 seconds
12	Air Dry	30 minutes
13	Mount slide with Cytoseal	NA

Supplemental Table 2-3: Putative Assignments of the Top 65 Phospholipid Signals by MS/MS. The table provides mass error in PPM, the proposed identification, and diagnostic fragments of the 30 identified m/z species from negative ionization and 35 from positive ionization mode. Previous literature confirming the identification is cited (right).

Experimental *m/z*	**Calculated m/z**	**Error PPM**	**Proposed Species**	**Adduct**	**Diagnostic Fragment(s)**	**Previous Literature**
569.29	569.27	-35	LPI(16:1)	$[M-H]^-$	241	Pi *et al.*[167]
595.30	595.28	-34	LPI(18:2)	$[M-H]^-$	241	Pi *et al.*[167]
619.30	619.28	-32	LPI(20:4)	$[M-H]^-$	241	Khalil *et al.*[180]
671.54	0.00	0	PA (34:2)	$[M-H]^-$	153	Khalil *et al.*[180]
673.50	673.48	-30	PA (34:1)	$[M-H]^-$	153	NA
688.50	688.49	-15	PE(32:1)	$[M-H]^-$	140	Khalil *et al.*[180]
701.50	701.51	14	PA(36:1)	$[M-H]^-$	153	Khalil *et al.*[180]
714.50	714.50	0	PE(34:2)	$[M-H]^-$	140	Khalil *et al.*[180]
716.50	716.52	28	PE(34:1)	$[M-H]^-$	140	Khalil *et al.*[180]
718.55	718.53	-28	PE(34:0)	$[M-H]^-$	140	Khalil *et al.*[180]
721.52	721.50	-28	PG(32:0)	$[M-H]^-$	171	Khalil *et al.*[180]
730.59	730.57	-27	PE(36:0)	$[M-H]^-$	140	NA
738.50	738.50	0	PE(36:4)	$[M-H]^-$	140	Khalil *et al.*[180]
740.50	740.52	27	PE(36:3)	$[M-H]^-$	140	NA
742.51	742.53	27	PE(36:2)	$[M-H]^-$	140	Khalil *et al.*[180]
744.60	744.59	-13	PE(36:1)	$[M-H]^-$	140	NA
807.55	807.53	-25	PI(32:2)	$[M-H]^-$	241	Khalil *et al.*[180]
809.51	809.51	2	PI(32:0)	$[M-H]^-$	241	Khalil *et al.*[180]
831.53	831.50	-36	PI(34:3)	$[M-H]^-$	241	Khalil *et al.*[180]
833.50	833.51	12	PI(34:2)	$[M-H]^-$	241	Khalil *et al.*[180]
835.55	835.53	-24	PI(34:1)	$[M-H]^-$	241	Khalil *et al.*[180]

837.54	837.55	12	PI(34:0)	$[M-H]^-$	241	Khalil *et al.*[180]
853.50	853.48	-23	PI(36:6)	$[M-H]^-$	241	Khalil *et al.*[180]
855.53	855.50	-35	PI(36:5)	$[M-H]^-$	241	Khalil *et al.*[180]
857.53	857.51	-23	PI(36:4)	$[M-H]^-$	241	Khalil *et al.*[180]
859.55	859.53	-27	PI(36:3)	$[M-H]^-$	241	Khalil *et al.*[180]
861.57	861.54	-35	PI(36:2)	$[M-H]^-$	241	Khalil *et al.*[180]
863.58	863.56	-23	PI(36:1)	$[M-H]^-$	241	Khalil *et al.*[180]
865.56	865.57	14	PI(36:0)	$[M-H]^-$	241	Khalil *et al.*[180]
891.59	891.59	6	PI(38:1)	$[M-H]^-$	241	Khalil *et al.*[180]
494.34	494.32	-20	LPC(16:1)	$[M+H]^+$	184.1	NA
496.34	496.33	-20	LPC(16:0)	$[M+H]^+$	184.1	Patterson *et al.*[265]
520.34	520.33	18	LPC(18:2)	$[M+H]^+$	184.1	Khalil *et al.*[180]
522.34	522.35	6	LPC(18:1)	$[M+H]^+$	184.1	Khalil *et al.*[180]
674.49	674.47	-30	PC(28:2)	$[M+H]^+$	184.1	NA
704.53	704.52	-14	PC(30:1)	$[M+H]^+$	184.1	Khalil *et al.*[180]
706.51	706.53	28	PC(30:1)	$[M+H]^+$	184.1	Khalil *et al.*[180]
728.56	728.55	-14	PE(O-36:3)/PE(P-36:2)	$[M+H]^+$	184.1	Khalil *et al.*[180]
730.52	730.53	14	PC(32:2)	$[M+H]^+$	184.1	Khalil *et al.*[180]
732.54	732.55	14	PC(32:1)	$[M+H]^+$	184.1	Khalil *et al.*[180]
752.50	752.52	21	PC(32:2)	$[M+Na]^+$	184.1	Khalil *et al.*[180]
754.52	754.53	13	PC(34:1)	$[M+Na]^+$	184.1	Khalil *et al.*[180]
756.54	756.55	9	PC(34:3)	$[M+H]^+$	184.1	Khalil *et al.*[180]
758.56	758.56	-5	PC(34:2)	$[M+H]^+$	184.1	Khalil *et al.*[180]
760.59	760.58	-8	PC(34:1)	$[M+H]^+$	184.1	Khalil *et al.*[180]
762.62	762.60	-26	PC(34:0)	$[M+H]^+$	184.1	NA
766.59	766.57	-26	PC(O-36:4)/PC(P-36:3)	$[M+H]^+$	184.1	Khalil *et al.*[180]
774.62	774.60	-26	PE(38:1)	$[M+H]^+$	184.1	Khalil *et al.*[180]
776.60	776.61	13	PC(34:4)	$[M+Na]^+$	184.1	Khalil *et al.*[180]

778.53	778.53	-5	PC(34:3)	$[M+Na]^+$	184.1	Khalil *et al.*[180]
780.57	780.55	-22	PC(34:2)	$[M+Na]^+$	184.1	Khalil *et al.*[180]
782.59	782.56	-33	PC(36:4)	$[M+H]^+$	184.1	Khalil *et al.*[180]
784.60	784.58	-25	PC(36:3)	$[M+H]^+$	184.1	Khalil *et al.*[180]
786.63	786.60	-37	PC(36:2)	$[M+H]^+$	184.1	Khalil *et al.*[180]
788.64	788.61	-38	PC(36:1)	$[M+H]^+$	184.1	Khalil *et al.*[180]
792.50	792.49	-13	PC(34:4)	$[M+K]^+$	184.1	Khalil *et al.*[180]
794.53	794.50	-38	PC(34:3)	$[M+K]^+$	184.1	NA
796.53	796.52	-13	PC(34:2)	$[M+K]^+$	737.5, 184.1, 162.9, 575.5	Khalil *et al.*[180]
814.62	814.63	12	PC(38:2)	$[M+H]^+$	184.1, 86.1	Khalil *et al.*[180]
818.64	818.66	24	PC(38:0)	$[M+H]^+$	184.1	NA
820.55	820.52	-37	PC(38:1)	$[M+H]^+$	184.1	Khalil *et al.*[180]
822.55	822.54	-12	PC(36:3)	$[M+K]^+$	184.1, 763.5	NA
824.53	824.55	24	PC(36:2)	$[M+K]^+$	184.1, 763.5	Khalil *et al.*[180]
826.59	826.57	-24	PC(36:1)	$[M+K]^+$	184.1, 763.5	Khalil *et al.*[180]
980.82	980.80	-20	PC(48:0)	$[M+Na]^+$	184.1	NA

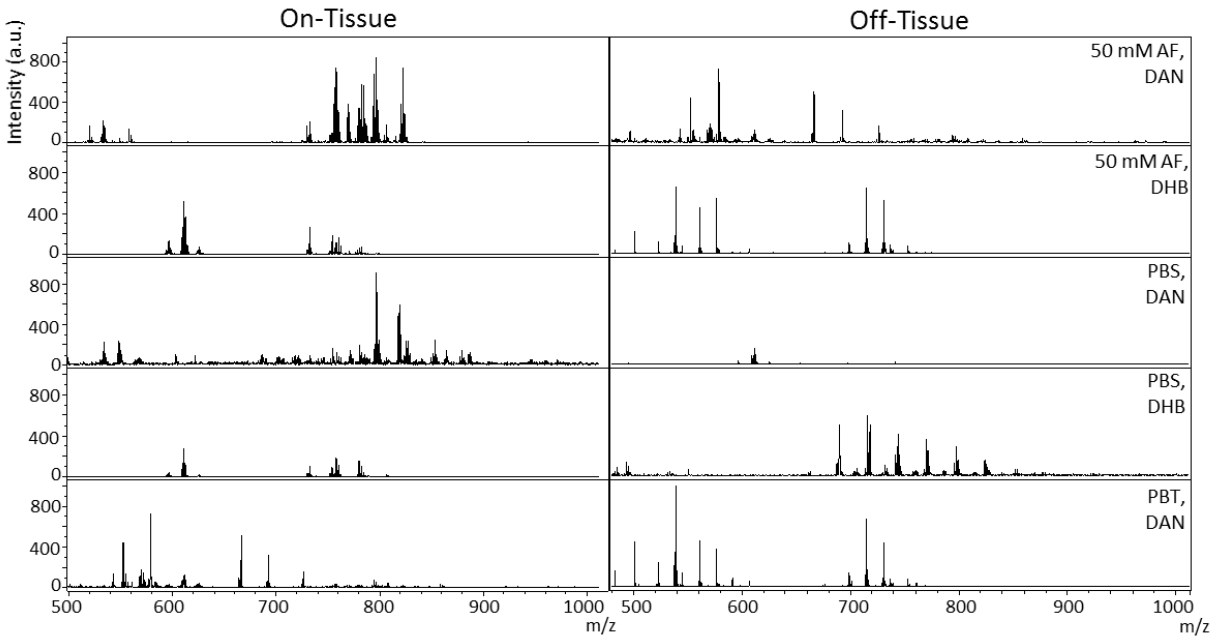

Supplemental Figure 2-1: Positive Ionization MALDI-TOF MS Lipid Profiles Acquired from Microdissected Malpighian Tubules in Different Buffers. Comparative results from the profiling analysis show that, only the 50 mM AF microdissection buffer environment coupled with the DAN matrix yielded acceptable phospholipid signals. All other conditions provided poor signals. Of interest was the strong presence of signals off-tissue after microdissection in PBS and DHB matrix application. Despite 50 mM AF being a good candidate from a MS signal quality standpoint, the difficulty in manipulating the tubules often resulting in degradation and fragmentation was found unpractical, even when AF concentration was increased to 150 mM to match physiological salt concentrations (results not shown).

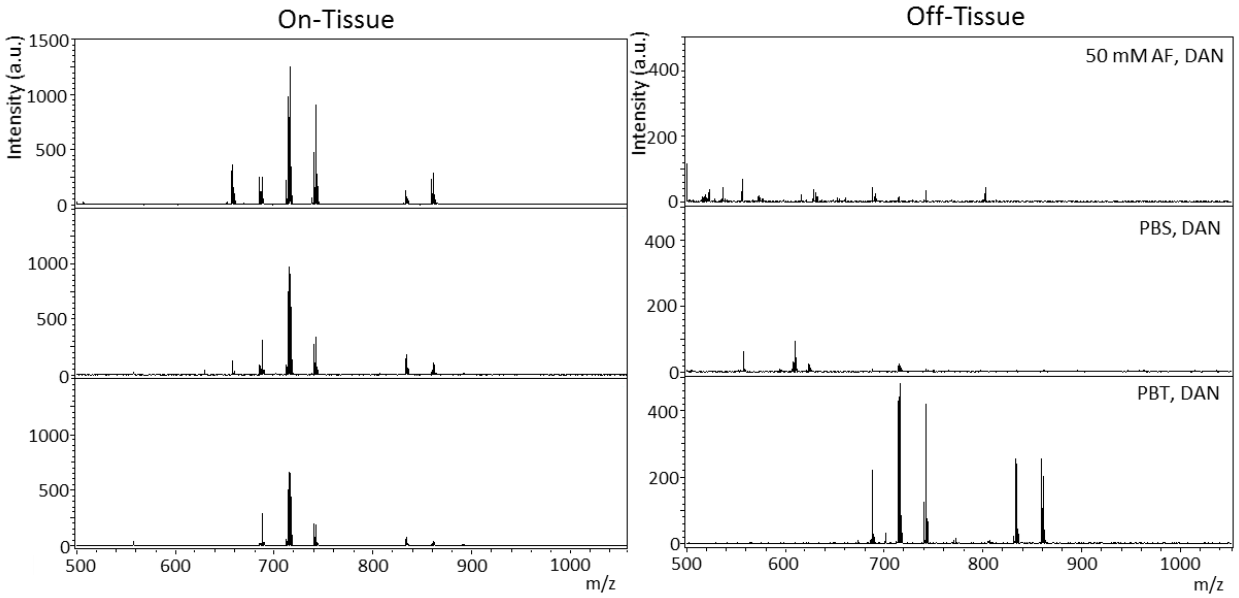

Supplemental Figure 2-2: Negative Ionization MALDI-TOF MS Lipid Profiles Acquired from Microdissected Malpighian Tubules in Different Buffers. Comparative results from the profiling analysis showed similar on-tissue results for the three tested microdissection buffers. Off-tissue MS analyses, however, showed that the PBT buffer led to greater signal diffusion, with the least amount observed for PBS. Despite 50 mM AF being a good candidate from a MS signal quality standpoint, the difficulty in manipulating the tubules often resulting in degradation and fragmentation was found unpractical, even when AF concentration was increased to 150 mM to match physiological salt concentrations (results not shown).

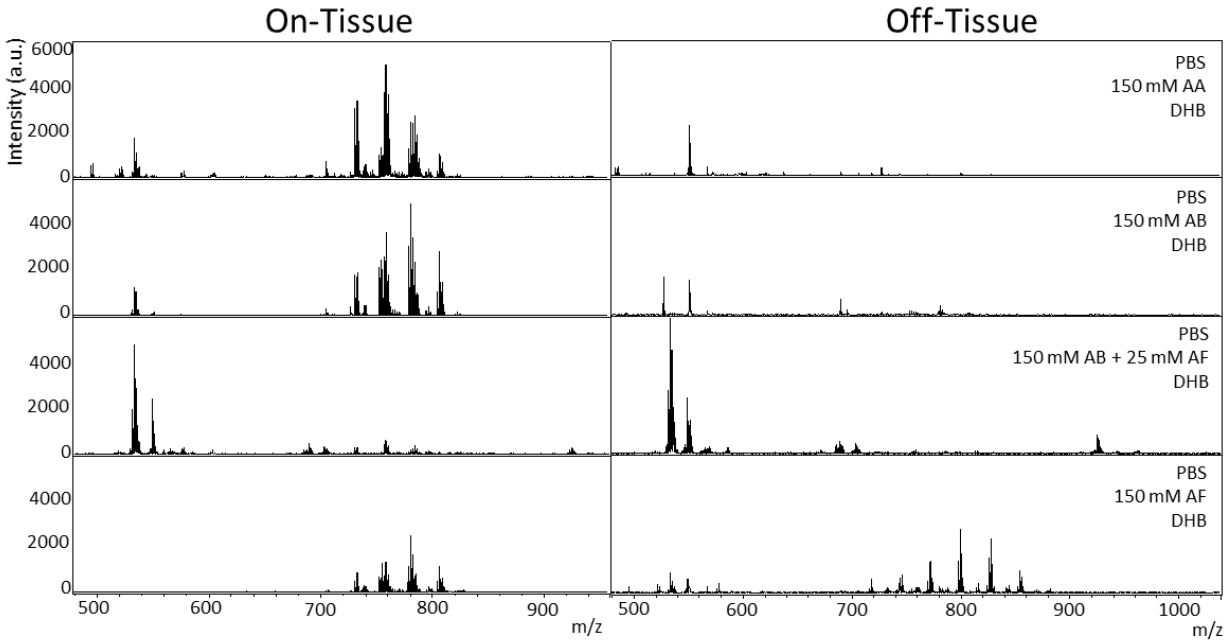

Supplemental Figure 2-3: Positive Ionization MALDI-TOF MS Lipid Profiles Acquired from Microdissected Malpighian Tubules in PBS and Washed in Different Ammonium-Based Salts. First row: drips of 150 mM ammonium acetate (AA). Second row: drips of 150 mM ammonium bicarbonate (AB). Third row: drips of 150 mM ammonium bicarbonate (AB), followed by drips of 25 mM ammonium formate (AF). Last row: drips of 150 mM ammonium formate. DHB matrix was used for all samples. Comparing the profiles after the various washes, it is clear that AB and AA buffers produce superior results to AF. Note, all of these approaches were harsh to the samples, causing the tubules to distort and change colour. The addition of 40% glycerol to the sample before sample wash (see Figure 2) helped to minimize this occurrence.

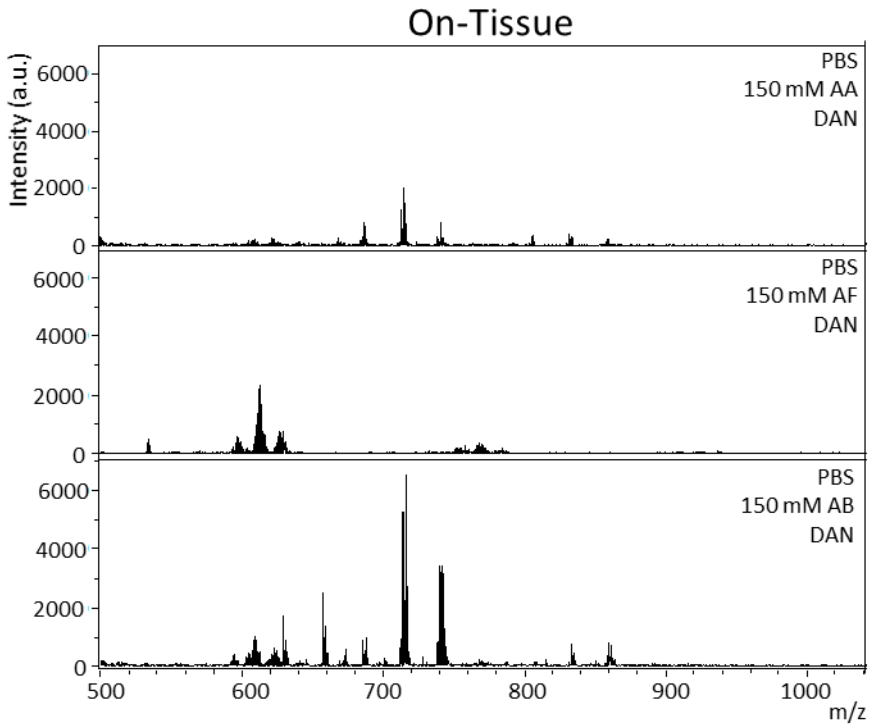

Supplemental Figure 2-4: Negative Ionization MALDI-TOF MS Lipid Profiles Acquired from Microdissected Malpighian Tubules in PBS and Washed in Different Ammonium-Based Salts. First row: 150 mM ammonium acetate (AA) wash; second row: 150 mM ammonium formate (AF); third row: 150 mM ammonium bicarbonate (AB). The DAN matrix was used for the three experiments. 150 mM AB on-tissue washes provided the greatest overall number of species and intensity, with 150 mM AA showing a similar spectrum at a lower overall intensity, and 150 mM AF instead losing most of the signals. Because very little off-tissue signals were observed with the PBS microdissection buffer compared to Supplemental Figure 2, no off-tissue results are shown.

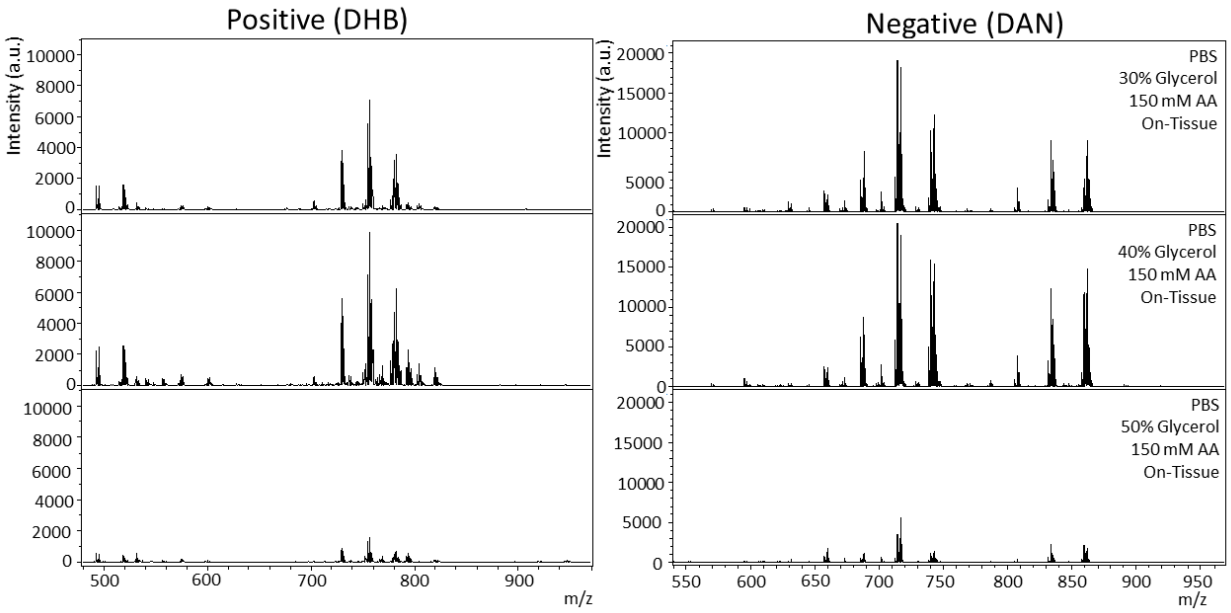

Supplemental Figure 2-5: Positive and Negative Ionization MALDI-TOF MS Lipid Profiles from Microdissected Tubules in PBS and Washed Using Different % Glycerol Solutions. After the glycerol wash, all samples were further washed with 150 mM ammonium acetate (AA). Matrix (DHB or DAN) was then deposited by sublimation. Results in the positive ion mode showed comparable results for both 30% and 40% glycerol, albeit overall greater intensity with the 40% glycerol wash. At 50% glycerol, more washes were needed for complete removal of excess glycerol, leading to a reduction in overall number of detected MS signals and signal quality. The same trends were observed in the negative ion mode.

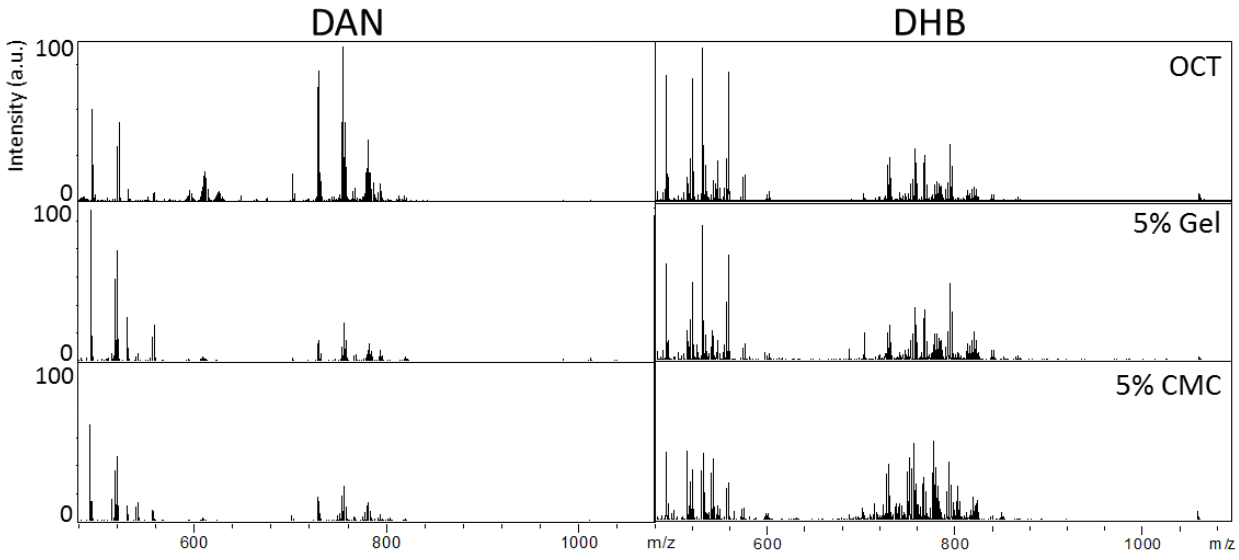

Supplemental Figure 2-6: Mean Positive Ionization MALDI-TOF IMS Spectra of Lipids Acquired from Fly Tissue Sections Obtained after Embedding and Sectioning in Different Media. The left column are the results from the DAN matrix, the right column those from the DHB matrix. The embedding media tested are shown by row: OCT, 5% gelatin in water (w/v) and 5% carboxymethylcellulose (CMC) in water (w/v). MS signal intensity is normalized across experiments. DAN results showed the greatest overall signal intensity in the phospholipid range from flies embedded in OCT. DHB results showed, a richer peak profile, particularly from flies embedded in 5% CMC. However, only OCT provided quality, reproducible sections at 10-12 µm thickness. Nonetheless, DAN was preferred over DHB because of the lower laser energy requirements allowing IMS at much higher spatial resolution (<15 µm without oversampling), as well as dual polarity IMS on the same section, as shown in **Figure 2-5**.

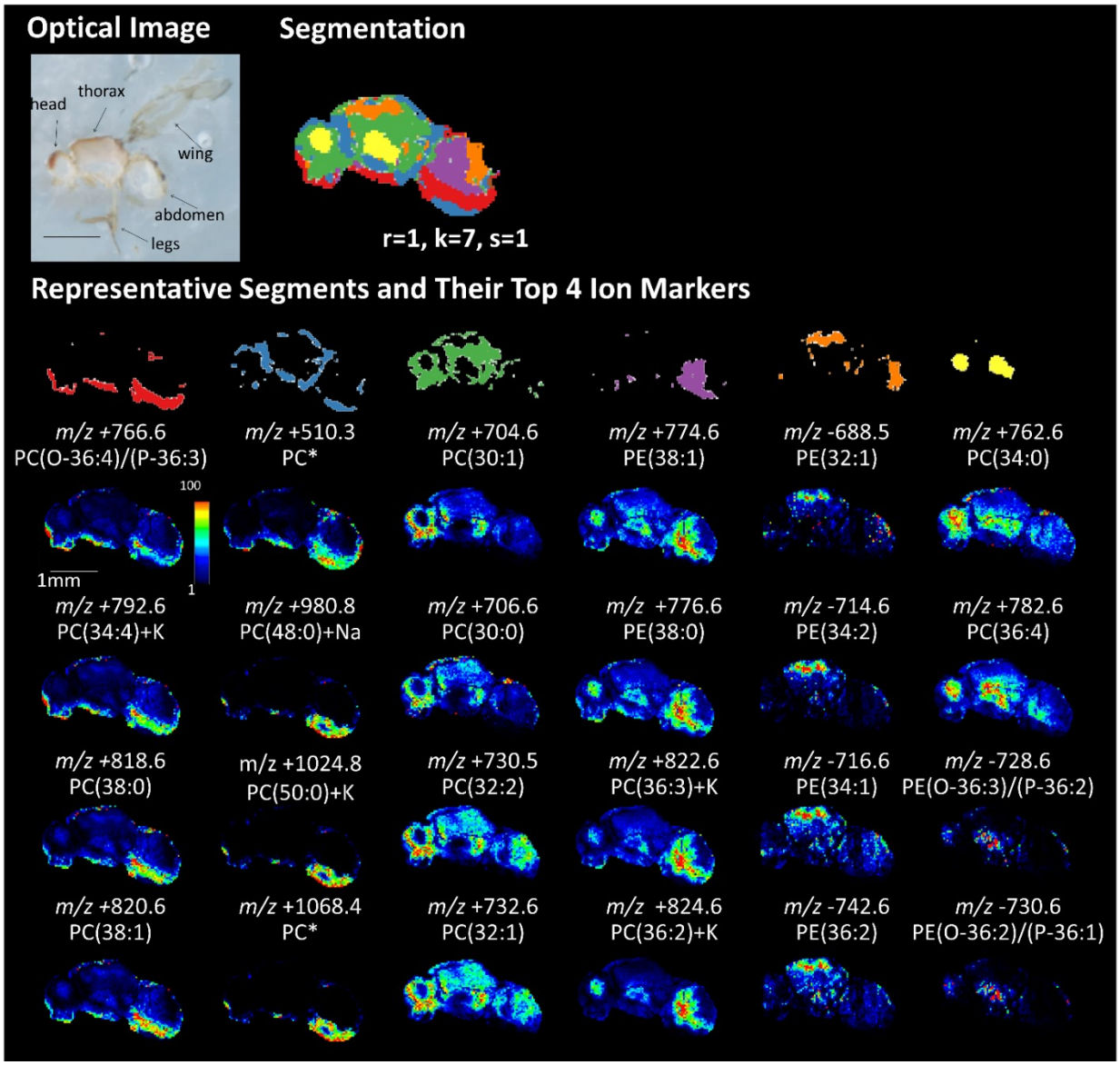

Supplemental Figure 2-7: Segmentation Analysis of the Dual Polarity IMS Results after Legs and Wings Removal. Positive and negative ionization data was acquired using a MALDI-TOF system on the same fly section at 25 µm spatial resolution with a 12 µm offset in the x and y array grid. The segmentation analysis was performed on the combined dataset as described in Patterson *et al*. 2018. The optical image is shown in the top left, followed by the segments, with the segmentation parameters listed. The segments and top four ion markers are shown below. Putative assignments based on exact mass and MS/MS are indicated by name. Those with incomplete

assignments are marked by *. Unless otherwise noted, all positive ion species are [M+H]+ and negative ion species [M-H]-. Of the seven segments, only the six shown represent IMS signals colocalized to different regions of the fly. The last segment was related to noise. Segmentation tests with r=6 was insufficient for separating the different regions while still creating a noise segment. Scale bar indicates 1 mm.

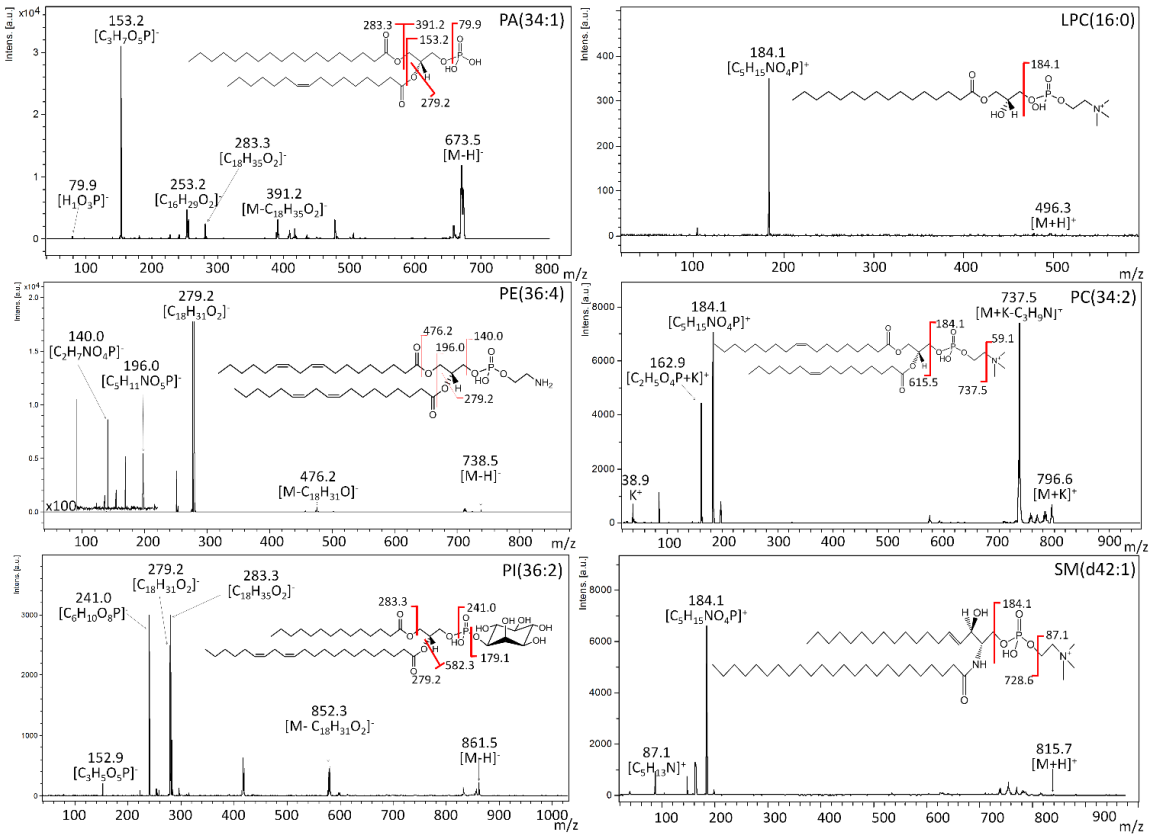

Supplemental Figure 2-8: MALDI MS/MS Fragmentation Pattern of PA, PE, PI, LPC, PC and SM Species. Representative MS/MS results and diagnostic ion fragments of five phospholipid families detected in the microdissected tubules and fly whole-body sections are shown in the six panels: PA(34:1), PE(36:4) and PI(36:2) in the first column and LPC(16:0), PC(34:2) and SM(d42:1) in the second column. Proposed fragmentation pathways are shown via their respective molecular drawings. MS/MS of PA, PE and PI were acquired in negative mode, while LPC, PC and SM were acquired in positive mode. In all cases, the exact location of the double bonds on the fatty acid chains could not be confirmed by MSMS and in the case of PC(34:2), the length of the fatty chains as well. The exact location and length shown in the drawings represent one of the many possibilities.

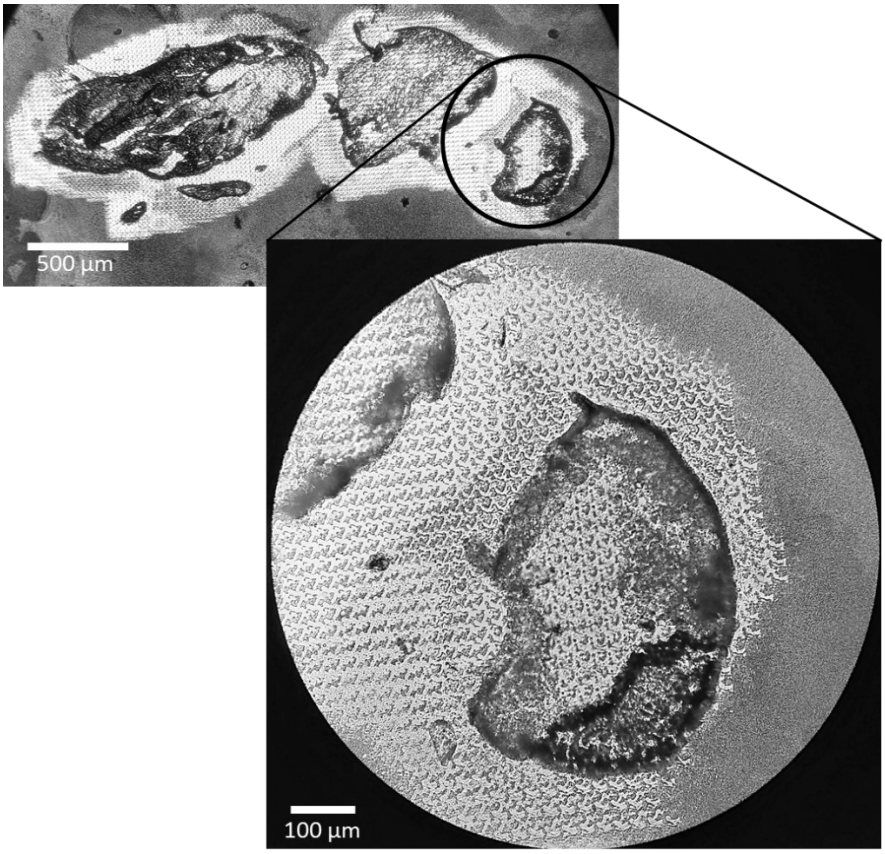

Supplemental Figure 2-9: Ablation Pattern Post Dual Polarity IMS at 25 µm. Optical images of a fly cross section after post dual polarity IMS at 25 µm indicating that while there is some overlap in the laser spots, the tissue is not completely ablated. This suggests that the 12 µm offset between the positive and negative ion mode grid arrays did not lead to major oversampling. The pattern is even more visible in the zoom of the head region. The images were taken through a Leica optical microscope at x5 for the whole-body section and x20 for the closeup of the head.

Chapter 3: Enhancing Ganglioside Species Detection for MALDI-TOF Imaging Mass Spectrometry in Negative Reflectron Mode

Ethan Yang, Martin Dufresne and Pierre Chaurand

International Journal of Mass Spectrometry, Volume 437, Pages 3-9, March 2019

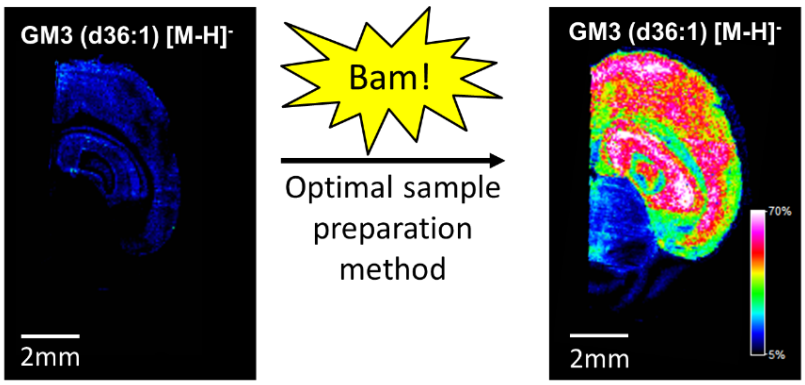

Author Contributions:

- Ethan Yang conducted all experiments, analyzed and interpreted the results and wrote the entirety of the manuscript.
- Dr. Martin Dufresne, a former doctoral student in the laboratory, provided support throughout the method development as well as helped review the manuscript.
- Prof. Pierre Chaurand, doctoral supervisor, initiated the experiment and finalized the manuscript.

3.1. Abstract

Enhanced ganglioside species detection was achieved for matrix assisted laser desorption ionization time-of-flight imaging mass spectrometry (MALDI-TOF IMS) in negative reflectron mode using a novel sample preparation protocol that involves washing the tissue in ammonium salt solutions followed by spray depositing ammonium salts and waiting 24 hours after sublimation of 1,5-diaminonaphthalene (DAN) before data acquisition. Application of this novel method to normal adult mouse brains led to more than 10-fold increase in total ion intensity in the ganglioside mass range and an increase in the number of detected sialylated species from 3 to 15, with no apparent delocalization observed at 20 μm spatial resolution, making it a powerful technique with the potential to provide greater information about gangliosides in numerous biological contexts.

3.2. Introduction

Gangliosides are a family of glycosphingolipids (GSLs) characterized by the presence of one or more sialic acid residues attached to the galactose moiety of the oligosaccharide chain linked to a ceramide tail[181]. They are subcategorized based on the number of sialic residues, where monosialogangliosides (GMs) have one, disialogangliosides (GDs) have two, trisialogangliosides (GTs) have three, tetrasialogangliosides (GQs) have four, and pentasialogangliosides (GPs) have five sialic acid residues, respectively[181] (their general structures are shown in **Supplemental Figure 3-1**). Found in the plasma membrane of all vertebrate cells, they constitute a large portion of lipid rafts[182] and are determined to be highly abundant in the brain[266], particularly GM1, GD1 and GT1b[184]. With important roles in cell recognition and signaling[267], it is no surprise that their dysregulation and overaccumulation have been implicated in numerous lysosomal storage disorders including Tay Sachs[268], Hunter's[205, 269], and Gaucher's[270], neurodegenerative diseases including Alzheimer's[134, 271, 272], Parkinson's[185], and the Guillain-Barré syndrome[273], and cancer including neuroblastoma[274], melanoma[275], and even breast cancer stem cells[276].

Matrix-assisted laser/desorption ionization (MALDI) imaging mass spectrometry (IMS) is a powerful technique for visualizing the spatial distribution of biomolecules on tissue surfaces, and has been the method of choice for on-tissue imaging of gangliosides since 2008 when Chen *et al.* visualized them in a Tay-Sachs/Sandhoff disease mouse model using 2,5-dihydroxybenzoic acid as matrix[277]. Since, there has been growing interest in the IMS community to improve the detection of gangliosides through buffered washes[215], novel matrices and matrix solutions[186, 189-191, 278], on-tissue derivatization[279], gold nanoparticle labeling[280], and the coupling of different ionization techniques[197]. Recently, our laboratory has successfully applied 1,5-diaminonapthalene (DAN) for 5 μm high spatial resolution imaging of GM2 and GM3 deposits found in a Hunter's disease mouse

model[205]. However, the same cannot be said of healthy tissue sections, where ganglioside species are not overexpressed and aggregated, and pose a challenge for comparative studies for less abundant gangliosides (such as GD2) that are strongly correlated to many of the diseases mentioned above. While Colsh *et al.* has developed a spot deposition method of 2,6-dihydroxyacetophenone (DHA) mixed with ammonium sulfate, HBFA that allowed for the detection of four classes of gangliosides (GM, GD, GQ, GT) in a wild-type mouse brain and imaging up to 80 μm of spatial resolution [191, 281], this method is limited in resolution by wet-matrix application.

To this end, we have used healthy mouse brains to develop a MALDI sample preparation protocol with dry matrix application that significantly increases the overall ion intensity of gangliosides and other sialylated species while still allowing for high spatial resolution imaging down to 20 μm lateral resolution. This protocol combines a series of optimized parameters that synergistically contribute to more than 10-fold increase in signal intensity and 5-fold increase in the number of ganglioside species detected.

3.3. Experimental

3.3.1. Chemicals and Reagents

Unless otherwise noted, all solvent and material were purchased from Thermo Fisher Scientific (Ottawa, ON). 1,5-diaminoapthalene (DAN), 9-aminoacridine (9AA), 2,5-dihydroxybenzoic acid (DHB), 5-Chloro-2-mercaptobenzothiazole (CMBT), norharmane (nH) and ammonium formate (AF) were purchased from Sigma-Aldrich Canada (Oakville, ON). For mass calibration, a total ganglioside extract (brain, porcine-ammonium salt) was purchased from Avanti Polar Lipids, Inc. (Alabaster, AL).

3.3.2. Tissue Sampling and Sectioning

The mouse brains used in this experiment were obtained from twelve-week old mice (n = 5)

euthanized through CO_2 asphyxiation, as approved by the local Ethical Committee of the Université de Montréal. The brains were harvested and flash frozen by contact with dry ice immediately after sacrifice to minimize molecular deterioration and maintain tissue morphology. 14 µm thick horizontal mouse brain sections were obtained at a latitude where the hippocampus was clearly visible (3 to 6 mm inferior to Bregma) using a Leica CM3050 cryostat (Leica Microsystems GmbH, Wetzlar, Germany) and thaw-mounted on 25 x 75 mm indium-tin-oxide (ITO) microscope slides (Delta Technologies, Loveland, CO). The tissues were then dried in a desiccator for ≤ 1hr prior to further processing. For the 65 µm spatial resolution IMS experiments, serial sections were collected and stained with hematoxylin and eosin (H&E) using a standard protocol (see Supplemental Table 3-1), while for the 20 µm spatial resolution IMS experiments the same section was stained after matrix removal by immersion for 30 seconds in successive ethanol solutions (90% and 70%).

3.3.3. Optimizing the Ammonium Formate (AF) Washing Protocol

Based on the protocol established by Angel *et al.* for overall enhancement of lipid signals in the negative ion mode[215], ganglioside signals were compared across five wash times (0, 30, 45, 60 and, 90s) with AF at five different concentrations (0, 25, 50, 75 and 100 mM). For solutions with AF, the pH ranged from 6.3 to 6 (lowest to highest concentration). The signal intensities after the washing protocol were also compared with and without the optimal wait time prior to data acquisition (see below).

3.3.4. Investigating ammonium formate (AF) deposition by the TM-Sprayer

Inspired by the AF wash, additional AF deposition using a first-generation TM-Sprayer instrument (HTX Technologies, Chapel Hill, NC) was also investigated. An optimal deposition layer was found using a solution of 400 mM AF (4:6 H_2O:ACN). The AF spray deposition cycle takes 15 minutes. The specific instrument parameters can be found in the Supplemental Table 3-2.

The layer density was evaluated by weighing an ITO glass slide three times with the tissue section before and after salt deposition under the same instrumental parameters. The weight difference divided by the area of the glass slide provided the density. The effects of wait time and AF wash in concert to AF deposition was also studied.

3.3.5. Matrix Deposition by Sublimation

Within 15 minutes after tissue sample processing with AF, DAN was deposited onto the sample using a sublimation apparatus (Chemglass Life Science, Vineland, NJ) as previously described[60]. No significant weight difference between the end of AF spray deposition and the beginning of the sublimation process was observed indicating no noticeable AF evaporation within this 15 minute timeframe. The optimized matrix thickness that provided reproducible ganglioside signals with maximum signal-to-noise ratio (S/N) was approximately 250 $\mu g/cm^2$, equivalent to 6 minutes of deposition at 180°C and 0.5 mbar. The matrix density upon sublimation was evaluated by the same approach as the salt layer. Lastly, matrix sublimations should be performed under a fume hood due to the possible carcinogenic effects of the DAN matrix.

3.3.6. Determining the Optimal Wait Time Before Data Acquisition

Protocols in the literature for MALDI IMS of ganglioside species suggest including a 24h wait time after matrix deposition for enhanced ganglioside signal detection, though no explanation has been given[278, 282]. For verification, the ganglioside signal intensity was compared when acquired immediately after matrix deposition (0h), after matrix deposition and 24h wait time at -20°C (24h), and after matrix deposition and 48h wait time at -20°C (48h).

3.3.7. MALDI-TOF Mass Spectrometry

Profiling and IMS of the tissue sections were performed on a MALDI TOF/TOF ultrafleXtreme mass spectrometer equipped with a SmartBeam II Nd:Yag/355 nm laser operating

at 1 kHz, providing a laser focus down to 20 μm in diameter for the "minimum" focus setting (Bruker Daltonics, Billerica, MA). MS and IMS data acquisition were performed in negative ion mode using the reflectron geometry with flexControl 3.4 and flexImaging 4.0, respectively (Bruker Daltonics, Billerica, MA). Acceleration voltage was set to −20 kV and all other instrumental parameters (delayed extraction parameters, source voltages, detector gain, laser energy, etc.) were optimized for maximum S/N of the detected ganglioside signals. Unless stated otherwise, the same parameters were used throughout the entire study. For protocol optimization, profiling MS data was acquired in 1000-3000 *m/z* range from three group replicates of five accumulations of 100 shots in random areas of the hippocampal region where a greater number of ganglioside species have been detected[281, 283]. For IMS data acquisition, 300 shots were summed per array position in the same mass range. Regular IMS measurements were acquired at a lateral resolution of 65 μm, while higher spatial IMS data were acquired with at a lateral resolution of 20 μm. IMS data were visualized using flexImaging 4.0 without any signal normalization. External calibration was carried out in cubic enhanced mode using a total ganglioside extract to obtain five points of calibration over the considered mass range. A mass accuracy better than 30 ppm was obtained for MS and IMS measurements on tissue. Ganglioside identification was performed by comparing accurate mass measurements with the LIPID MAPS prediction tool (http://www.lipidmaps.org/tools/index.html) and in some cases confirmed by MS/MS using the LIFT-TOF/TOF instrument mode.

3.3.8. Data Analysis

Total ion currents (TIC) were calculated using an in-house code based on the MALDIquant package (x1.15) in the R environment (x3.2.5). Only peaks with a minimum S/N of 3 after smoothing and baseline reduction were incorporated into the TIC. To determine the optimized

experimental parameters, the mean TIC was calculated using five technical replicates of three mouse brains subjected to the same experimental condition and compared across the different sample preparation approaches. Fold change was also calculated based on the control condition for each parameter. The error bars in the figures represent one standard deviation, and statistical significance was calculated using the Student's t-test.

3.4. Results & Discussion

3.4.1. Choice of Matrix and its Method of Deposition

Sublimation was chosen as the matrix application approach because this dry deposition method minimizes delocalization and allows for high resolution IMS down to 10 μm and below [60, 205]. Previous literature has shown sublimated DAN to be the matrix of choice for the detection of gangliosides[205, 278, 282]. Comparison of the sublimation results of three possible matrix candidates for negative mode IMS (9AA, DHB, DAN) tested on mouse brain sections corroborated with this finding. Two other possible matrices (CMBT and nH) were also tested through profiling[189, 284]. While the signals obtained were comparable to that of DAN, the high cost of these made it unpractical for sublimation, which in our sublimation system requires a minimum of 300 mg[109]. Representative spectra for the sublimation and profiling results can be found in Supplemental Figure 3-2. Taking all information into consideration, DAN was selected as the matrix for the entire study.

3.4.2. On-Tissue Optimization & Characterization

An important aspect of method development is to increase both the sensitivity and specificity for the class of molecules under investigation, raising the signal for low-abundant species above the noise threshold. Typically, only three or four of the most abundant ganglioside species from the mouse brain are detectable by MALDI-TOF MS in the control protocol—that is, no washing,

no AF deposition, no wait-time before data acquisition (**Figure 3-1**). Subjecting the sample to 24h in the -20°C, the optimal wait condition based on time course tests, approximately triples the overall sensitivity with no observable increase in the number of species detected (**Figure 3-1** and **Figure 3-2a**). In other words, the same number of ganglioside species detected have improved S/N. It is unclear what causes this change, though extraction of these species into the matrix over time

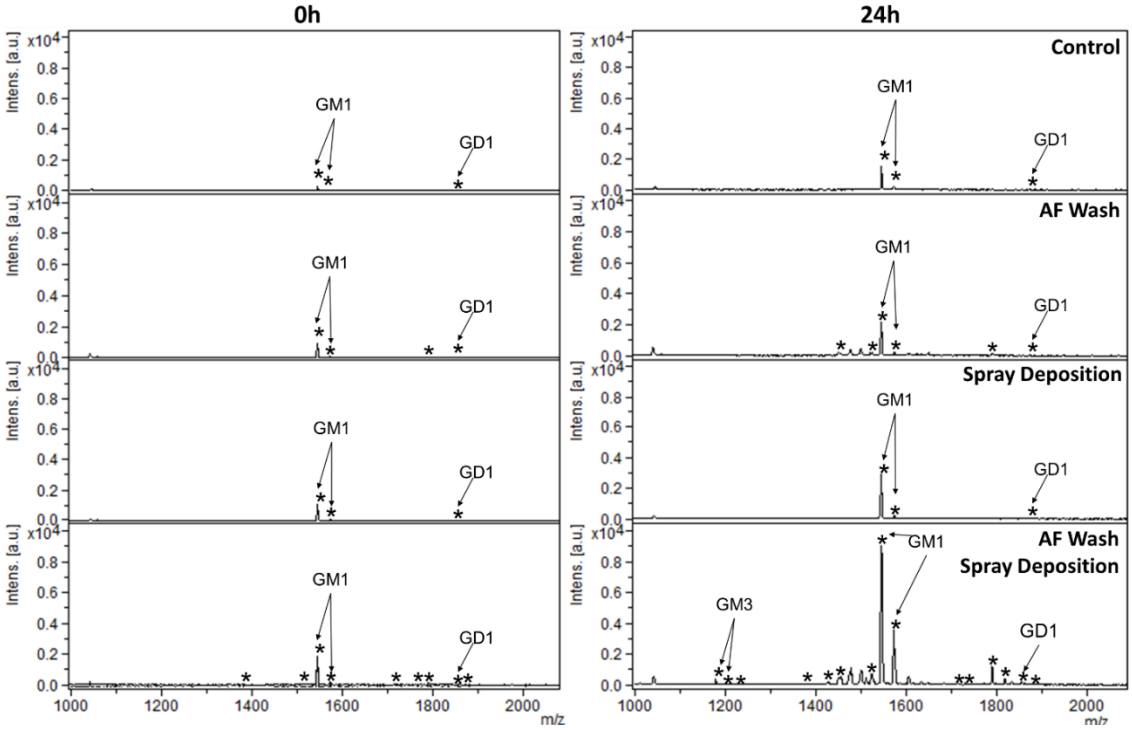

Figure 3-1: Typical Negative Mode MALDI MS Spectra (Scaled to the Same Intensity) from Brain Tissue Sections Subjected to the Control, Optimal Ammonium Formate (AF) Wash, Optimal AF Spray Deposition, and Optimal AF Wash Followed by Optimal AF Spray Deposition. Left column indicates no wait-time (0h), while the right column indicates optimal wait-time condition (24h) prior to MS data acquisition. In all cases, waiting 24 h improved the overall signal intensity, and in some cases, the number of signals detected. The number of sialylated species based on MS/MS determination (marked with *) increased from 3 to 15 when the optimal sample preparation method (bottom right spectra) was applied. Those with full MS/MS on-tissue confirmation have been labelled according to their conventional names.

may explain this observation, a phenomenon also observed for lipids by matrix-enhanced SIMS after DHB matrix deposition by sublimation[285]. This hypothesis is supported by literature[60] reporting that a thicker matrix layer is required for optimal ganglioside signals compared to phospholipid signals. The slight improvement when leaving the sample for 48 hours compared to 24 hours was not statistically significant (**Figure 3-2a**), indicating little to no degradation of ganglioside species over time, in line with the results for phospholipid signals when left in the -80°C environment[265]. Despite the small fold increase, wait time has shown to contribute to dramatic improvements in signal quality and intensity when combined with the other optimized parameters.

Optimal concentration for AF wash was found at 75 mM (optimization curves for all concentrations tested can be found in Supplemental Figure 3-3), and provided less than a 2-fold improvement in signal intensity (**Figure 3-2b**), with four and sometimes five ganglioside species detected. This result is in stark contrast to the 5-fold improvement reported by Angel *et al*.[215] for lipid signals using DHB as the matrix. However, with the addition of the 24-hour wait time, the overall signal improvement was found to be nearly 4-fold, with no change in the number of ganglioside species detected. While washing at the optimal concentration for 30 or 45 seconds followed by a 24-hour wait time provided similar signal improvement, longer wash times run a greater risk of delocalization and tissue tear (though tissue tearing was only observed when washing was accomplished with MilliQ water alone). Hence, the 30 second wash time was preferred and chosen as the optimal wash condition.

Deposition of an optimal thickness of AF at 30 $\mu g/cm^2$ yielded approximately 3-fold overall signal increase (**Figure 3-2c**) and no change in the number of species detected. The fold change hovers around 3-fold with increasing AF deposition; however, because this salt is hydroscopic, increased deposition >30 $\mu g/cm^2$ promotes incomplete drying between passes and may lead to

water retention on the tissue and the formation of large millimeter crystals in lieu of micrometer crystals, preventing successful IMS experiments. In fact, one critical aspect of spray deposition is ensuring the complete drying of the tissue section between each pass. Visually, the optimal amount of AF deposition renders the entire tissue section slightly more opaque and white upon matrix

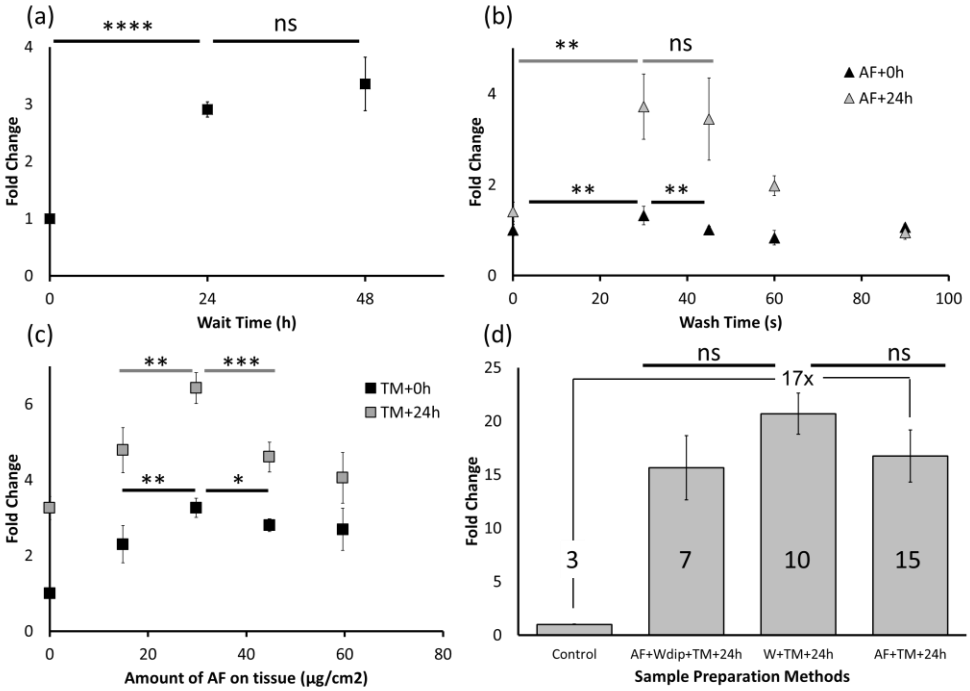

Figure 3-2: Effects of Wait Time, AF Wash and AF Spray on Ganglioside Signal. (a) Wait-time comparison post matrix sublimation. Example spectra are shown in the first row of Figure 1. (b) Wash time optimization using 75 mM ammonium formate (AF), without wait time (AF+0h) and with wait time (AF+24h). (c) On-tissue AF deposition optimization, without wait time (TM+0h) and with wait time (TM+24h). (d) Fold change in TIC for the control method, and the three most prominent sample preparation methods (AF+Wdip+TM+24h, W+TM+24h and AF+TM+24h) that demonstrated an average 17-fold increase in signal intensity and up to 15 sialylated species detected (number in or above each bar). Error bars represent the standard deviation of triplicate measurements. ns = not significant, * = p value ≤ 0.05, ** = p value ≤ 0.01, *** = p value ≤ 0.001, **** = p ≤ 0.0001

sublimation than the control sample, whereas microscopic AF crystals are observed around the tissue (Supplemental Figure 3-4). This suggests that AF is homogeneously deposited on the tissue surface and is (partially) absorbed by the tissue, preventing large crystal formation. As with the AF wash, leaving the sample in the freezer for 24 hours improves signal intensity to a total of 6-fold in comparison to no AF deposition and immediate data acquisition, further corroborating the importance of wait time for detecting this class of species.

With hints that a combinatory approach increases signal intensity, the three optimized parameters (wait time, AF wash condition, AF deposition) were applied to tissue sections to determine the protocol that would lead to the greatest overall improvement. Unsurprisingly, the three most prominent ones all require an initial washing step, the optimal AF deposition (TM), DAN deposition by sublimation, and the optimal wait time (24h), as shown in Supplemental Figure 3-5). For the initial washing step, the optimal washing conditions (AF) alone, the optimal washing condition followed by 5 dips in MilliQ water (AF+Wdip) or washing for 30 seconds in MilliQ water (W) provided statistically similar TICs that were all more than 10-fold greater than for the control protocol (**Figure 3-2d**). Yet, the number of detectable sialylated species varied. As can be seen in Supplemental Figure 3-5, the "AF+Wdip+TM+24h" approach resulted in fewer than 7 ganglioside species detected, whereas both the "W+TM+24h" and the "AF+TM+24h" approach allowed for more than double that amount, with 15 species detected using the "AF+TM+24h" approach. However, the "W+TM+24h" approach tore mounted tissue sections about 2/3 of the time, making it unsuitable for imaging experiments. In conclusion, the optimal washing condition coupled to optimal AF deposition and the optimal wait time (AF+TM+24h) produced the highest increase in detection and most reproducible signal for gangliosides. For the rest of the study, this protocol will simply be referred to as the "optimal method".

3.4.3. On-Tissue Signal Identification

Of the ganglioside species detected and identified, GM1 (d36:1) and GM1 (d38:1) are the two most intense species. GM1 has been reported to be the most abundant ganglioside species in the brain, as confirmed by the spectrum obtained from the total ganglioside extract standard (see Supplemental Figure 3-6)[278, 286]. The MS/MS spectra of GM1 (d36:1) shown in **Figure 3-3** display the expected fragment ion patternss. Although many fragmentation pathways are possible, MALDI-TOF MS/MS favors the loss of the labile sialic acid residue, followed by the sequential loss of the sugar moieties. In fact, the initial loss of the sialic acid fragment $C_{1\beta}$ is observed at *m/z*

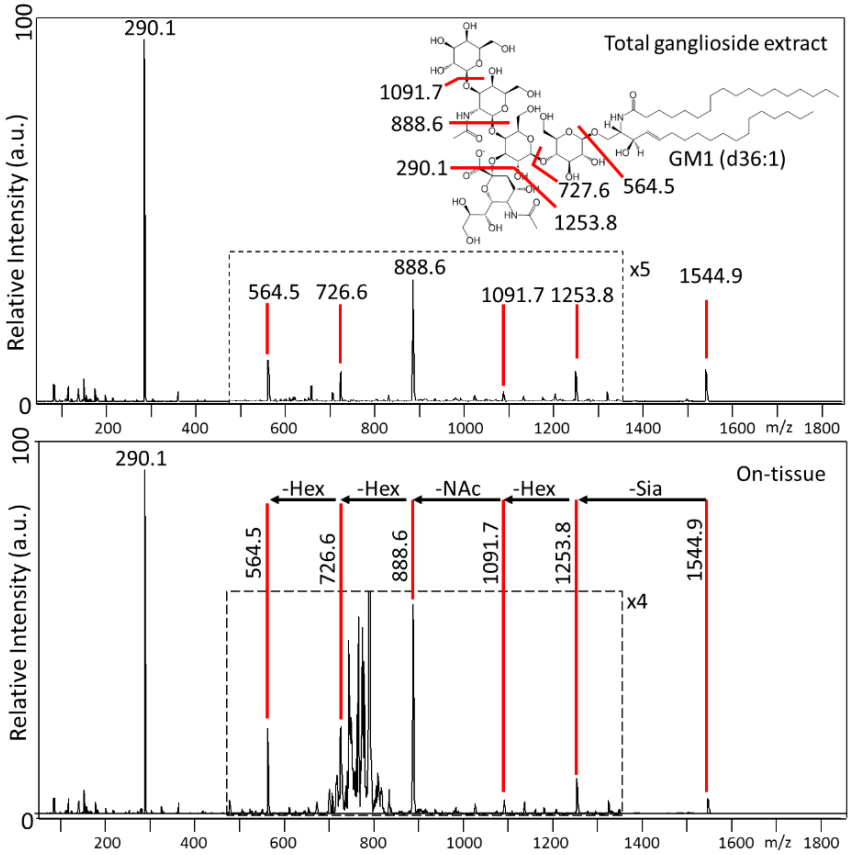

Figure 3-3: MALDI-TOF MS/MS spectra of GM1 (d36:1) directly acquired from the total ganglioside extract (top) and a mouse brain section (bottom) displaying all five diagnostic fragment ions: Sia→Hex→NAc→Hex→Hex. Sia = sialic acid, Hex = hexose (glucose or galactose), NAc =N-Acetylgalactosamine. See text for more details.

290.1, leading to the first stable fragment 1253.8 ($[M_1\text{-}H]^-$), followed by hexose loss yielding fragment 1091.7 (Y_3), NAc loss producing fragment 888.6 (Y_2), subsequent hexose loss producing fragment 727.6 (Y_1), and finally another hexose loss leading to 564.5 (Y_0). The naming convention is based on Domon and Costello[287]. It is important to note that no structural information on the fatty acid side chain or the sphingosine chain was obtained during the MS/MS experiments. Furthermore, because of the wide window needed in LIFT-TOF/TOF to ensure high signal intensity, some contaminate signals from tissue also entered the LIFT and their fragments between *m/z* 600-800 were also detected. The allocation of the two extra $–CH_2$ found for GM1 (d38:1) was made through the results of the exact mass search in the Lipid Maps database and its fragmentation behavior (Supplemental Figure 3-7). Other species referred to by name in this paper have also been characterized with the same fragmentation behavior, and are also shown in Supplemental Figure 3-7.

3.4.4. IMS of a Horizontal Mouse Brain Section

Serial sections of horizontal mouse brain analyzed by IMS at 65 μm of spatial resolution indicated significant signal improvement with the optimal method (**Figure 3-4**). Ion images of unidentified sialylated species can be found in Supplemental Figure 3-8. GM1 (d36:1) displayed the greatest intensity increase, followed by GM1 (d38:1), corroborating with the profiling data. While both species are highly abundant in the hippocampal and cortex region, there are visible differences in their localization and relative intensities. This observation has been well-characterized in the literature [278, 281]. The identified gangliosides are all highly abundant in the hippocampus and the cerebral cortex, with some in the midbrain and the cerebellum. The optimal method favors desorption of gangliosides as $[M\text{-}H]^-$ species, as evidenced by the shift from the

detection of GD1 (d36:1) as a $[M+Na-2H]^-$ with the control method to $[M-H]^-$ with the optimal method applied. This evidence suggests that the AF washing step serves to remove excess salt from the sample. This also supports the efficacy of a pure water wash, though an unbuffered wash could lead to changes in histology and have been observed to lead to undesirable tissue tear.

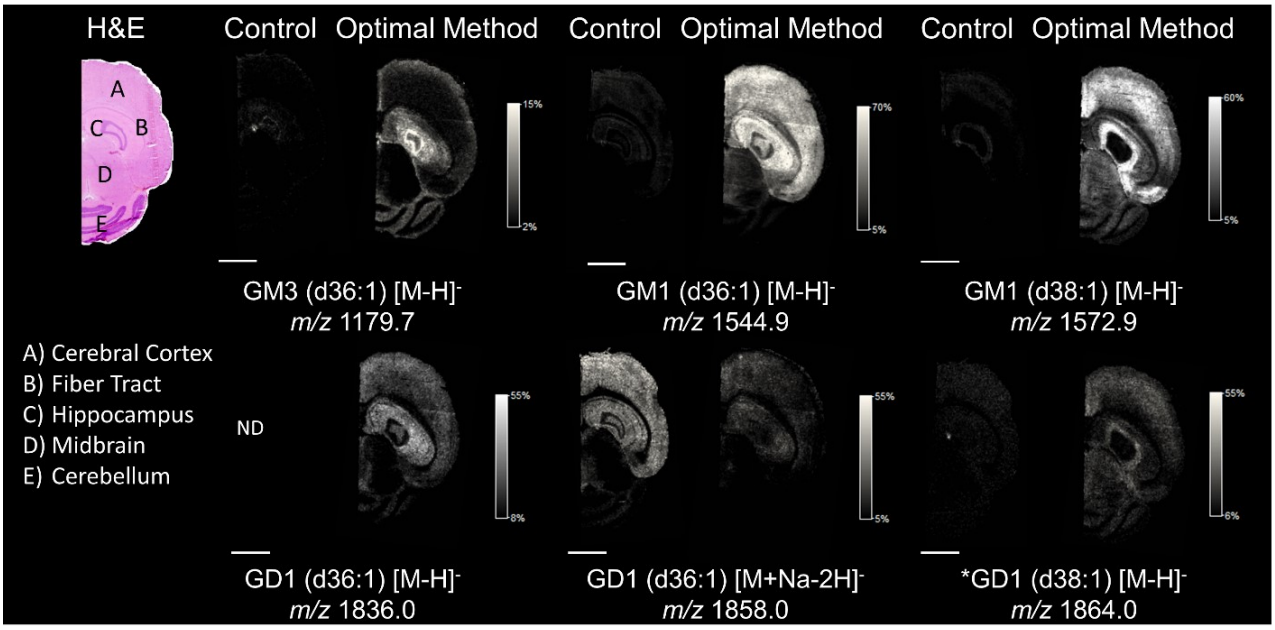

Figure 3-4: MALDI-TOF IMS of serial horizontal mouse brain tissue sections subjected to the control (sublimation only, no wait time) and optimal (optimal AF wash followed by optimal AF deposition, matrix sublimation and a 24 hour wait time before data acquisition) preparation method, respectively. The results were acquired in one IMS experiment at a lateral resolution of 65 µm. Supplemental Figure 3-8 shows other sialylated species that were also detected. GM1 species displayed the largest signal intensity variations with respect to the optimal method. Only modest improvements where observed for GM3. For GD1, only the [M+Na+2H]- species is detected in the control method, whereas the optimal method allowed for the detection of the [M-H]- ion species, most likely favored by salt removal after the initial washing step in AF. Except for GD1 (d38:1) that had partial confirmation via the presence of two sialic acids in its MS/MS spectrum, the

identity of all ganglioside species presented have been confirmed by MS/MS. The scale bar represents 2 mm. ND: not detected.

One limiting factor for the optimal method is potential signal delocalization, which may occur during the AF washing and spray deposition steps because of the wet interface involved. Regardless, no delocalization was visually observed at 65 µm when overlaying IMS results and histology. This was further confirmed by higher spatial resolution IMS data acquired with 20 µm lateral steps in the hippocampal region after control and optimal method processing. This spatial resolution was chosen because it was the smallest pixel size for which ganglioside signals could still be reliably detected from the control sample. The hippocampal region was chosen because of the greater abundance and clear correlation of many ganglioside species to histological structures[283]. Results are presented in **Figure 3-5.** Firstly, the H&E section staining overlaid with the GD1 (d36:1) ion distribution showed no presence of the GD1 species in the pyramidal layer of the hippocampus in both methods. Second, the overlay of the two GM1 species demonstrated the same spatial distribution for both methods, though the intensity for GM1 (d36:1) increased more significantly when compared to GM1 (d38:1), rendering the composite image greener. Since the section for the optimal method is deeper into the tissue, the fiber tracts are thinner and less visible, not because of delocalized GM1 species.

Although the high resolution IMS data were acquired at 20 µm of spatial resolution, after applying the optimal method, laser fluency (taking into account the Global and Method instrument attenuation settings) could be lowered by at least 8% while maintaining constant signal output without reducing the overall quality of the spectra (Supplemental Figure 3-9). Because the ablation area decreases with decreasing laser energy, in this case, IMS can be achieved at 15 µm spatial resolution without oversampling, as confirmed by measuring the laser spot size at the lower laser

energy. In practice, when applying the optimal method and a lower laser fluency, 5 µm spatial resolution IMS in the oversampling mode should be attainable for samples with (localized) ganglioside overexpression[205].

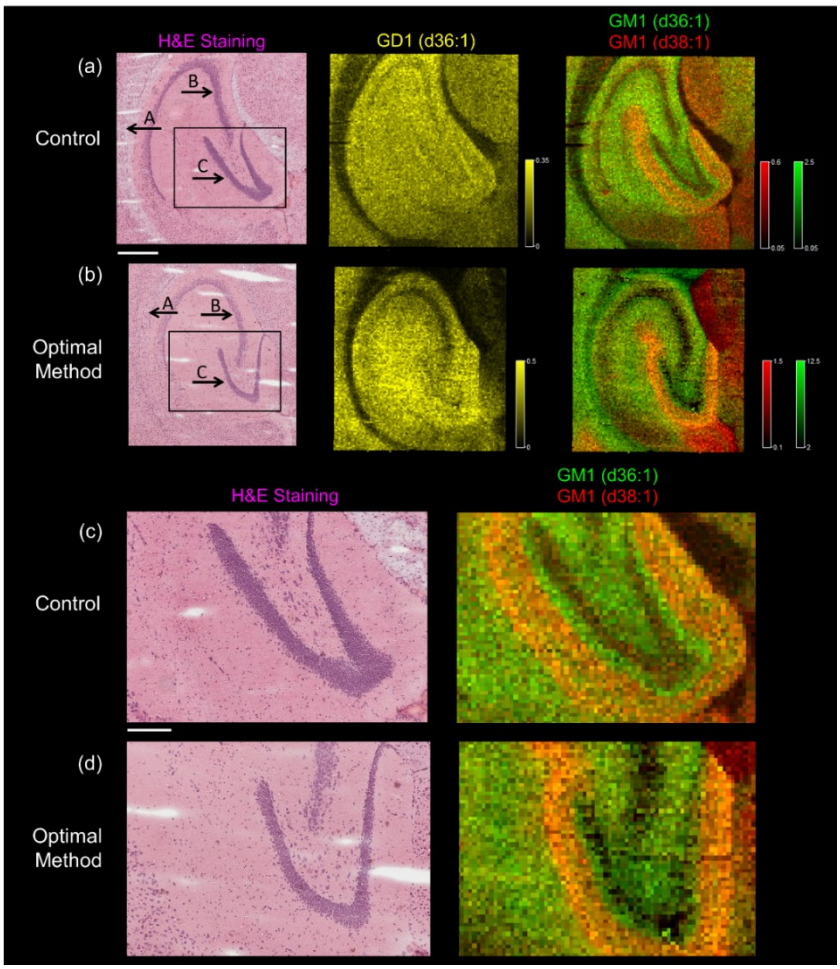

Figure 3-5: MALDI-TOF IMS of mouse horizontal brain tissue sections (near serial sections from the same brain) in the hippocampus region acquired at 20 µm of lateral resolution comparing the (a) & (c) control (sublimation only, no wait time) to the (b) & (d) optimal (optimal AF wash followed by optimal AF deposition, matrix sublimation and a 24 hour wait time before data acquisition) preparation protocol. (a) & (b) rows: H&E section staining after data acquisition and matrix removal (Left panel). A = fiber tract, B = pyramidal layer of Ammon's horn in the hippocampus, C = granule cell layer of the dentate gyrus. Ion distribution of GD1 (d36:1) (middle

panel). Overlay of GM1 (d36:1) and GM1 (d38:1) ion distributions (right panel). Scale bar represents 500 μm. (c) & (d) rows: zoomed areas from (a) & (b) showing no apparent GM delocalization after section processing with the optimal protocol. Scale bar represents 200 μm.

3.5. Conclusions

This study outlines a sample preparation method that allows for down to 20 μm spatial resolution MALDI-TOF IMS data acquisition of gangliosides from thin tissue sections through increasing their overall signal intensity by more than 10-fold compared to approaches found in current literature. This method calls for a 30 second section wash in a 75 mM AF solution, a deposition of 30 μg/cm^2 of AF onto the sample, a deposition of 250 μg/cm^2 of DAN matrix by sublimation, and 24h of wait time in -20°C environment prior to IMS. This increased sensitivity allowed MALDI-TOF IMS data to be collected on ganglioside species that were previously not detectable. Further, this approach did not lead to any noticeable delocalization, and has the potential for even higher resolution imaging for tissue samples presenting higher expressions of gangliosides. Previous studies have demonstrated that the instability of gangliosides when measured by reflectron MALDI-TOF MS is due to the metastable loss of the sialic acid residues during time of flight, a problem that can be minimized with higher pressure systems through collisional cooling[194]. This is the case for MALDI ion traps, QTOF and FT/ICR mass spectrometers, with which we expect a greater number of detectable species. As such, this protocol opens the possibility for the study of numerous biological systems and diseases where gangliosides are known or thought to be implicated.

3.6. Acknowledgements

The authors acknowledge funding from the Natural Sciences and Engineering Research

Council of Canada (NSERC), and the Canadian Foundation for Innovation (CFI). The authors would also like to thank Assia Lysius (Centre de Recherche du Centre Hospitalier de l'Université de Montréal, Quebec, Canada) for her aide with the high-resolution H&E scans.

3.7. Supplemental Information

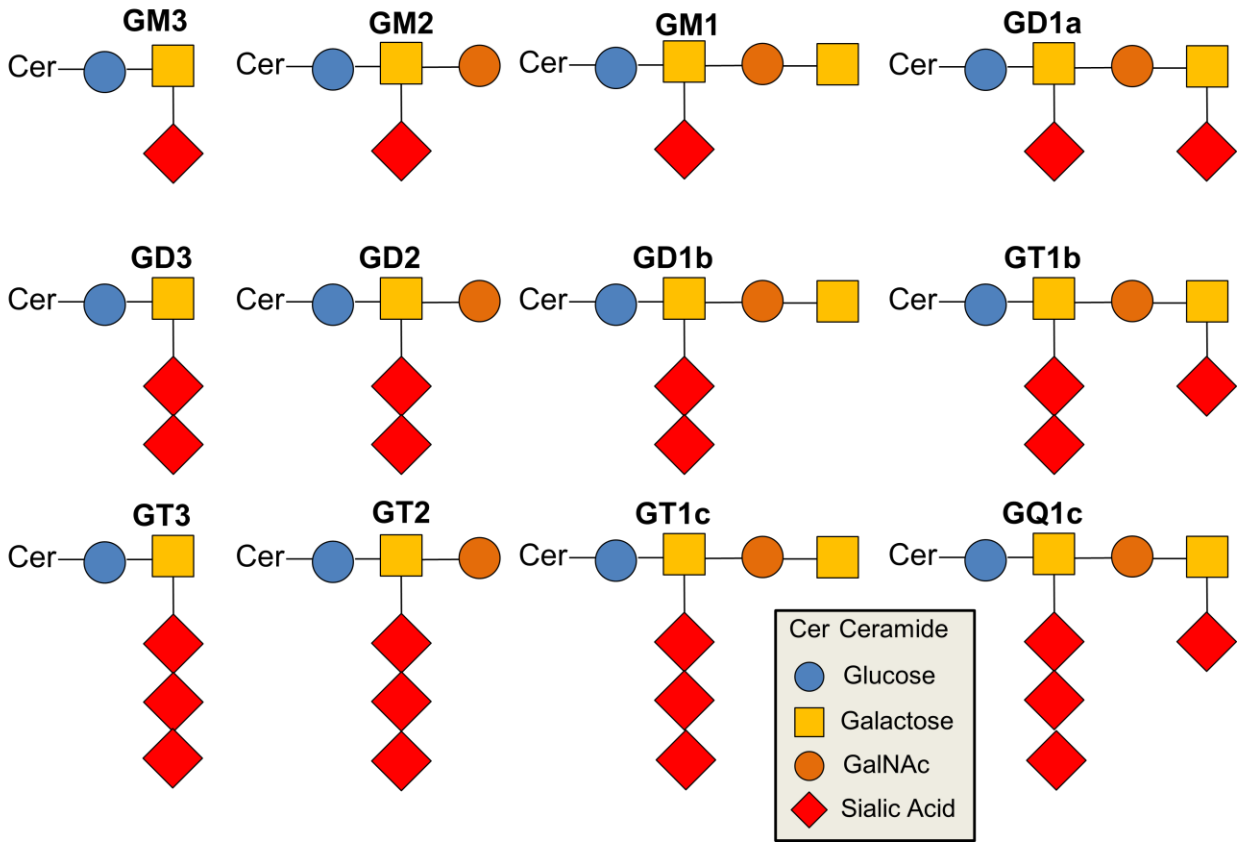

Supplemental Figure 3-1: Schematic Representation of the Ganglioside Lipid Family.

Supplemental Table 3-1: H&E Staining Protocol for Mouse Brain Section. H&E staining protocol adopted for mouse brain sections post-IMS data acquisition and serial sections.

Step	Solution (Immersion)	Time	Note
1	95% ethanol	30 seconds	Matrix is removed during this washing step.
2	70% ethanol	30 seconds	
3	De-ionized water	30 seconds	
4	Gill 3 Hematoxylin	25 seconds	Progressive stain; filter each time before use
5A	De-ionized water	10 seconds	
5B	0.007% Sodium Bicarbonate in H2O	5 dips	Bluing solution
6	70% ethanol	30 seconds	
7	95% ethanol	30 seconds	
8	Eosin	5 dips	
9	95% ethanol	30 seconds	
10	100% ethanol	30 seconds	

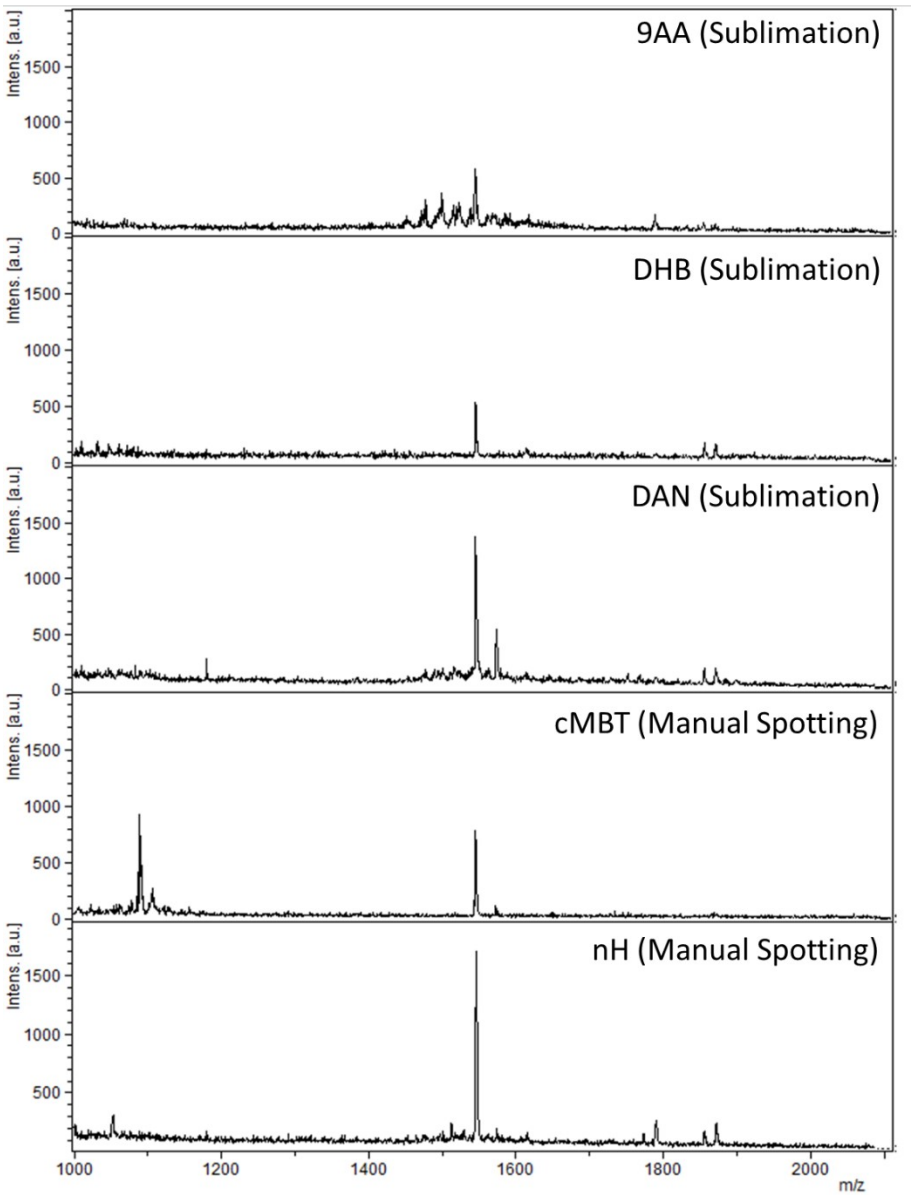

Supplemental Figure 3-2: Typical Negative Reflectron Mode MALDI-TOF MS Spectra of the Brain Hippocampal Region with different matrices applied either by sublimation or manual spotting. In sublimation, DAN provided the greatest overall signal intensity. Norharmane (nH) showed comparable results to sublimated DAN, but was found too costly for sublimation.

Supplemental Table 3-2: TM Sprayer AF Deposition Parameters. The gas pressure was set at 150 kPa. Deposition cycle takes 15 mins.

Parameter	**Condition**
Software version	1.0.0.8
Flow Rate	133 µL/min (8 ml/hr)
Spray Nozzle Velocity	3485 mm/min
Spray Nozzle Temperature	55.0°C
Number of passes	30 passes
Time per path	12 seconds
Drying time between passes	6 seconds
Spray Area	x = 0, 90 mm & y = 0, 55 mm
Track spacing	7.0 mm
Offset spacing	0 mm (odd passes), 3.5 mm (even passes)
90° rotation each alternating pass	Not used

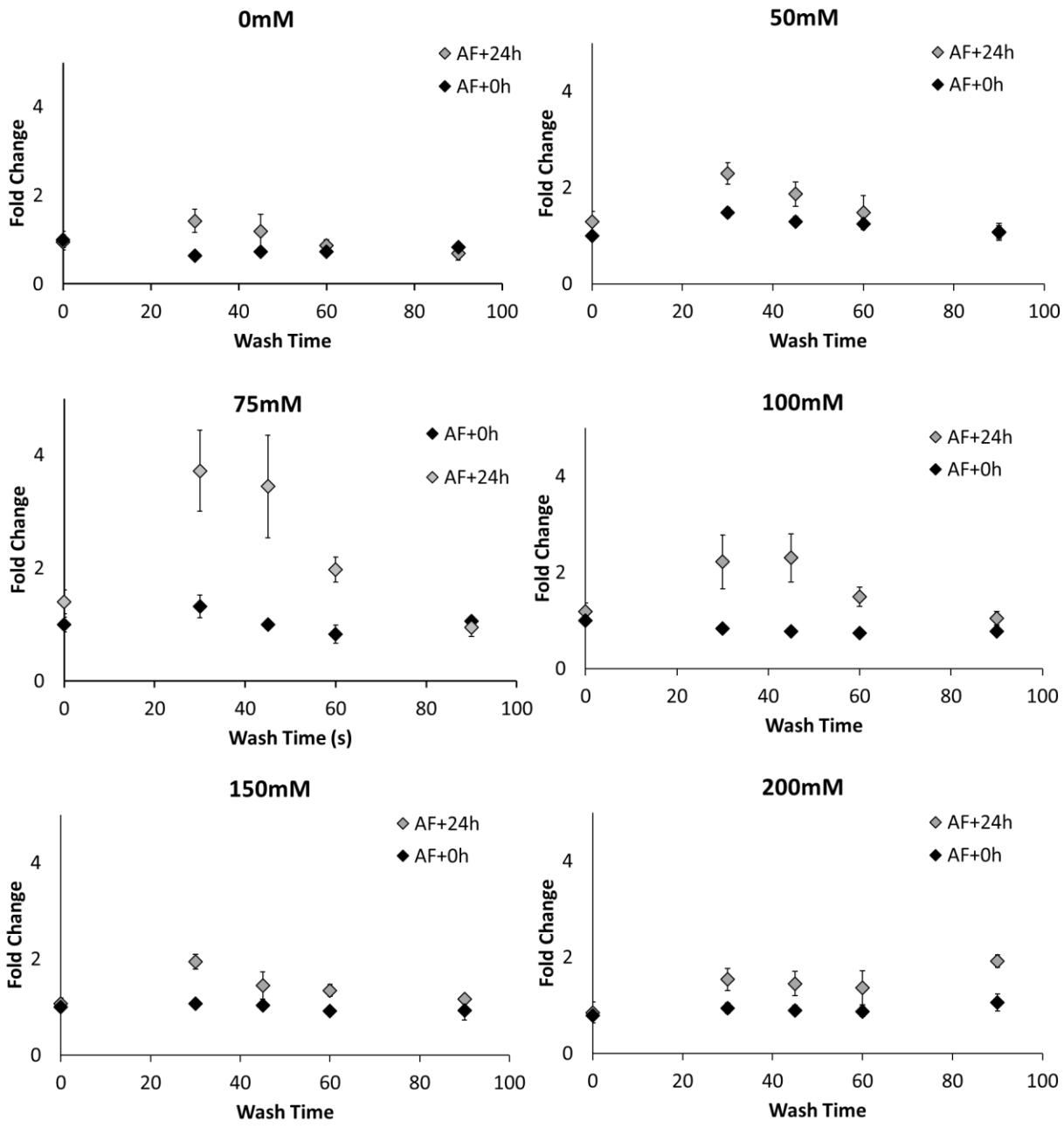

Supplemental Figure 3-3: Optimization Curves for AF washing Conditions (n=3, with 5 accumulations of 100 shots per sample). Signal improvement hovered around two-fold for most washes, except for 50 mM, which showed similar results to the 75 mM washing parameter.

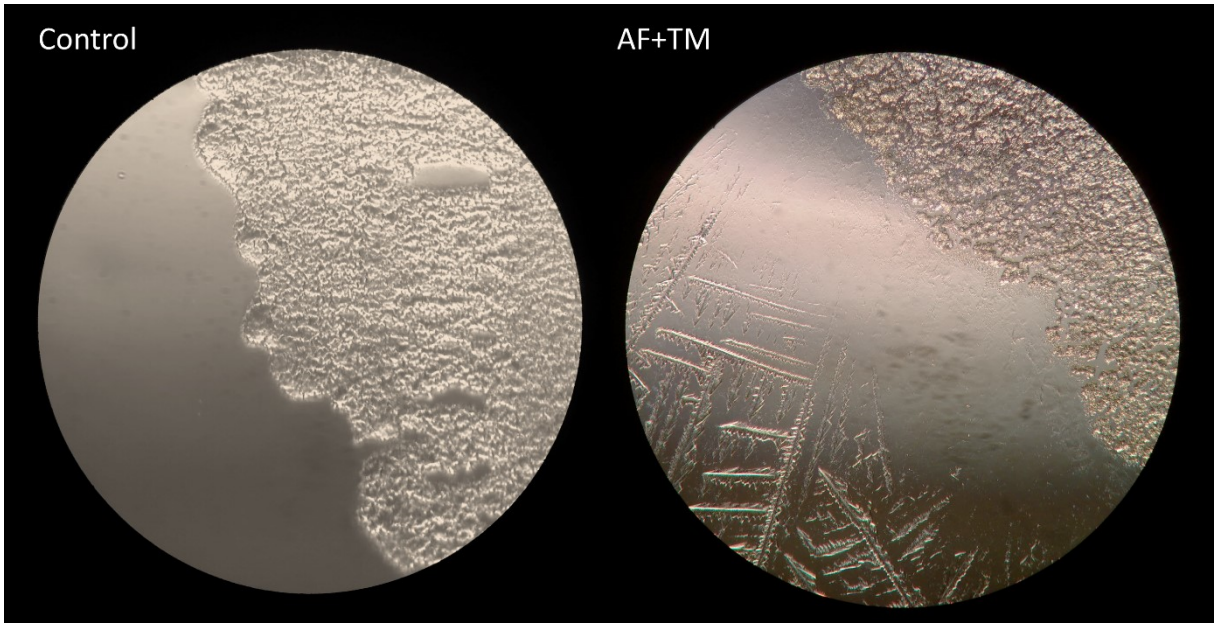

Supplemental Figure 3-4: Brightfield Images of 14 µm Mouse Brain Sections at 20X Magnification Before and After 30 µg/cm2 Ammonium Formate (AF) Deposition. Left panel, control section. Right panel, large crystal structures are visible off tissue after AF wash and spray deposition, while much smaller crystals can be seen around the border of the tissue section. No crystal structures were clearly observed on the section itself, suggesting that the AF deposited on the tissue sections to be more amorphous.

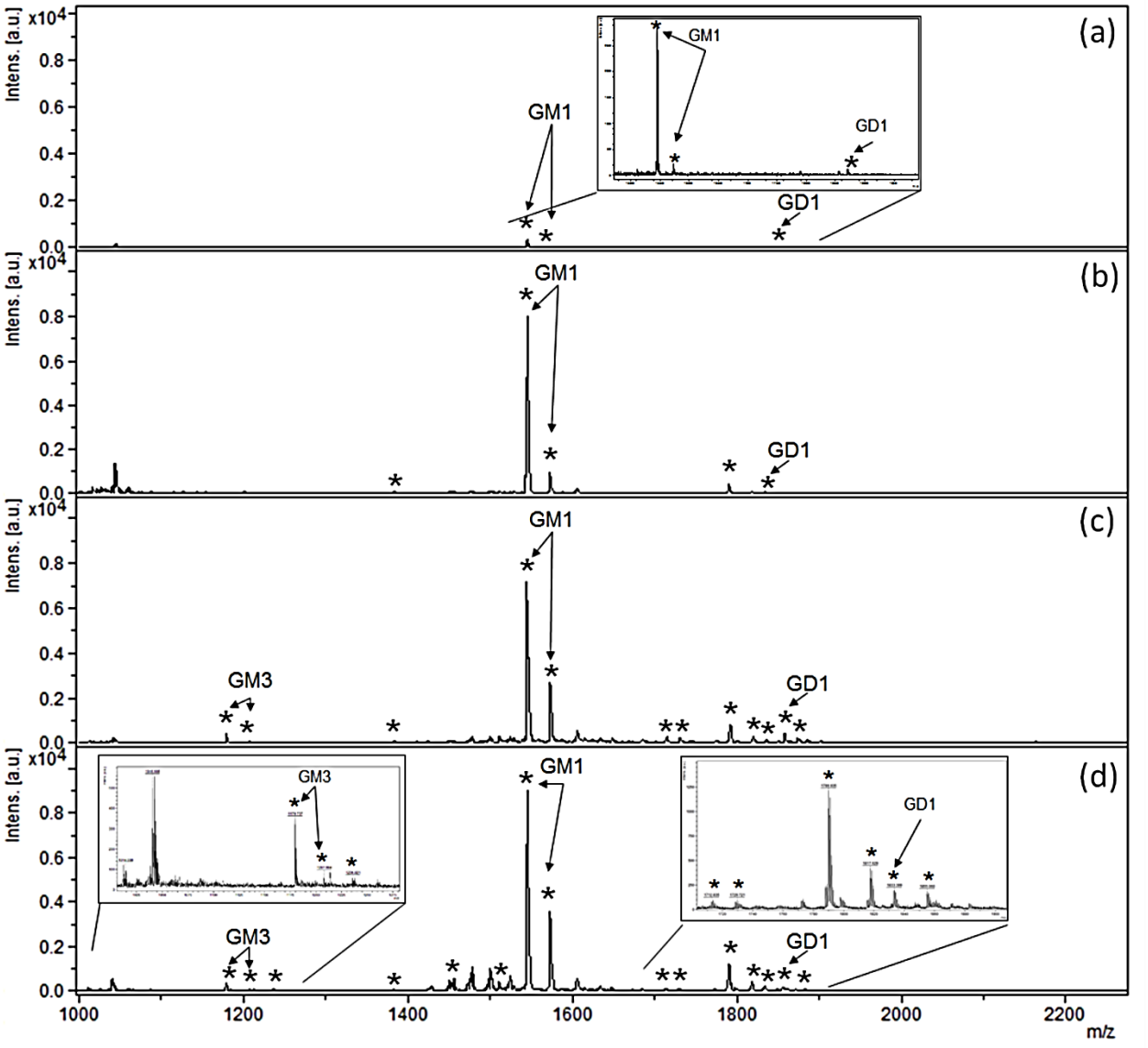

Supplemental Figure 3-5: Typical Negative Mode MALDI-TOF MS Spectra from Brain Tissue Sections Subjected to Four Different Sample Preparation Approaches: (a) the control protocol, (b) the AF+Wdip+TM+24h protocol, (c) the W+TM+24h protocol, and (d) the optimal method (AF+TM+24h). The number of sialylated species based on MS/MS determination (marked with *) increased from 3 to 15 when the optimal sample preparation method was applied. Those with full MS/MS on-tissue confirmation have been labelled according to their conventional names.

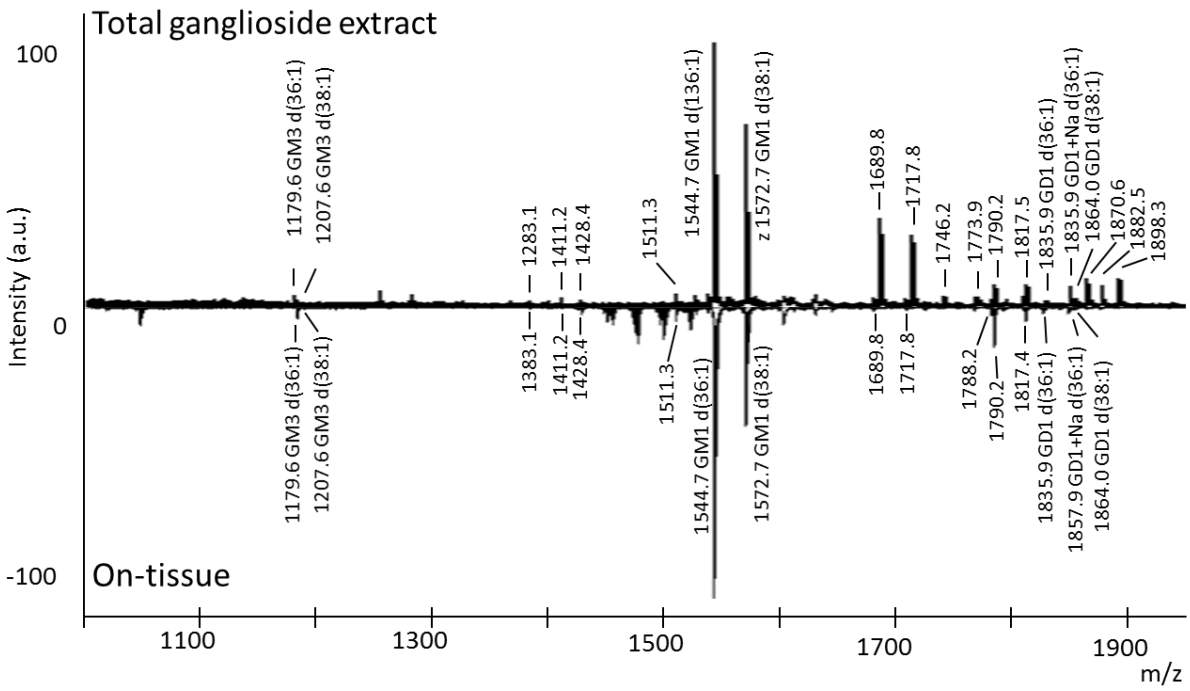

Supplemental Figure 3-6: Typical MALDI-TOF MS Profiling Data Obtained from the Total Ganglioside Extract using DAN as the Matrix (above) and On-Tissue Using the Optimal Method (below). Sialylated species indicated by their m/z value have been confirmed by exact mass and partial MS/MS (minimally the presence of a sialic residue fragment), while those referred by their nomenclature have been confirmed by complete MS/MS.

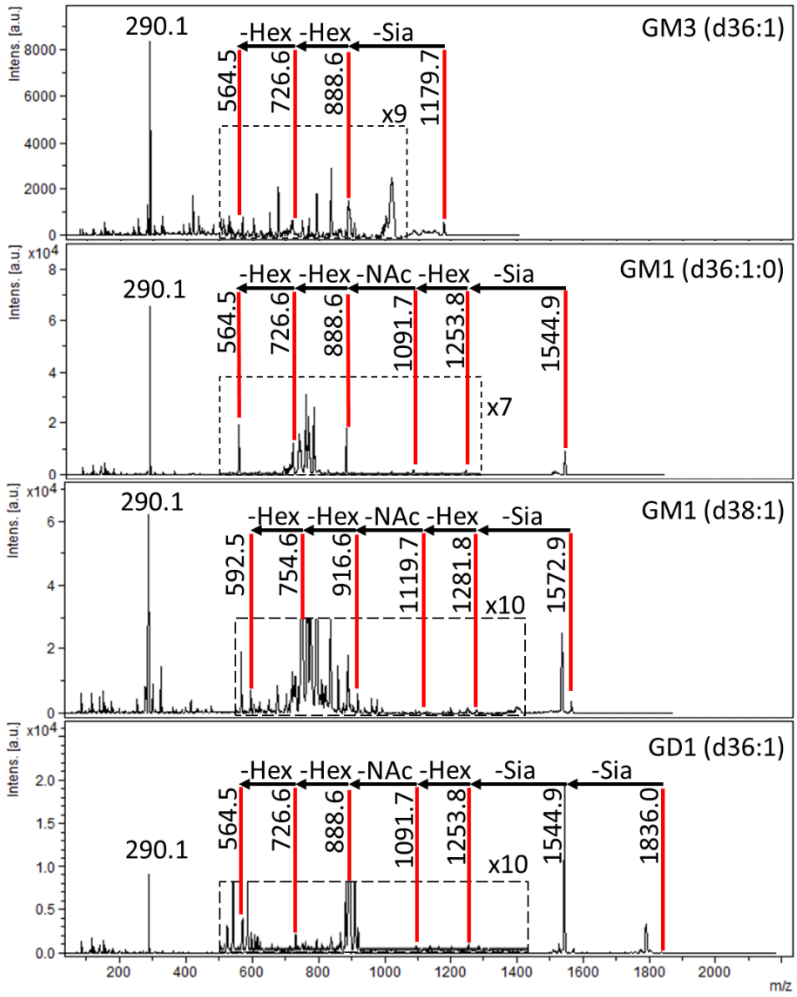

Supplemental Figure 3-7: On-Tissue MALDI-TOF MS/MS Spectra of Fully Identified Ganglioside Species Displaying a Typical Fragmentation Pathway. Sia = sialic acid, Hex = hexose (glucose or galactose), NAc =N-Acetylgalactosamine. Low intensity fragment signals have a minimum S/N of 3.

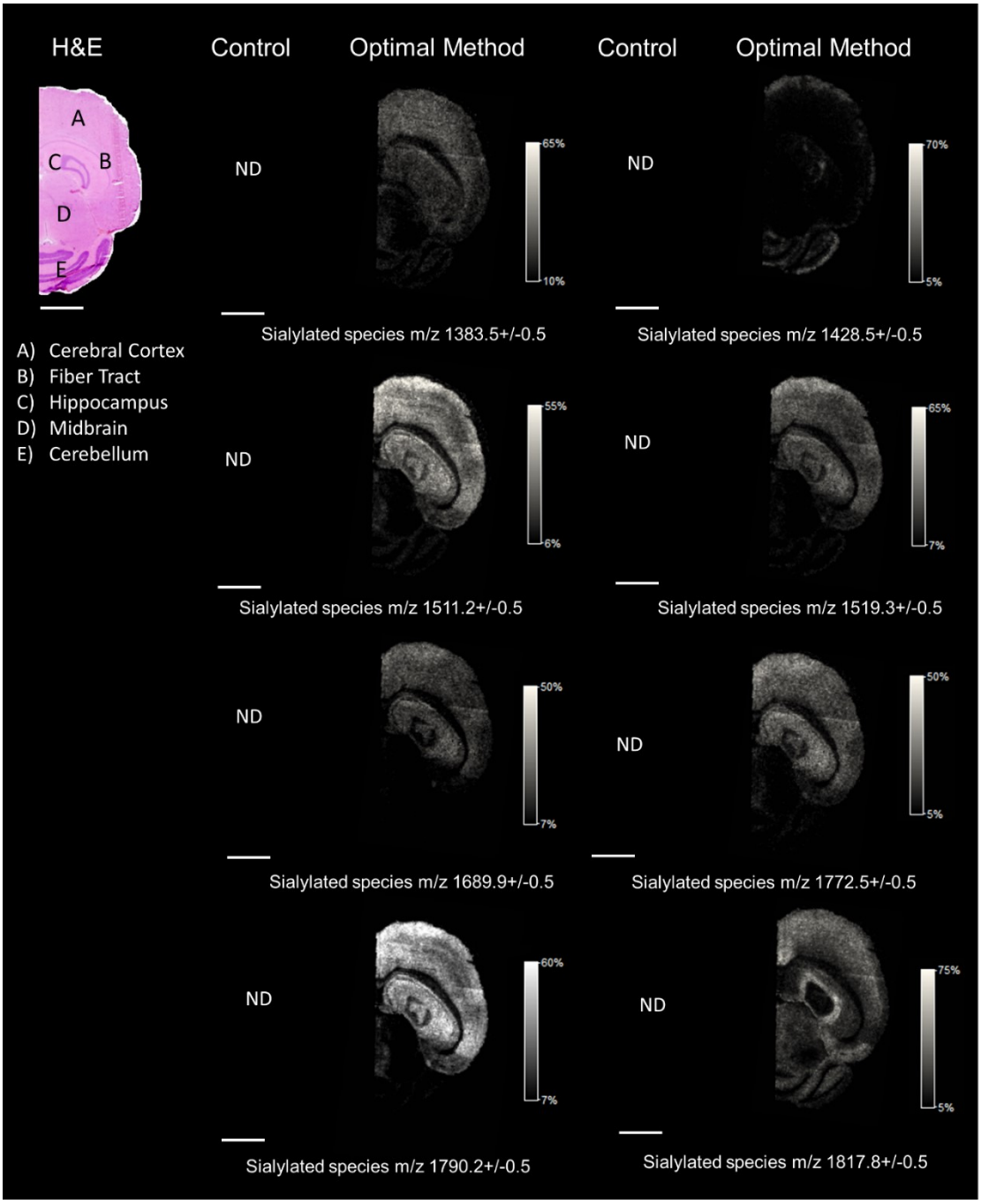

Supplemental Figure 3-8: MALDI-TOF IMS of Purported Unidentified Sialylated Species from Serial Horizontal Mouse Brain Tissue Sections subjected to the control and optimal preparation method, respectively. The results were acquired in one IMS experiment and at a lateral resolution of 65 μm. ND: not detected.

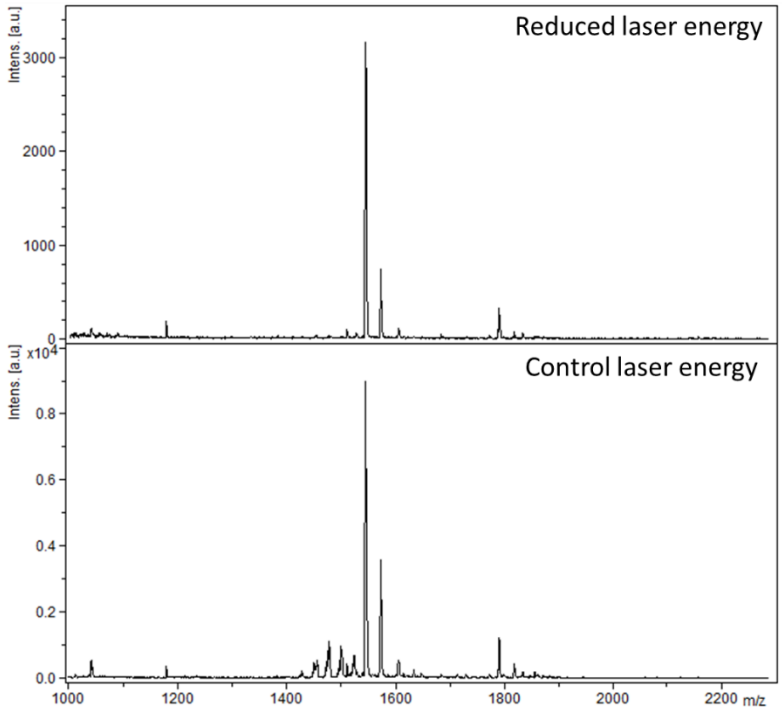

Supplemental Figure 3-9: MALDI-TOF MS Spectra Acquired on a Mouse Brain Tissue Section in the Hippocampal Area after the Optimal Section Processing Method was Applied. The quality of the GM1 signal was not comprised at a reduced laser energy (8% drop in laser power with respect to that needed for the control method taking into account the Global and Method instrument attenuation settings), which still allowed continuous ion production for successive laser shots on the same section coordinate.

Chapter 4: Silver Spray Deposition for AgLDI Imaging MS of Cholesterol and Other Olefins on Thin Tissue Sections

Ethan Yang, Frédéric Fournelle and Pierre Chaurand

Journal of Mass Spectrometry, Special Issue, Volume 5, Issue 4, Page e4428, April 2020

Author Contributions:

- Ethan Yang came up with the experimental designs, acquired and interpreted all the IMS results, and produced all the figures for the manuscript other than the ones listed under Frédéric Fournelle.
- Frédéric Fournelle, current PhD student in the laboratory, acquired the crystal size data for Supplemental Figure 4-2 as well as created **Figure 4-2** and **Figure 4-4** based on the data Ethan Yang produced**.**
- Prof. Pierre Chaurand, doctoral supervisor, provided the necessary advice and support during the experimentation and helped finalize the manuscript.

4.1. Abstract

Olefins such as cholesterol and unsaturated fatty acids play important biological roles. Silver assisted laser desorption ionization (AgLDI) takes advantage of the strong affinity of silver to conjugate with double bonds to selectively ionize these molecules for imaging mass spectrometry experiments (IMS). For IMS studies, two main approaches for silver deposition have been described in the literature: fine coating by silver sputtering and spray deposition of silver nanoparticles. While these approaches allow for extremely high resolution IMS experiments to be conducted, they are not readily available to all laboratories. Herein we present a silver nitrate spray deposition approach as alternative to silver sputtering and nanoparticle deposition. The silver nitrate spray has the same level of specificity and sensitivity for olefins, particularly cholesterol, and has shown to be capable of IMS experiments down to 10 μm spatial resolution. Minimal sample preparation and the affordability of silver nitrate make this a convenient and accessible technique worth considering.

4.2. Introduction

Matrix assisted laser desorption ionization (MALDI) imaging mass spectrometry (IMS) is a powerful analytical technique that can provide insight into the distribution of biomolecules within thin tissue sections[109, 204, 288]. Originally introduced for proteomic studies, this technology is now widely adopted for lipidomic studies thanks to the discovery of novel matrices and sample preparation approaches[60, 144, 215, 289]. Beyond traditional organic matrices, metal matrices have also been studied to determine their ability to aid with the desorption ionization of specific biomolecules for MS and IMS studies[41, 237, 239, 290-294]. Tanaka *et al*. firstly described the use of cobalt for analysis of protein up to 100 kDa[41]. Since then, other metals and metal salts have also been employed. This includes the use of cesium chloride for detecting gangliosides[237], titanium dioxide sol-gel for proteins such as cyclodextrin and insulin[290], palladium colloids for drug compounds[291], pretreated nickel oxide and lithium oxides for monosaccharides[292, 293] and platinum for insecticides in plant leaves[294]. Our group deposited sodium salt followed by a nanolayer of gold (CBS-AuLDI) to selectively enhance the detection of triacylglycerols (TAGs)[239]. An extensive summary of the multiple metal assisted LDI MS approaches developed in the past decades is provided by Shi *et al*.[295].

Of the various metals investigated, silver is one of the most characterized because of its strong affinity for conjugating with double bonds[296, 297]. This characteristic has kept it as the dopant of choice in mass spectrometry analyses of a vast array of molecules including nonpolar hydrocarbon polymers[298], carotenoids and tocopherols[299], peroxide products of various phospholipids and fatty acids[300, 301], monosaccharides[302], flavonoid glycosides[303] and even aromatic hydrocarbons[304]. It can be used to quantify olefin contents in samples when the appropriate internal standard is selected[297]. For IMS, silver nitrate was introduced as a dopant of the solvent spray of DESI (desorption

electrospray ionization) IMS by Jackson *et al.* where they investigate Ag^+ adduct of 26 biologically relevant lipid species[305] and more recently in nanoDESI IMS allowing quantification of prostaglandins as silver adducts[306]. Siuzdac's group demonstrated the use of silver nitrate salt to form a rich cation environment on porous silicon nanostructure targets for an enhanced detection of cholesterol and glucose in human serum by nanostructure-initiator mass spectrometry (NIMS)[307]. Our group developed a silver-assisted laser desorption ionization (AgLDI) approach that deposited silver nanoclusters through bombarding solid elemental silver with a beam of charged argon molecules in a vacuum, known as sputtering[146]. This dry deposition technique optimized on a mouse brain showed strong specificity for olefins and allowed for IMS analysis at the limit of the laser spot size[146]. Its overall simplicity in sample preparation-cryosectioning followed by silver deposition by sputtering-has seen its application to other type of samples including human carotids[308], murine fore-stomach[309], mouse liver samples[310], human colorectal cancer liver metastasis samples[260] and to a larger extent, fingermarks[309, 311-313]. However, the overall adoption in the IMS community remains relatively sparse, possibly because of the need for the specialized sputtering system. Schnapp *et al*. described a silver foil blotting technique for the detection of many classes of olefins[314]. Most other researchers have cited the silver sputtering approach but instead introduced different flavors of silver nanoparticles (AgNPs) sprayed onto samples as an IMS approach for detecting olefins and other endogenous species such as beta-amyloid peptides, phospholipids and triacylglycerols[145, 243, 315-317]. While nanoparticles are exciting and provide the sensitivity and spatial resolution required in IMS, they can be especially difficult to prepare for those without the proper training and know-how to reproduce, even when the synthesis recipe is followed to the dot.

In this work, we propose a friendlier AgLDI IMS approach that does not require extra instrumentation nor knowledge in nanoparticle synthesis. By returning to silver salts, we were able

to spray deposit a homogeneous layer of silver cations onto thin tissue sections and obtain IMS results on brain tissue sections comparable to that of sputtering down to 10 µm spatial resolution. While it cannot match spatial resolution of previously published approaches, this technique has the same level of sensitivity. Plus, its overall simplicity and affordability makes it an attractive alternative and easy first step for IMS experiments targeting olefins. To our knowledge, this is the only research report that describes in detail an IMS approach for olefin detection using silver salts.

4.3. Experimental

4.3.1. Materials & Reagents

The silver nitrate ($AgNO_3$) and acetate (AgAc) were obtained from Sigma-Aldrich Canada (Oakville, ON, Canada). All solvents used were purchased from Thermo Fisher Scientific (Ottawa, ON, Canada). While $AgNO_3$ is not highly toxic, it stains relatively easily. Wear gloves when handling. Immediate washing with H_2O or acetonitrile (ACN) in 1% TFA will help to remove the stain, which normally appears the next day after the spill.

4.3.2. Tissue Sampling and Sectioning

Fresh frozen mouse brains were obtained from twelve-week-old mice. Immediately after euthanization in CO_2, the brains were removed from the animals, wrapped in aluminum foil and placed on dry ice. They were then stored at -80°C until use. The tissue procuration protocol for this study has been approved by the local Ethical Committee of the Université de Montréal.

Frozen mouse brain homogenate blocks were used to optimize the silver spray method. The homogenate blocks were produced as per the protocol outlined by Groseclose and Castellino[318]. Briefly, multiple brains were manually cut into small pieces with surgical blades then added into an Eppendorf tube containing metallic beads and broken into finer pieces through mechanical shearing for 30 mins. A shortened straw two millimeter in diameter was plunged directly into the

homogenate, embedding within approximately 100 µL of homogenate. The straw with the homogenate was then immediately frozen on dry ice and kept in the -80°C until needed. For each step of sample optimization, three consecutive sections were obtained at 20 µm thickness using a Thermo Fisher Scientific Microm^{TM} HM550, thaw-mounted onto indium–tin-oxide (ITO) microscope slides (Delta Technologies, Loveland, CO, USA), and desiccated for <1 hr before further sample preparation. The consecutive sections represented technical triplicates. Experimental replicates were also performed, indicated by the letter "n."

For all other experiments, non-homogenized horizontal mouse brain sections cut at 12-µm thickness were used. Serial sections were obtained for H&E staining as described in Supplemental Table 4-1.

4.3.3. Silver Salt Manual Spotting

Two solutions, one of $AgNO_3$ and another of AgAc both at 8.5 mg/mL and dissolved in 3:1 ACN:H_2O and 0.1% TFA, were pipetted individually onto the cerebellum of a mouse brain section. Two consecutive 1 µL drop of either solution were overlaid upon drying of the first drop.

4.3.4. Silver Salt Spray Deposition

Silver nitrate at 8.5 mg/mL in 100% MeOH and 0.1% TFA was deposited using a first-generation TM-Sprayer (HTX Technologies, Chapel Hill, NC) with the following protocol: 0.075 mL/hr flow rate, 500 mm/min track velocity, 4 mm track spacing with a 2 mm offset for even-numbered passes, 20 psi air pressure and 45°C nozzle temperature. The optimal amount of silver salt was evaluated at 24 passes, equivalent to 0.76 mg/cm^2 thickness. The thickness was estimated using the following equation provided by HTX Technologies:

$$W = \frac{NP * FR * C}{V * TS}$$

where W = thickness, NP = the number of passes, FR = the flow rate (mL/min), C = concentration

of salt sprayed (mg/mL), V = track velocity (mm/mins) and TS = track spacing (mm). The actual thickness deposited was obtained from weighing a clear glass slide (25 mm x 25 mm) before and after salt deposition and dividing this weight from the area of the glass slide. Triplicate depositions were made to obtain an average, which was determined to be 0.78 ± 0.01 mg/cm^2. Because of the high agreement between the calculated and actual thickness deposited (<5% variation), all thicknesses presented in the results section are based on the calculated thickness.

4.3.5. Silver Sputter Deposition

Silver deposition by sputtering was accomplished as per the protocol outlined in Dufresne *et al.* with the same instrumental parameters[146]. Briefly, a layer of approximately 28 nm of silver was deposited onto the tissue section using a Cressington 308R sputter coater from Ted Pella Inc. (Redding, CA, USA) at an argon partial pressure of 0.02 mbar and a current of 80 mA.

4.3.6. LDI Mass Spectrometry

All mass spectrometry data was acquired with a MALDI TOF/TOF ultrafleXtreme MS instrument in positive ionization mode reflectron geometry at an acceleration voltage of +25 kV (Bruker Daltonics, Billerica, MA, USA). This model is equipped with a 2 kHz SmartBeam II Nd:Yag/355 nm laser with an approximate 15 µm diameter in the "minimum" focus setting. Instrumental parameters such as delayed extraction, source voltage and laser energy, were initially optimized to maximize the signal to noise ratio (S/N) of cholesterol on a set of brain homogenate tissue sections on which was deposited two drops of 1 µL silver nitrate solution. The same instrument settings were maintained throughout the entire sample optimization procedure. The instrumental parameters were re-optimized for the sputtered samples. In all cases, flexControl (v 3.4) and flexImaging (v 4.1) were used to operate the instrument during data acquisition (Bruker Daltonics, Billerica, MA, USA). For sample optimization, an array of 15 by 15 pixels at 100 µm

spatial resolution were obtained from the middle of the homogenate at 200 shots per pixel. For spray deposition and sputter deposition comparison, 100 µm and 20 µm spatial resolution IMS data were obtained at 200 shots per pixel on three brain tissue sections. A mass accuracy of <10 ppm was achieved for all spectra thanks to possibility for internal calibration with silver clusters observed throughout the spectra. Lipid identification was performed by comparing accurate mass measurement with LIPID MAPS (http://www.lipidmaps.org/) and confirmed by MS/MS measurements with the ultrafleXtreme TOF-TOF in LIFT mode.

4.3.7. Data Analysis

IMS data were visualized in flexImaging (4.1) without normalization (Bruker Daltonics, Billerica, MA, USA). To optimize the silver deposition approach, means from triplicate measurements of the total cholesterol signals from the mouse brain homogenate tissue sections were compared. The total cholesterol signal is the average intensity of the sum of the intensities from the two argentitated cholesterol signals at *m/z* 493.2 $[M+Ag_{107}]^+$ and *m/z* 495.2 $[M+Ag_{109}]^+$ on a given brain homogenate. To calculate the total cholesterol signal, raw data were first internally recalibrated with known silver cluster peaks using the Batch Processing function of flexAnalysis (v 3.4) then exported in the vendor neutral imzML format (Bruker Daltonics, Billerica, MA, USA). The imzML data was imported in the R environmental (v 3.4.4). The data was then normalized by total ion current (TIC) with the Cardinal package (v 2.1)[224]. MALDIquant[319] (v 1.19.3) was then used to calculate the S/N of the cholesterol signals. Pixels with S/N<10 were discarded. Finally, the intensities of the two cholesterol signals of the remaining pixels were extracted with the Cardinal package (v 2.1)[224]. After removing the top and bottom 10% in intensity of the remaining pixels, these signals were averaged then summed. The final intensity obtained is the total cholesterol signal. Multivariate ANOVA was used to determine if any of the tested parameters

(thickness, choice of solvent system and percentage of acid) were statistically significant, and if so, a Tukey's statistical test was used to assess the significance between the values.

4.4. Results & Discussion

4.4.1. Silver Salt Selection

When considering silver salts, silver nitrate immediately comes to mind as it is widely used in LC-MS[320-323] and GC-MS[324-326]. It is also one of the most affordable out of the silver salts commercially available. Given the same budget, it is possible to purchase five to ten times more silver nitrate than any other silver salts. The cost alone would have made silver nitrate an easy choice, given that the ionization efficiency of cholesterol should remain relatively similar for the different silver salts. A quick profiling test by manually spotting the silver salts on mouse brain homogenate tissue sections confirmed that the spectral profiles obtained with silver nitrate and silver acetate are highly similar for cholesterol, with silver nitrate somewhat superior at detecting lower mass species (**Supplemental Figure 4-1**). However, beyond the concern of cost, the solubility of the silver salt is of utmost importance. In order to maximize the attainable spatial resolution, a silver salt soluble in organic solvent is necessary because spray solvents with organic components dry faster and is presumed to lead to finer crystals while minimizing analyte delocalisation (see below). Out of the silver salts considered, silver nitrate is highly soluble in acetonitrile (ACN) and soluble in methanol (MeOH), the two most prevalent organic components used as spray solvents. Because of these advantages, silver nitrate was selected as the silver salt for further studies.

4.4.2. Silver Nitrate Thickness Optimization

The amount of silver nitrate deposited on the tissue sample has a direct impact on the intensity of the detected cholesterol signal. This was confirmed by comparing the total cholesterol signal at

varying thicknesses of $AgNO_3$ deposited from a 8.5 mg/mL solution (3:1 ACN:H_2O and 0.1% TFA). Thirteen different thicknesses at 0.09, 0.13, 0.17, 0.26, 0.34, 0.43, 0.51, 0.60, 0.68, 0.77, 0.85, 1.02 and 1.28 mg/cm^2 were tested by spray depositing 4, 6, 8, 12, 16, 20, 24, 28, 32, 36, 40, 48 and 60 passes respectively at a flow rate of 0.05 mL/hr and all other parameters consistent with that indicated in Materials and Method. A slow velocity and flow rate were chosen because previous tests on our system using 2,5-DHB showed that this combination provided an even coating visually similar to sublimated 2,5-DHB (data not shown).

As shown in **Figure 4-1a**, the total cholesterol signal increased logarithmically as the thickness o f the $AgNO_3$ increased linearly. Specifically, the total cholesterol signal doubled between 0.09 and 0.17 mg/cm^2, once more between 0.17 and 0.34 mg/cm^2. The increase slowed and plateaued at 0.77 mg/cm^2. Multivariate ANOVA and Tukey's test revealed that the total cholesterol signal at 0.77 mg/cm^2 is statistically significantly different from the total cholesterol signal at 0.34 mg/cm^2. The plateau observed signifies that enough $AgNO_3$ has been deposited onto the sample to allow for maximal desorption and ionization for the amount of cholesterol present in the sample, and that an increase in the amount of silver salt does not improve the total cholesterol signal. Surprisingly, the $AgNO_3$ layer is more than double that of conventional MALDI matrices indicated in the literature to be around 0.2 mg/cm^2 in thickness[60, 219]. It is important to note that the amount of $AgNO_3$ deposited on the tissue may vary based on the thickness of the tissue section and its histology including the amount of cholesterol present in the sample. Because the silver ions act as the ionization agent, an excess of $AgNO_3$ is required to maximize cholesterol ionization probability. For samples with lower cholesterol content, a thinner coating may be sufficient. A representative mass spectrum acquired from a mouse brain homogenate section is shown in **Figure 4-1c**, with the major silver clusters, cholesterol and other olefins highlighted.

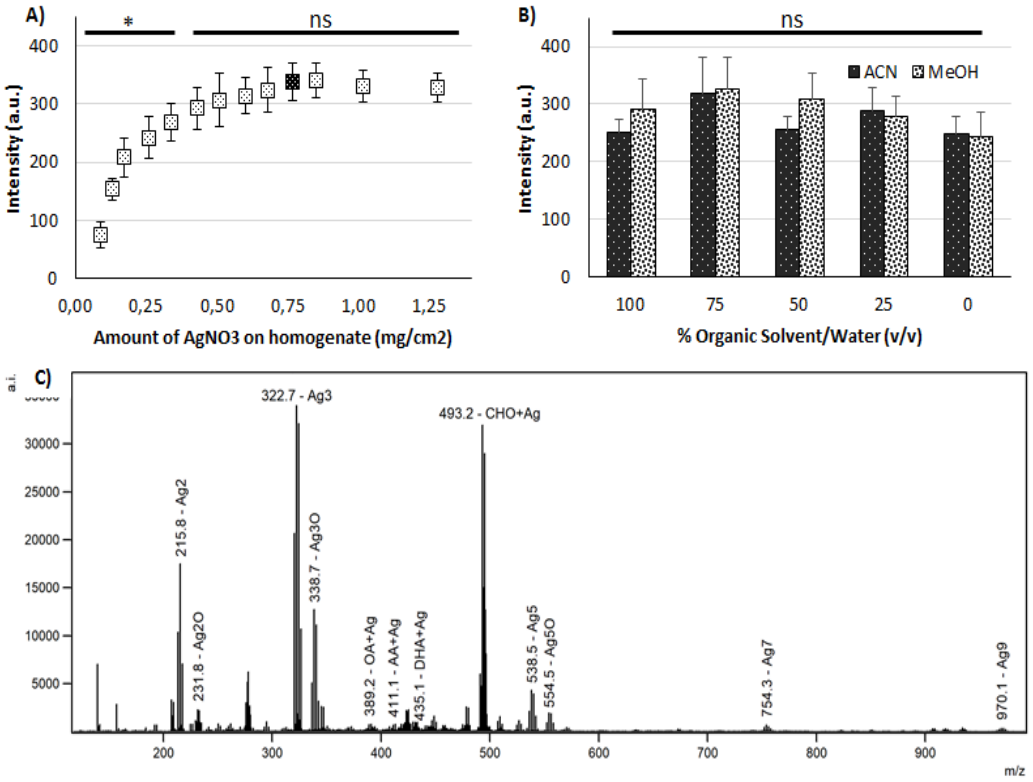

Figure 4-1: Optimization of Silver Nitrate Spray Deposition on Mouse Brain Homogenate sections. A) Mean total cholesterol signal intensity (n=5) as a function of the amount of silver nitrate (AgNO3) deposited on tissue determined from 0.09 to 1.28 mg/cm2 over thirteen points. The minimal thickness where the total cholesterol signal stabilized was 0.77 mg/cm2. Thicknesses whose total cholesterol intensity is significantly less ($p < 0.05$) are marked by *. B) Mean total cholesterol signal intensity comparison across different solvent systems (n=3). No statistical significance amongst the compared solvent systems were found. C) A representative MS spectrum acquired from a mouse brain homogenate section with the optimal thickness of AgNO3 deposited. Major species including silver clusters are identified. CHO = cholesterol, AA = arachidonic acid, OA = oleic acid, AgxO = silver oxide

4.4.3. Solvent System Optimization

In MALDI IMS, the solvent system for matrix deposition is important not only to ensure the

solubility of the matrix, but also the co-crystallization of the matrix with the analyte[327].

Additionally, solvents chosen for IMS should also limit the amount of analyte delocalization during matrix deposition in order to maximize the obtainable spatial resolution. In AgLDI IMS after silver spray deposition, the detection of cholesterol and other olefins as silver cationized ions suggests that solvent extraction of these molecules may play a crucial role in the efficacy of this technique. Luckily, silver nitrate is soluble in the three standard solvents predominantly used in MALDI: acetonitrile (ACN), methanol (MeOH) and water (H_2O). To test these different solvent systems, solutions of 8.5 mg/mL silver nitrate in various proportions of ACN:H_2O or MeOH:H_2O and 0.1% TFA (100%, 75%, 50%, 25% and 0% organic) were spray deposited on mouse brain homogenate sections and the total cholesterol signal across the homogenate was compared. As can be seen in **Figure 4-1b**, the total cholesterol signals of the various solvent systems are within one standard deviation of each other. The highest absolute value attributed to the 75% organic and the lowest to 0% organic. While cholesterol is only slightly soluble in ACN and MeOH, it is possible that there is a slight solvent extraction effect leading to the improved detection. This extraction is minimal at 100% organic because in this case, the spray deposition is completely dry: no microdroplets are observed on glass slides throughout the entire deposition.

While there are no clear quantitative differences in the total cholesterol signal, there is a qualitative difference in the silver deposition summarized in **Figure 4-2**. For one, the crystal size off-tissue increases with the percentage of water in the solvent system, shown in the top row of each cell in **Figure 4-2**. This may be because the high solubility of $AgNO_3$ in water allows the salt to fully resolubilize with each new spray passage and aggregate into larger crystals rather than forming even coatings of small crystals. This observation is supported by the much smaller crystal dimension below 100 μm at 100% MeOH and 0.1% TFA compared to all other spray systems, the

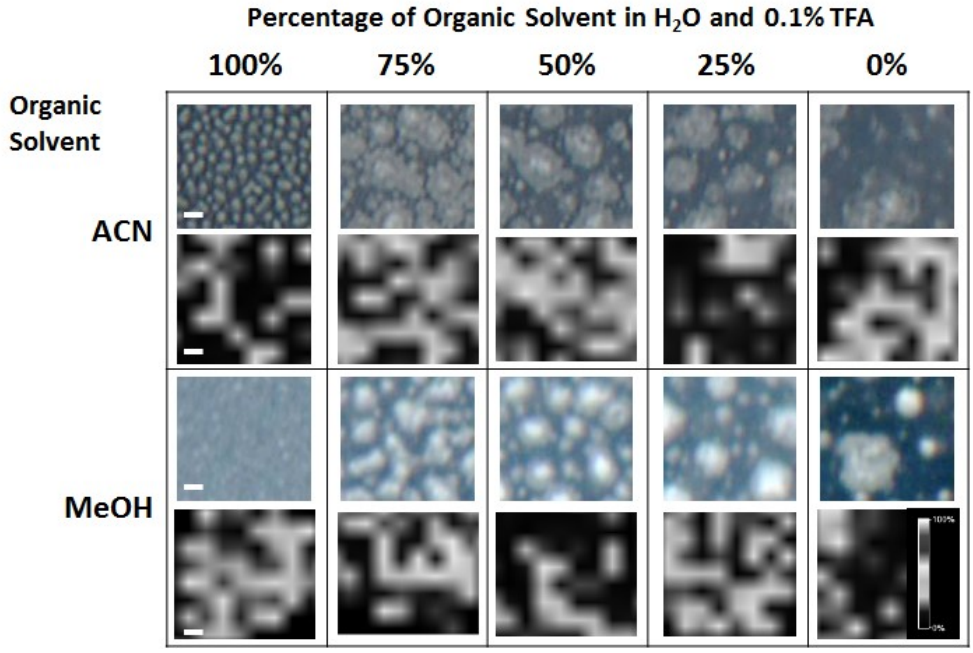

Figure 4-2: Effects of Solvent System on Crystal Size and Deposition Homogeneity. In each cell: optical image of the silver nitrate salt crystals off-tissue after the optimal spray deposition (top) and IMS results of the Ag3 cluster at m/z 323.7 on the brain tissue homogenate (bottom) of the exact solvent system tested. The type of solvent is indicated in each row, while the solvent composition (in %) is marked in each column. The remaining percentage is water in 0.1 % TFA. It is evident that a decrease in organic content leads to an increase in crystal size formation off-tissue and a decrease in overall deposition homogeneity. IMS results shown are TIC normalized. Scale bar represents 100 μm.

solvent in which $AgNO_3$ is the least soluble. While the crystal size off-tissue does not necessary translate to large crystals on-tissue, as demonstrated in the CBS-AuLDI method[239], the continuous re-solubilization of the highly water soluble $AgNO_3$ in aqueous solutions may lead to large crystal aggregates on tissue and result in a less than homogeneous sample. This may be problematic particularly for the spray parameter proposed in this thesis because the velocity and flow rate are 500 mm and 0.075 mL/min rather than at 1000 mm and 0.10 ml/min, the values typically found in

the literature. The slower velocity may provide the environment for large aggregates to form. In fact, comparisons of the Ag_3 cluster signal at *m/z* 322.7 from the brain homogenates indicated a change inhomogeneity depending on solvent composition (**Figure 4-2).** For the MeOH series, the homogeneity increases with increasing organic component, where at 100% MeOH and 0.1% TFA the coating is highly uniform minus the dead pixels present. For the ACN spray series, the trend is also true, except at 100% ACN and 0.1% TFA. With this spray, hotspots were detected, suggesting that the salt crystals re-solubilized and aggregated during the spray. To allow for the fastest drying between passes and minimal salt re-solubilization, 100% MeOH and 0.1% TFA was selected for further IMS analysis.

Upon selecting the most suitable solvent system, the amount of trifluoroacetic acid (TFA) was also tested to determine if its addition would enhance cholesterol detection. The mean total cholesterol signal is much lower when no TFA is added at all when compared to 0.1%, 1% and 3% (see Figure 4-3**a**). However, there is no statistical difference because of the large error bar for 0% TFA. This suggests that the silver deposition is not homogenous with 0% TFA. IMS results confirm this hypothesis, as the Ag^{3+} signal at *m/z* 322.7 from a representative mouse brain section without TFA indicates an overall lower intensity and a few hotspots skewing upwards the overall intensity. Even with 0.1% TFA added, the homogeneity and overall detectability greatly improves, and slightly decreases with increasing TFA concentration (Figure 4-3b, middle row). Interestingly, the amount of TFA appears to slightly modify how the silver salt crystallizes, as the density of the salt crystals off-tissue increases with the concentration of TFA (Figure 4-3b, top row). An increase in the amount of TFA also renders the tissue opaque, which is more easily comparable with the thinner mouse brain section (Figure 4-3b, bottom row). While this does not imply tissue damage, it has led to a somewhat lower overall value in cholesterol signal. Based on these observations, 0.1% TFA was included in the final solvent system. Lastly, various flow rate and velocity combinations were

also tested to determine if the previously selected flow rate and velocity were optimal for minimal crystal size. Optical results demonstrated that larger crystals formed when the flow rate is increased

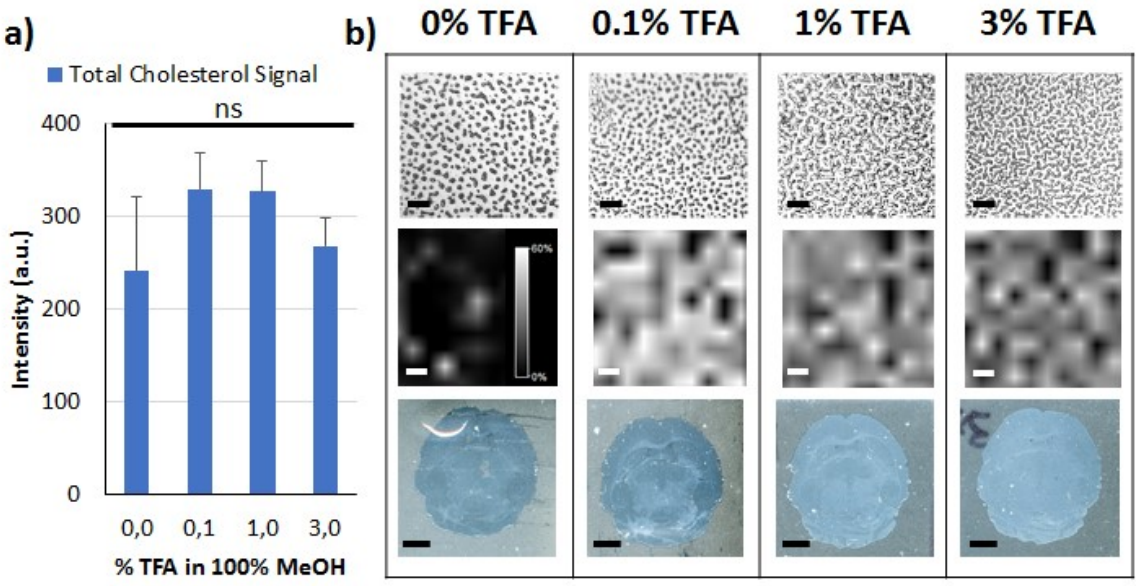

Figure 4-3: Effects of TFA concentration on total cholesterol signal and signal homogeneity. A) The mean total cholesterol signal from mouse brain homogenates (n=3) is the highest with 0.1% and 1%TFA, followed by 3% and finally no TFA. While there is no statistical difference among the concentrations, the large error bar observed at 0% TFA suggests a large variability and non-homogeneity of the detection. B) Top row: optical image of the silver nitrate salt crystals off-tissue using the optimal spray deposition reveals an increase in crystal density with increasing TFA concentration. Middle row: Non-normalized IMS results of the Ag3 cluster at m/z 323.7 on the brain tissue homogenate confirms the non-homogeneity of the silver deposition on tissue when no TFA in added. Bottom row: optical image of a mouse brain section after optimal spray deposition shows an increase in opacity. Optical images of the salt crystals were obtained using a conventional light microscope at 40x magnification without further digital zooming. Optical images of the brains were obtained using a standard bed scanner at 3200 dpi. Scale bars for first two rows represent 100 µm, while the scale bars for bottom represent 2 mm.

to the conventional spray flow rates, while no differences in crystal size due to track velocity was observed (Supplemental Figure 4-2). It would have been possible to reduce the flow rate even more. However, this would greatly increase the sample preparation time beyond the 45 minutes it currently takes to spray coat an entire slide. Therefore, to minimize crystal size and accomplish the spray deposition within a reasonable timeframe, the original parameters were kept.

4.4.4. On-Tissue Characterization of $AgNO_3$ Sprayed Samples

As expected, the $AgNO_3$ spray deposition approach provided strong specificity towards the detection of olefins, particularly cholesterol. A typical spectrum obtained from the right hemisphere of a horizontal mouse brain section shown in Figure 4-4 confirms this unique selectivity. Beyond cholesterol (CHO), other olefins have also been detected with lower intensities. These include fatty acids such as arachidonic acid (AA), oleic acid (OA) and docohexanoic acid (DHA) and other unidentified argentinated species. Tentative assignments for these were determined by exact mass and confirmed by MS/MS, which can be found in Supplemental Figure 4-3. The proposed fragmentation pathway and assignments match those shown in the literature[146, 317]. A list of other detected olefins and their tentative assignments can be found **in** Supplemental Table 4-2. While these olefins may appear to be in "low abundance" in the spectrum, their S/Ns are above 3. However, many of these were not easy to isolate or provided high enough local abundance for confident species assignment.

IMS results at 100 µm spatial resolution of the same horizontal mouse brain section are displayed in **Figure 4-4.** Of the IMS results shown, CHO, a CHO derivative, a fatty acid and an unknown argentinated species at *m/z* 906.5 are highly localized to the white matter of the brain, namely the fiber tracts found in the corpus collosum and the cerebellum. AA and DHA, on the other hand, have a greater distribution towards the midbrain

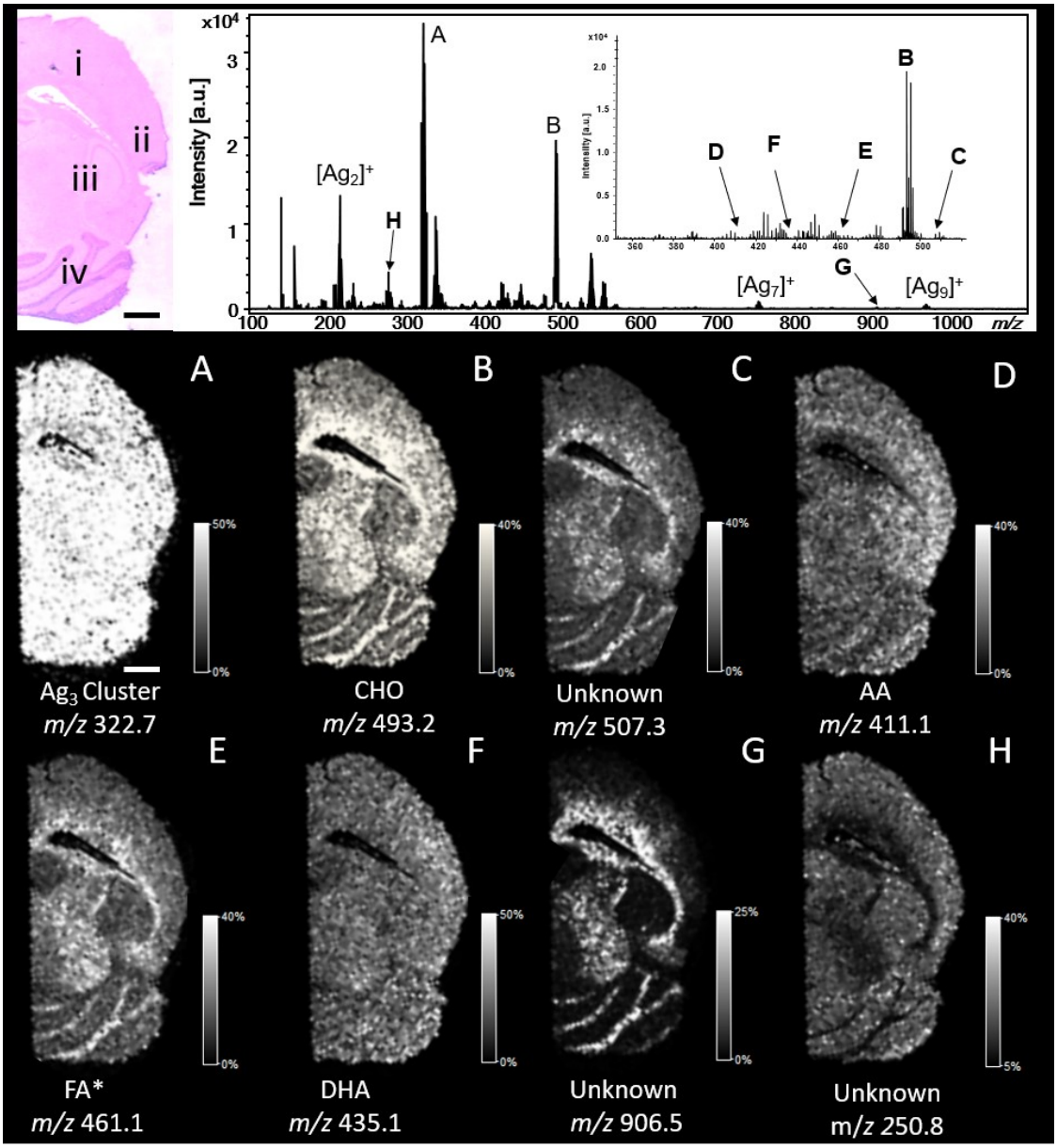

Figure 4-4: AgLDI MS & IMS at 100 µm spatial resolution from a half mouse brain section after AgNO3 spray deposition. IMS results of seven different argentinated olefin species after optimal silver salt spray deposition. The distribution of cholesterol (CHO), an unidentified fatty acid (FA) and an unidentified signal observed at m/z 906.5 were observed highly associated with the white matter, while arachidonic acid (AA) and docosahexaenoic acid (DHA) are more associated to the midbrain. An unidentified species at m/z 248.8 was more localized to the grey matter and was the mirror opposite to the unknown at m/z 906.5. The IMS result of Ag_3 cluster

confirmed the homogeneity of the silver salt deposition. An H&E staining of the serial section with the different brain regions annotated is shown at the top left: i) frontal cortex, ii) isocortex, iii) hippocampal region and iv) cerebellum. The top right displays a representative spectrum from the same brain section with the corresponding m/z species marked by corresponding letters to the top right. All scale bars represent 1 mm. Species marked by * were not fully characterized by MSMS but are tentatively assigned based on their exact mass and identifications by previous publications (see **Supplemental Table 4-2**).

region of the cortex. Finally, an unknown species at *m/z* 250.8 appears to be more localized in the grey matter, as it produces a clear negative ion image compared to CHO. H&E staining of a serial section is included in **Figure 4-4** to assist in identifying the corresponding histologies. As the instrumental capacity for high spatial resolution IMS experiments becomes more and more commonplace, it is important to investigate if the $AgNO_3$ spray approach can be employed at higher spatial resolutions. We were able to obtain high quality IMS results from a horizontal mouse brain section acquired at 50, 20 and 10 μm spatial resolutions from the hippocampal, midbrain and the cerebellar regions, respectively. The results for select olefin species as presented in **Figure 4-5**. In the cerebellum, the CHO intensity was noticeably greater in the fiber tracts. An unidentified species at *m/z* 906.5 was predominantly localized to this structure. For the cerebellum, the highest intensity was again detected in the fiber tracts, followed by the granular level surrounding it. At both 20 and 10 μm spatial resolutions, it was possible to separate the two layers based on the difference in CHO intensity alone. Interestingly, multiple lower mass species with the opposite spatial distribution were also observed, with an example at *m/z* 250.8 highlighted.

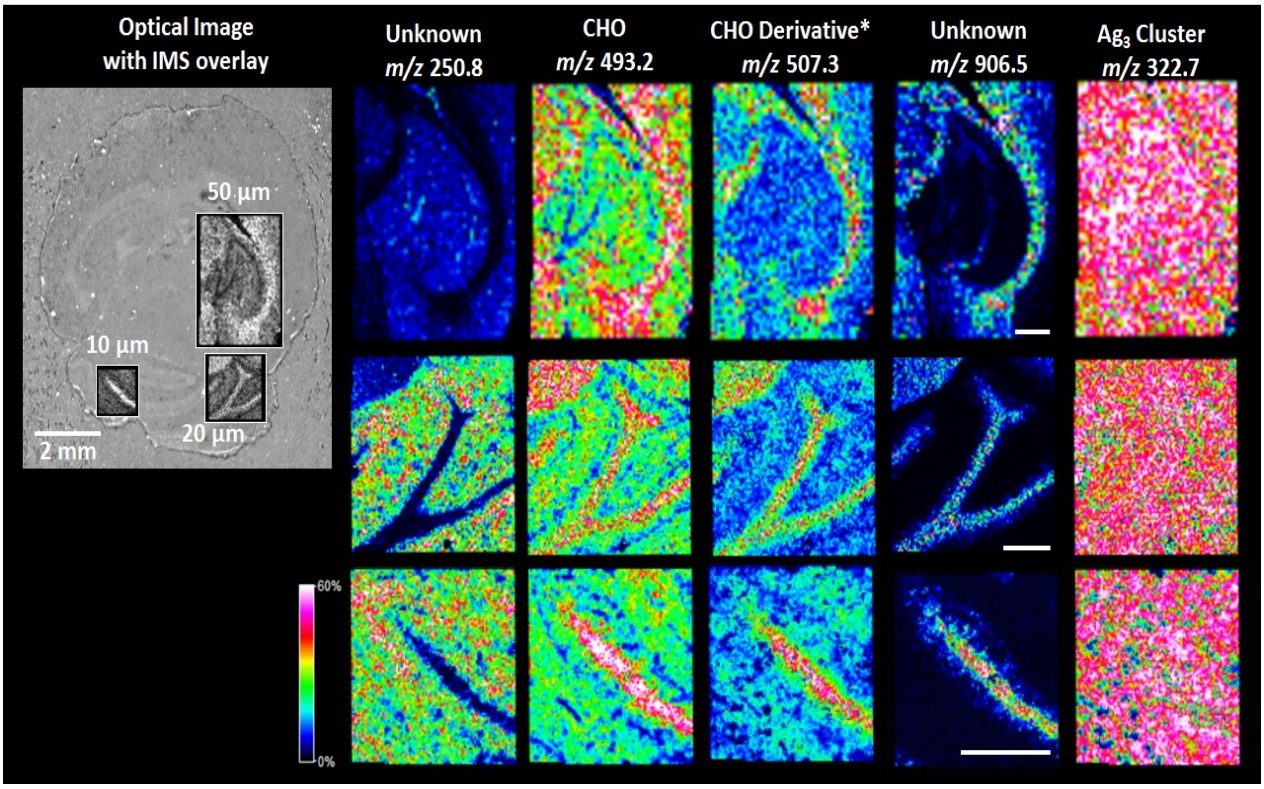

Figure 4-5: High-resolution AgLDI IMS from a horizontal mouse brain section. High resolution IMS experiments performed at 50, 20 and 10 µm spatial resolution after spray deposition of 0.77 mg/cm$_2$ of $AgNO_3$ (100% MeOH, 0.1% TFA) acquired from different brain regions all showed greater abundance for cholesterol (CHO), a cholesterol derivative and and unknown species observed at *m/z* 906.5 to the fiber tracts, while an unknown species observed at *m/z* 248.8 displayed the exact opposite spatial distribution. To the right is an optical image of the mouse brain section used with the regions that were analyzed overlayed with the IMS results of CHO (in grayscale). Unless otherwise noted, scale bars represent 500 µm. Species marked by * were not fully characterized by MS/MS but are tentatively assigned based on their exact mass and identifications by previous publications (see Supplemental Table 4-2).

4.4.5. Silver Sprayed versus Silver Sputtered IMS

Spray deposition of silver nitrate and silver deposition by sputtering yield highly similar results, as

confirmed by the mean spectra of the cerebellum obtained by both methods shown in **Supplemental Figure 4**. In both cases, the spectra are littered with silver clusters, specifically Ag^{2+}, Ag^{3+}, Ag^{5+}, Ag^{7+} and Ag^{9+}. With regards to olefins, cholesterol remains the most intense species followed by AA, OA and DHA in much lower abundance. There is also an array of signals from *m/z* 300 to 600 representing different olefins that are yet to be fully identified. The major difference between deposited and sprayed silver is the presence of oxidized silver clusters (Ag_2O^+, Ag_3O^+, Ag_4O^+ and Ag_5O^+). This may be attributed to the ambient condition under which the silver salt is sprayed as compared to the argon-filled chamber under which silver nanoparticles are sputtered onto the sample. It can also be due to regular air rather than pure nitrogen that is used as the carrier gas, introducing oxygen during the spray deposition that has led to the formation of these oxidized species. While their presence has increased the overall spectral complexity, they have not overlapped with the major olefin species detected to be considered problematic. The identities of these species were confirmed by the exact mass difference compared to their respective silver cluster and the strong agreement in the experimental isotopic pattern of these species with the predicted one calculated using IsotopePattern (Bruker Daltonics, Billerica, MA, USA).

4.4.6. Advantages and Limitations of the $AgNO_3$ Spray Approach

The $AgNO_3$ spray approach has multiple advantages compared to silver sputtering. First, and perhaps more importantly, the spray method does not require additional instrumentation. Because nearly all IMS laboratories are equipped with a spray system for matrix deposition, the spray approach is much more accessible than the sputter deposition approach. Second, the silver nitrate coating is easily removed by the standard H&E washing protocol, leaving the possibility for histological staining on the same section post-IMS. The staining must be conducted immediately after because silver nitrate will oxidize in the ambient conditions, and even faster in the presence

of light (see Supplemental Figure 4-5). Same section staining is not possible after silver sputtering, as the nanolayer deposited on the section cannot be easily removed. Lastly, the solvent system and various spray parameters can be easily adapted depending on the sample type and thickness. However, because it remains a spray approach of salts, the spatial resolution attainable cannot currently compete with the sputtered approach, whose deposition of nanoparticles forms aggregates in the nanoscale and whose spatial resolution is therefore only limited by the laser spot size. There is also much greater chemical noise compared to sputtered silver, making MS/MS analysis of low intensity olefins more difficult. The main disadvantage of the $AgNO_3$ spray approach is a practical concern. As mentioned earlier, silver nitrate stains very easily. If not cleaned quickly, spills will turn into permanent dark spots. This also implies that the spray system must be cleaned thoroughly after each deposition to ensure that the loop, the stage and other parts of the system remains clean and void of possible silver contamination. Because the sprayer is not itself a closed system, changing day-to-day ambient conditions may affect sample reproducibility, which may be drastic in regions with large variability in temperature and humidity throughout the year. Taken all the advantages and drawbacks into consideration, the $AgNO_3$ spray technique is an attractive alternative to silver sputtering for the IMS of olefins.

4.5. Conclusions

This study describes a novel AgLDI IMS approach that can be easily adapted in all laboratories equipped for IMS experiments. Specifically, this method utilizes a standard pneumatic spray deposition instrument to coat the sample with an even layer of $AgNO_3$ at 0.77 mg/cm^2 thickness. Like the sputtered deposition approach, this technique is sensitive and selective for olefin compounds and is also amenable to high resolution IMS, down to 10 µm spatial resolution. While it cannot compete with the sputtered technique for the highest spatial resolution attainable[146], nor

with the polyvinylpyrrolidone capped silver nanoparticle (PVP-AgNPs) spray technique for the largest family of biomolecules detected[145], the $AgNO_3$ spray approach is much simpler and the most affordable. It can be easily adapted for various tissue types and thicknesses and requires minimal sample preparation. As such, the $AgNO_3$ spray approach should be considered as a standard go-to technique for IMS analyses of olefins.

4.6. Acknowledgements

The authors acknowledge funding from the Natural Sciences and Engineering Research Council of Canada (NSERC) and the Canadian Foundation for Innovation (CFI). The authors would also like to thank Prof. Jean-François Masson (Dept of Chemistry, Université de Montréal) for unlimited access to the sputtering system and Dr. Nidia Lauzon of the Drug Discovery Platform at the Glen Site of the Research Institute of the McGill University Health Centre (RI -MUHC) for access to their MALDI-TOF/TOF instrument.

4.7. Supplemental Information

Supplemental Table 4-1: H&E Protocol Applied. Detailed protocol for H&E staining for mouse brain sections.

Step	Solution	Time
1	95% ethanol	30 seconds
2	70% ethanol	30 seconds
3	De-ionized water	30 seconds
4	Gill 3 Hematoxylin	15 seconds
5	De-ionized water	10 seconds
6	0.007% Sodium Bicarbonate in H_2O	5 dips
7	70% ethanol	30 seconds
8	95% ethanol	30 seconds
9	Eosin	5 dips
10	95% ethanol	30 seconds
11	100% ethanol	30 seconds
12	Air Dry	30 minutes
13	Mount slide with Cytoseal	NA

Supplemental Table 4-2: Proposed Assignment of Major Olefin Species Detected. Summary table of the major m/z species detected in mouse brain sections, their proposed assignment, mass error in PPM, and major m/z fragments detected. Species whose identification is not known are marked "unknown," whereas those whose lipid class could be determined but not fully identified are marked by their class name. Previous literature or online database confirming the identification is also cited.

Exp. *m/z*	Calc. *m/z*	Error (PPM)	Proposed Assignment	Major Fragment(s)	Molecular Formula	Reference
250.8	NA	NA	Unknown	231, 221, 207, 178, 165, 139, 109, 107	NA	NA
292.8	NA	NA	Unknown	287, 273, 233, 140, 109, 107, 86	NA	NA
294.8	NA	NA	Unknown	289, 275, 233, 140, 109, 107, 86	NA	NA
322.7	322.714	19	Ag_3	107, 109	Ag3	NA
338.7	338.709	3	Ag_3O	107, 109	Ag3O	NA
345.1	NA	NA	Unknown	317, 301, 109, 107, 86	NA	NA
387.2	387.145	13	Linoleic acid	369, 343	$C_{18}H_{30}O_2$	Dufresne *et al.*[146]
389.2	389.160	0	Oleic acid	371, 344	$C_{18}H_{34}O_2$	Dufresne *et al.*[146]
411.2	411.145	12	Arachidonic acid	411, 393, 365, 297, 274, 257	$C_{20}H_{32}O_2$	Dufresne *et al.*[146]
430.2	430.187	7	Linoleoyl Ethanolamide	411, 401, 373, 275, 242	$C_{20}H_{37}NO_4$	LipidMaps
435.1	435.145	11	Docosahexaenoic acid	417, 391, 299, 258, 255, 215	$C_{22}H_{22}O_2$	Dufresne *et al.*[146]
439.2	439.176	9	Docosatetraenoic acid	421,395,367,341,222	$C_{22}H_{36}O_2$	Dufresne *et al.*[146]
443.3	0.000	NA	Fatty Acid	425, 393, 333, 287, 107	NA	NA
461.2	0.000	NA	Fatty Acid	444, 416, 389, 347, 325, 244	NA	NA
493.3	493.259	2	Cholesterol	493, 475, 437, 367, 247	$C_{27}H_{46}O$	Dufresne *et al.*[146]
507.2	NA	NA	Unknown	433, 323, 261, 219, 163, 125, 86	NA	NA

509.3	NA	NA	Unknown	323, 290, 243, 163, 125, 86	NA	NA
538.5	538.524	11	Ag_5	107, 109	Ag_5	NA
672.5	0.000	NA	Cer (36:1)	654, 626, 624, 564, 457, 285, 287, 163	$C_{27}H_{44}O_2$	LipidMaps
906.5	0.000	NA	Unknown	713, 569, 417, 264, 157, 86	NA	LipidMaps
934.6	0.000	NA	Fatty Acid	916, 772, 754, 570, 445, 280, 264	NA	NA

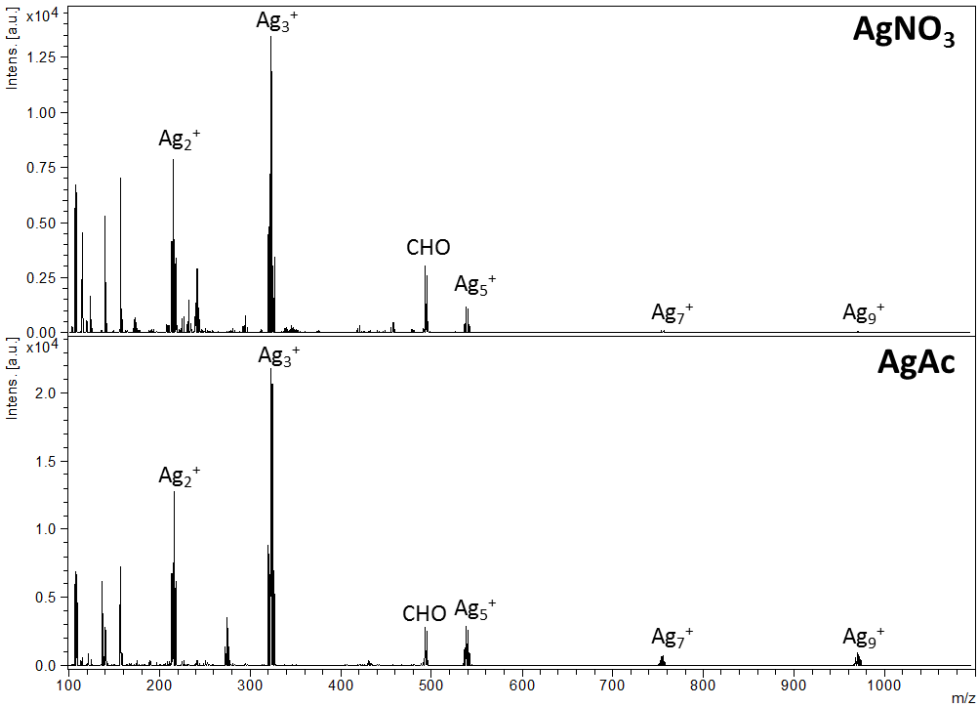

Supplemental Figure 4-1: Spectral Comparison of Silver Salts Spotted on a Mouse Brain Tissue Section. Representative positive reflectron mode mass spectra (200 shots per spectrum) from the white matter of a mouse brain obtained after spotting 1 µL of silver nitrate (AgNO3) or 1 µL of silver acetate (AgAc) on the white matter of the brain. The spectra are highly similar in terms of the cholesterol (CHO) signal intensity and overall spectral features. The AgNO3 spectrum displayed greater number of species in the lower mass range, suggesting it to be more sensitive and slightly more effective than AgAc.

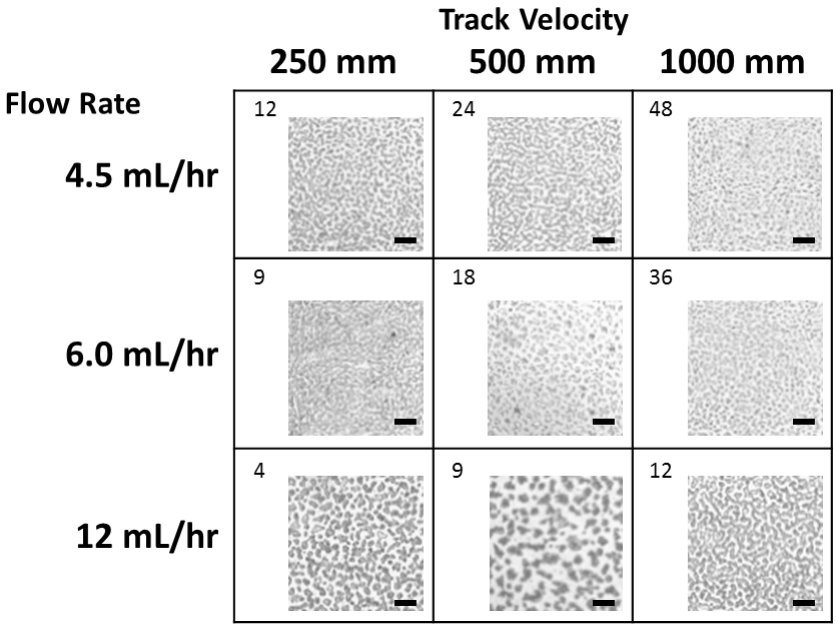

Supplemental Figure 4-2: The Effects of Flow Rate and Track Spacing on $AgNO_3$ Crystal Size. Optical comparisons of different combinations of flow rate and velocity demonstrated a clear increase in crystal size as the flow rate increases (by column) and a slight decrease in crystal size as the velocity increases (by row). The number of passes for each flow rate and track spacing (indicated on the top left of each cell) were modified such that the same amount of $AgNO_3$ was deposited per scare unit. All remaining parameters were kept constant as follows: 8.5 mg/mL solution of $AgNO_3$ in 100% MeOH, 4 mm track spacing, 45°C nozzle temperature and 20 psi spray pressure. Images were obtained from a conventional light microscope at 40x enlargement without further digital zoom. Scale bars represent 100 μm.

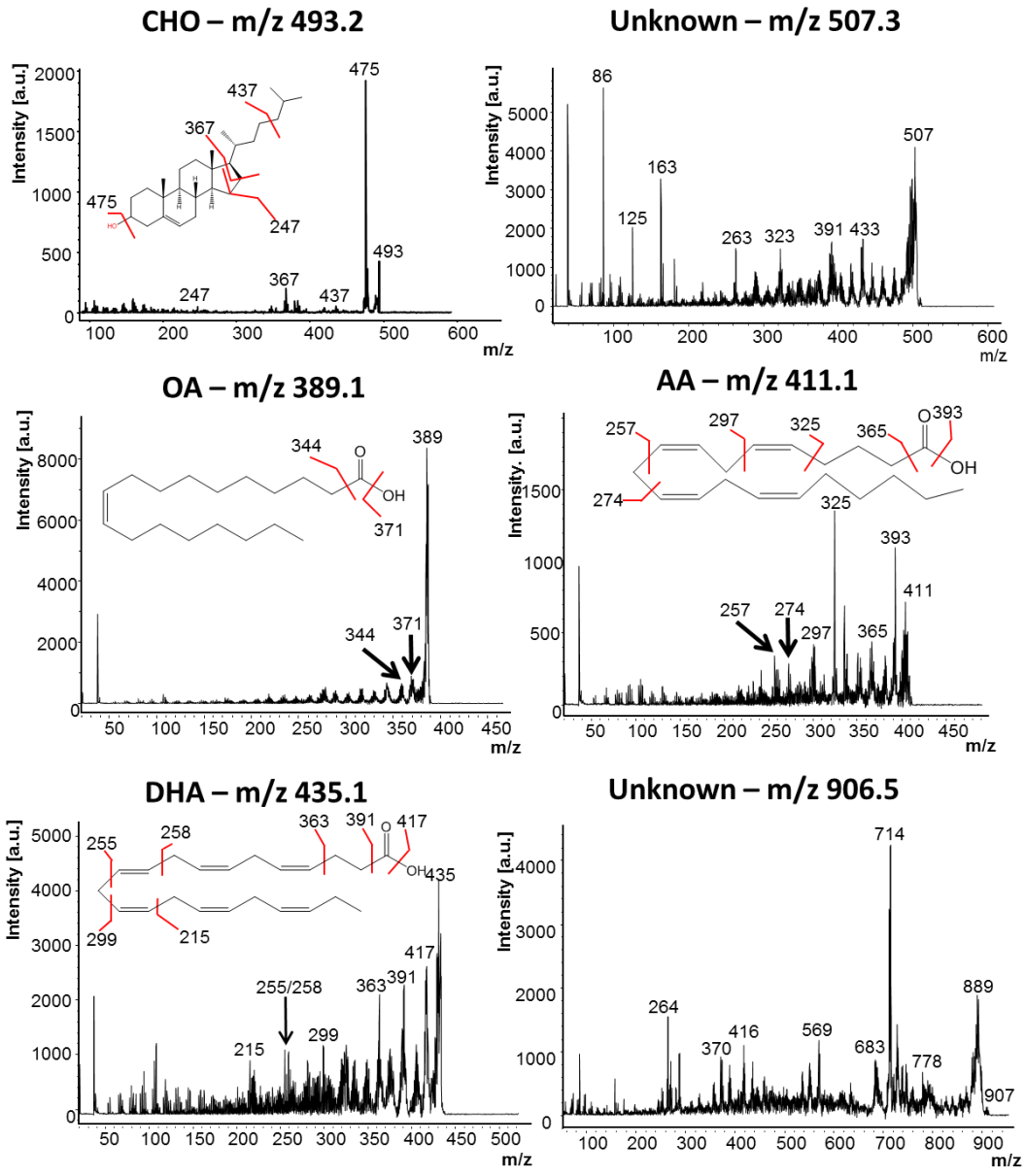

Supplemental Figure 4-3: Representative MS/MS Results of Select Olefins and Other Species. On-tissue MS/MS of select olefins and their proposed fragmentation pathways with fragment pics indicated. The results shown were confirmed with previous literature, particularly, Dufresne *et al*., 2013[146]. MS/MS of two unknowns that were shown in Figure 3 and Figure 4 are highlighted here

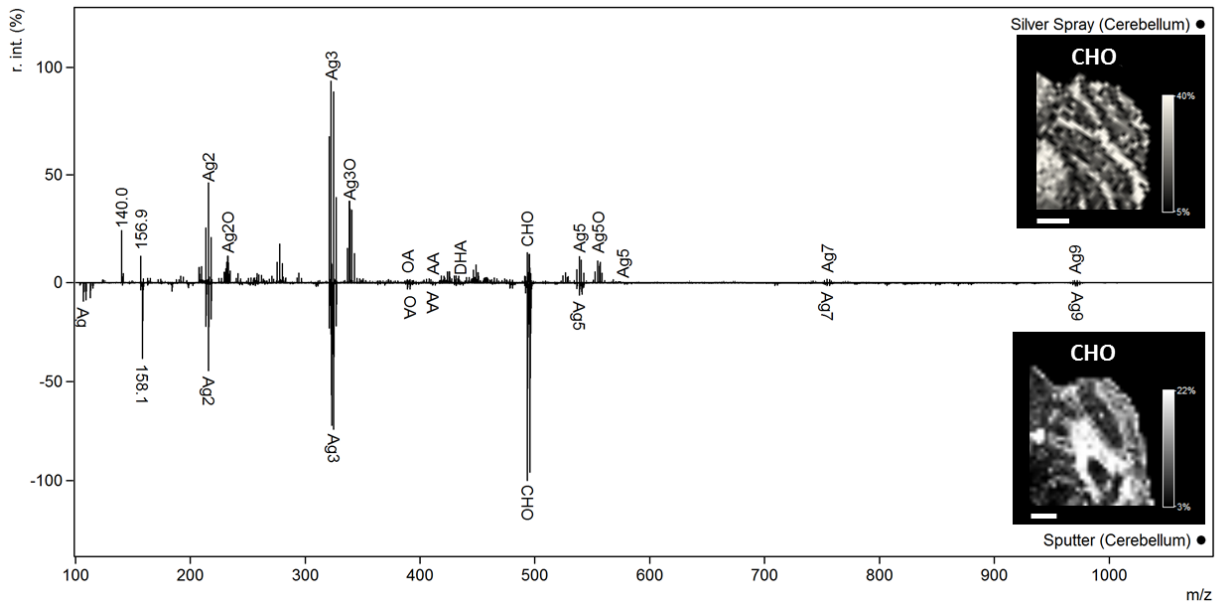

Supplemental Figure 4-4: Spectral and Image Comparison of $AgNO_3$ Spray vs Silver Sputtering of the Mouse Cerebellum. Mean spectra of the cerebellum region from a half brain section after AgNO3 spray deposition (top spectrum) and silver sputtering (bottom spectrum) show similar species detected. The major difference is the presence of oxidized silver clusters after spray deposition and greater relative intensity for arachidonic acid (AA) and oleic acid (OA) after sputter deposition. Lower mass species uniquely observed after spray or sputter deposition are labeled. The IMS results for cholesterol (CHO) from the cerebellum brain region is shown at the right of each spectrum. The sputtering results were obtained from a section at a lower Bregma than that of the spray result, leading to the difference seen in CHO distribution. Scale bars indicate 1 mm.

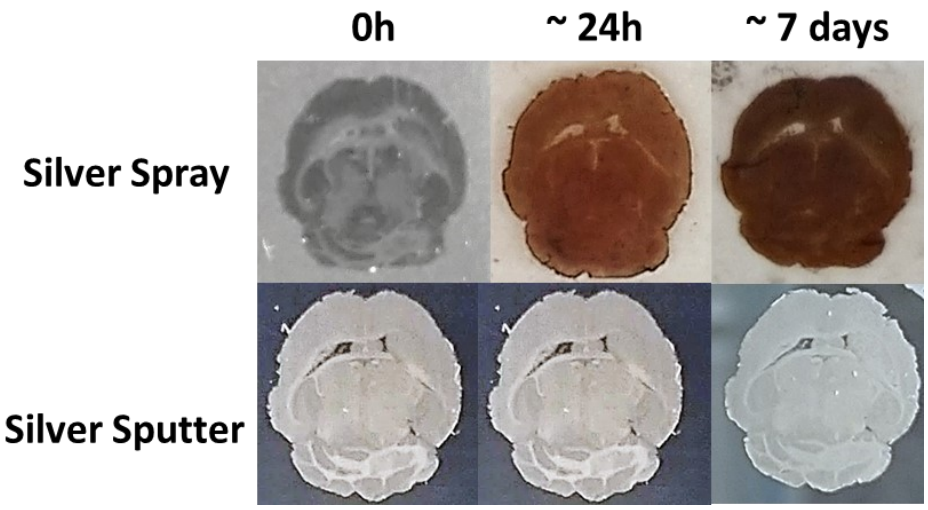

Supplemental Figure 4-5: Visual Horizontal Mouse Brain Section Comparison After Silver Spray and Sputter Deposition. Silver sprayed samples exposed to ambient light after more than 24 h turn from transparent to dark brown, indicative of oxidation (top row). UV light (including sunlight) expedites this oxidative process. Meanwhile, silver sputtered samples do not have obvious visual changes when left under ambient conditions for 24 hs, indicating that in this case oxidation takes longer time.

Chapter 5: Conclusion & Future Perspectives

5.1. Conclusion

Salts are undeniably essential to all known biological life. However, their natural presence in biological samples can be a nuisance for IMS analysis. This thesis provides three different methods to overcome this 'salty mess'.

Chapter 2 details a viable sample preparation protocol for overcoming challenges when working with salt-laden samples for lipidomic studies. Specifically, the chapter demonstrates that washing Malpighian fly tubules microdissected in PBS with 40% glycerol followed by 150 mM cold ammonium acetate removes the excess potassium and sodium salts and still allows for the detection of major phospholipid signals on-tissue. This study is the first of its kind to conduct lipidomic studies on microdissected samples after rigorous desalting washes, as previous studies of microdissected organs have been focused on protein IMS [229, 251, 253, 258]. The computability between traditional microdissection protocol and lipid IMS greatly enhances the possibility to obtain both lipid and protein profiles of organs and organisms not suitable for sectioning. This chapter also describes a dual-polarity IMS approach for phospholipid (PL) detection on whole *Drosophila* cryosections. While the protocol itself is not novel, this is the first set of experiments applying dual polarity IMS on an insect, an area of research with emerging interests in including this technique in future studies. It is also the first dual-polarity IMS conducted at 25 μm without oversampling, a marked improvement compared to the original dual-polarity IMS experiment at 50 μm[60], paving the way for high resolution dual-polarity IMS studies.

On the other hand, **Chapter 3** posits that doping samples with salt prior to matrix application can enhance the ionization of certain lipid species. Indeed, it was discovered that a thin layer of ammonium formate (AF) deposited onto mouse brain sections followed by DAN matrix deposition by sublimation led to an overall increase in ganglioside signals. Interestingly, desalting the sample

in 50 mM AF for 30 s prior to AF salt deposition and a 24-hour rest period in the freezer after AF salt and matrix deposition yielded the greatest overall enhancement. Compared to the standard IMS protocol noted in the literature, this combinatory protocol yielded an average 10-fold improvement in the total ganglioside signal and 3-fold increase in the number of ganglioside species detected. This level of sensitivity allowed for the detection of biologically relevant yet less abundant species such as GM2s and GM3s in normal mouse brain sections, giving us the ability to compare the healthy levels of these gangliosides against the diseased model. While Colsch *et al* reported similar success by spray-coating their sample with 2,6-dihydroxyacetphenon (2,6-DHA) doped with ammonium sulfate and heptafluorobutyric acid (HBFA)[281], their results appear to be limited in spatial resolution (80 μm) and time, as 2,6-DHA is still less stable than DAN in vacuum. Our sublimation-based approach can reach at least 20 μm of spatial resolution without detectable delocalization.

Finally, **Chapter 4** revealed that in some cases, salts alone are sufficient for conducting lipidomic IMS experiments. In this work, silver nitrate was tested for its ability to ionize cholesterol and other olefins on mouse brain tissue sections. The solvent system and various instrumental parameters were optimized to ensure a homogeneous and dry deposition to minimize species delocalization. This approach successfully discerned the spatial distribution of cholesterol and other common fatty acids on the mouse brain samples down to 5 μm. While some hot spots were still visible on the sample, the overall olefin signal quality was comparable to that obtained with a sputtered layer of silver. While one previous study has dismissed silver-based salts due to their inferiority in sensitivity compared to silver nanoparticles[145], this work has demonstrated that $AgNO_3$ can be successfully applied for IMS experiments as a low-cost and efficient alternative. The relative ease and high reproducibility not only cater to preliminary studies on cholesterol distribution on thin tissue sections but can also be considered for large scale studies where sample

preparation consistency is key. The study also highlights the robustness of automatic spray instruments and their growing importance in ensuring the reproducibility of sample preparation. This work also opens the door for further exploration of other metal salts that could also be directly spray deposited to introduce specificity for species less favoured by typical organic MALDI matrices.

Through these three different IMS workflows, this thesis highlights the complex influence of salts during the MALDI process. At times considered ion-suppressing contaminants, other times ionizing adducts, their interactions with the analytes and the matrix molecules demand careful consideration and methodical investigation prior to IMS experiments in order to maximize their contribution and minimize their suppression in the formation of analyte ions relevant to the biological question we seek to answer.

5.2. Future Perspectives

Over the past decade, IMS has become an integral part of biological studies, ranging from cancer research[47, 328, 329] to the drug discovery process[330, 331]. Much of this has been made possible through the development of sample preparation techniques and novel instrumentation that have increased the specificity and sensitivity for biomolecules that were traditionally less amenable to the MALDI process. These include the discovery of novel matrices[144, 164], the adaptation of chemical and enzymatic derivatization approaches[47, 169, 193, 332], as well as leaps in IMS instrumentation such as faster laser pulse rates[220], post-MALDI separation by ion mobility[333] and secondary laser ionization (MALDI-2)[213]. The contribution of this thesis lies in the development of novel sample preparation approaches to increase and improve the sensitivity and/or specificity for specific classes of lipids to answer associated biological questions. As such, the immediate next steps would be to validate these techniques with actual biological studies. For Malpighian tubules,

a feasible study would be to compare the phospholipid profiles of wild-type tubules against transgenic ones. For the enhanced ganglioside method, it would be interesting to apply this technique to understand changes in ganglioside distribution as a function of a neurodegenerative disease, such as Alzheimer's. The silver salt spray protocol is ready for large scale studies and can be used to compare the relative quantitative difference in cholesterol of disease or transgenic models. Clearly, tweaks and slight modifications may be required depending on sample type and instrumental status. Nonetheless, the goal is to affirm these techniques as extremely robust and reproducible, a crucial aspect of quality MALDI IMS.

Besides the biological applications, it would be interesting to examine the underlying factors at play. Despite clear benefits derived from desalting and/or salt doping, the molecular mechanisms were not here fully explored. For example, what factors (concentration, pH, temperature, duration, etc.) are driving the differences in the molecular profile and degree of delocalization observed on microdissected tubules subjected to varying desalting solutions? To what extent are these effects observed across various types of microdissected samples and/or thin-tissue sections? In the case of salt doping, what is the molecular interaction among the salt, the analytes, and the matrix molecules before and during the MALDI process? For metal-based salts, how do metal salts participate in the desorption or/and ionization process? How do their counterions affect the ionization efficiency of the target analytes? Perhaps, more interestingly, this thesis begs the question: what is it about ammonium-based salts that allow them to be beneficial both as a desalting solution and as a salt additive? A greater understanding of this interaction will not only help elucidate the elusive MALDI process, but also guide future IMS experiments towards a more rational approach when designing and optimizing sample preparation protocols.

References

1. Thomson, J. J., XL. Cathode Rays. *Lond. Edinb. Dubl. Phil. Mag.* **1897,** *44* (269), 293-316.

2. Griffiths, J., A Brief History of Mass Spectrometry. *Anal. Chem.* **2008,** *80* (15), 5678-5683.

3. Bleakney, W., A New Method of Positive Ray Analysis and Its Application to the Measurement of Ionization Potentials in Mercury Vapor. *Phys. Rev.* **1929,** *34* (1), 157-160.

4. Eckenrode, B. A.; McLuckey, S. A.; Glish, G. L., Comparison of electron ionization and chemical ionization sensitivities in an ion trap mass spectrometer. *Int. J. Mass Spectrom. Ion Processes* **1991,** *106*, 137-157.

5. Dempster, A. J., A new Method of Positive Ray Analysis. *Phys. Rev.* **1918,** *11* (4), 316-325.

6. Munson, M. S. B.; Field, F. H., Chemical Ionization Mass Spectrometry. I. General Introduction. *J. Am. Chem. Soc.* **1966,** *88* (12), 2621-2630.

7. Wilschefski, S. C.; Baxter, M. R., Inductively Coupled Plasma Mass Spectrometry: Introduction to Analytical Aspects. *Clin. Biochem. Rev* **2019,** *40* (3), 115-133.

8. Houk, R. S.; Fassel, V. A.; Flesch, G. D.; Svec, H. J.; Gray, A. L.; Taylor, C. E., Inductively coupled argon plasma as an ion source for mass spectrometric determination of trace elements. *Anal. Chem.* **1980,** *52* (14), 2283-2289.

9. Yamashita, M.; Fenn, J. B., Electrospray ion source. Another variation on the free-jet theme. *J. Phys. Chem.* **1984,** *88* (20), 4451-4459.

10. Karas, M.; Hillenkamp, F., Laser desorption ionization of proteins with molecular masses exceeding 10,000 daltons. *Anal. Chem.* **1988,** *60* (20), 2299-2301.

11. Nadler, W. M.; Waidelich, D.; Kerner, A.; Hanke, S.; Berg, R.; Trumpp, A.; Rösli, C., MALDI versus ESI: The Impact of the Ion Source on Peptide Identification. *J. Proteome Res.* **2017,** *16* (3), 1207-1215.

12. Nier, A. O., A Mass Spectrometer for Routine Isotope Abundance Measurements. *Rev. Sci. Instrum.* **1940,** *11* (7), 212-216.

13. Nier, A. O., A Mass Spectrometer for Isotope and Gas Analysis. *Rev. Sci. Instrum.* **1947,** *18* (6), 398-411.

14. Paul, W.; Steinwedel, H., Notizen: Ein neues Massenspektrometer ohne Magnetfeld. *Z. Naturforsch. A* **1953,** *8*, 448.

15. Morrison, J. D., Personal reminiscences of forty years of mass spectrometry in Australia. *Org. Mass Spec.* **1991,** *26* (4), 183-194.

16. Yost, R. A.; Enke, C. G., Selected ion fragmentation with a tandem quadrupole mass spectrometer. *J. Am. Chem. Soc.* **1978,** *100* (7), 2274-2275.

17. Blaum, K., High-accuracy mass spectrometry with stored ions. *Phys. Rep.* **2006,** *425* (1), 1-78.

18. Hu, Q.; Noll, R. J.; Li, H.; Makarov, A.; Hardman, M.; Graham Cooks, R., The Orbitrap: a new mass spectrometer. *Journal of Mass Spectrometry* **2005,** *40* (4), 430-443.

19. Park, J.; Aksamija, Z.; Shin, H.-C.; Kim, H.; Blick, R. H., Phonon-Assisted Field Emission in Silicon Nanomembranes for Time-of-Flight Mass Spectrometry of Proteins. *Nano Lett.* **2013,** *13* (6), 2698-2703.

20. Wolff, M. M.; Stephens, W. E., A Pulsed Mass Spectrometer with Time Dispersion. *Rev. Sci. Instrum.* **1953,** *24* (8), 616-617.

21. Ewing, R. G.; Atkinson, D. A.; Eiceman, G. A.; Ewing, G. J., A critical review of ion mobility spectrometry for the detection of explosives and explosive related compounds. *Talanta* **2001,** *54* (3), 515-529.

22. Sogawa, K.; Watanabe, M.; Sato, K.; Segawa, S.; Ishii, C.; Miyabe, A.; Murata, S.; Saito, T.; Nomura, F., Use of the MALDI BioTyper system with MALDI–TOF mass spectrometry for rapid identification of microorganisms. *Anal. Bioanal. Chem.* **2011,** *400* (7), 1905.

23. Pusch, W., Bruker Daltonics: leading the way from basic research to mass-spectrometry-based clinical applications. *Pharmacogenomics* **2007,** *8* (6), 663-668.

24. Thevis, M.; Schänzer, W., Mass spectrometry in sports drug testing: Structure characterization and analytical assays. *Mass Spectrom Rev.* **2007,** *26* (1), 79-107.

25. Bartelink, E. J.; Chesson, L. A., Recent applications of isotope analysis to forensic anthropology. *Forensic Sci. Res.* **2019,** *4* (1), 29-44.

26. Olshina, M. A.; Sharon, M., Mass spectrometry: a technique of many faces. *Q. Rev. Biophys.* **2016,** *49*, e18.

27. Armenian, P.; Vo, K. T.; Barr-Walker, J.; Lynch, K. L., Fentanyl, fentanyl analogs and novel synthetic opioids: A comprehensive review. *Neuropharmacology* **2018,** *134*, 121-132.

28. Vandergrift, G. W.; Gill, C. G., Paper spray mass spectrometry: A new drug checking tool for harm reduction in the opioid overdose crisis. *Journal of Mass Spectrometry* **2019,** *54* (9), 729-737.

29. Selliez, L.; Maillard, J.; Cherville, B.; Gautier, T.; Thirkell, L.; Gaubicher, B.; Schmitz-Afonso, I.; Afonso, C.; Briois, C.; Carrasco, N., High-resolution mass spectrometry for future space missions: Comparative analysis of complex organic matter with LAb-CosmOrbitrap and laser desorption/ionization Fourier transform ion cyclotron resonance. *Radid Commun. Mass Sp.* **2020,** *34* (10), e8645.

30. Meiring, H. D.; van der Heeft, E.; ten Hove, G. J.; de Jong, A. P. J. M., Nanoscale LC–MS(n): technical design and applications to peptide and protein analysis. *J. Sep. Sci.* **2002,** *25* (9), 557-568.

31. Jorgenson, J. W.; Lukacs, K. D., Zone electrophoresis in open-tubular glass capillaries. *Anal. Chem.* **1981,** *53* (8), 1298-1302.

32. McDaniel, E. W.; Martin, D. W.; Barnes, W. S., Drift Tube ‐ Mass Spectrometer for Studies of Low ‐ Energy Ion ‐ Molecule Reactions. *Rev. Sci. Instrum.* **1962,** *33* (1), 2-7.

33. Kanu, A. B.; Dwivedi, P.; Tam, M.; Matz, L.; Hill Jr., H. H., Ion mobility–mass spectrometry. *Journal of Mass Spectrometry* **2008,** *43* (1), 1-22.

34. Barber, M.; Bordoli, R. S.; Sedgwick, R. D.; Tetler, L. W., Fast atom bombardment mass spectrometry of two isomeric tripeptides. *Journal of Mass Spectrometry* **1981,** *16* (6), 256-260.

35. Castaing, R.; Slodzian, G., Microanalyse par émission ionique secondaire. *J. Microsc* **1962,** *1* (395), I960.

36. Mumma, R. O.; Vastola, F. J., Analysis of organic salts by laser ionization mass spectrometry. Sulfonates, sulfates and thiosulfates. *Org. Mass Spec.* **1972,** *6* (12), 1373-1376.

37. Tabet, J. C.; Cotter, R. J., Laser desorption time-of-flight mass spectrometry of high mass molecules. *Anal. Chem.* **1984,** *56* (9), 1662-1667.

38. Posthumus, M. A.; Kistemaker, P. G.; Meuzelaar, H. L. C.; Ten Noever de Brauw, M. C., Laser desorption-mass spectrometry of polar nonvolatile bio-organic molecules. *Anal. Chem.* **1978,** *50* (7), 985-991.

39. Hercules, D. M.; Day, R. J.; Balasanmugam, K.; Dang, T. A.; Li, C. P., Laser Microprobe Mass Spectrometry 2. Applications to Structural Analysis. *Anal. Chem.* **1982,** *54* (2), 280A-305A.

40. van Breemen, R. B.; Tabet, J.-C.; Cotter, R. J., Characterization of oxygen-linked glucuronides by laser desorption mass spectrometry. *Biomed. Mass Spec.* **1984,** *11* (6), 278-283.

41. Tanaka, K.; Waki, H.; Ido, Y.; Akita, S.; Yoshida, Y.; Yoshida, T.; Matsuo, T., Protein and polymer analyses up to m/z 100 000 by laser ionization time-of-flight mass spectrometry. *Radid Commun. Mass Sp.* **1988,** *2* (8), 151-153.

42. Jackson, S. N.; Wang, H.-Y. J.; Woods, A. S.; Ugarov, M.; Egan, T.; Schultz, J. A., Direct tissue analysis of phospholipids in rat brain using MALDI-TOFMS and MALDI-ion mobility-TOFMS. *J. Am. Soc. Mass. Spectrom.* **2005,** *16* (2), 133-138.

43. Sparvero, L. J.; Amoscato, A. A.; Dixon, C. E.; Long, J. B.; Kochanek, P. M.; Pitt, B. R.; Bayır, H.; Kagan, V. E., Mapping of phospholipids by MALDI imaging (MALDI-MSI): realities and expectations. *Chem. Phys. Lipids* **2012,** *165* (5), 545-562.

44. Gogichaeva, N. V.; Williams, T.; Alterman, M. A., MALDI TOF/TOF tandem mass

spectrometry as a new tool for amino acid analysis. *J. Am. Soc. Mass. Spectrom.* **2007,** *18* (2), 279-284.

45. Alterman, M. A.; Gogichayeva, N. V.; Kornilayev, B. A., Matrix-assisted laser desorption/ionization time-of-flight mass spectrometry-based amino acid analysis. *Anal. Biochem.* **2004,** *335* (2), 184-191.

46. Liang, J.-R.; Ai, X.-X.; Gao, Y.-H.; Chen, C.-P., MALDI-TOF MS analysis of the extracellular polysaccharides released by the diatom Thalassiosira pseudonana. *J. Appl. Phycol.* **2013,** *25* (2), 477-484.

47. Drake, R. R.; Powers, T. W.; Jones, E. E.; Bruner, E.; Mehta, A. S.; Angel, P. M., Chapter Four - MALDI Mass Spectrometry Imaging of N-Linked Glycans in Cancer Tissues. In *Advances in Cancer Research*, Drake, R. R.; McDonnell, L. A., Eds. Academic Press: 2017; Vol. 134, pp 85-116.

48. Cui, Z.; Theruvathu, J. A.; Farrel, A.; Burdzy, A.; Sowers, L. C., Characterization of synthetic oligonucleotides containing biologically important modified bases by matrix-assisted laser desorption/ionization time-of-flight mass spectrometry. *Anal. Biochem.* **2008,** *379* (2), 196-207.

49. Zagorevskii, D. V.; Aldersley, M. F.; Ferris, J. P., MALDI Analysis of Oligonucleotides Directly from Montmorillonite. *J. Am. Soc. Mass. Spectrom.* **2006,** *17* (9), 1265-1270.

50. Burkoth, A. K.; Anseth, K. S., MALDI-TOF Characterization of Highly Cross-Linked, Degradable Polymer Networks. *Macromolecules* **1999,** *32* (5), 1438-1444.

51. Montaudo, G.; Samperi, F.; Montaudo, M. S., Characterization of synthetic polymers by MALDI-MS. *Prog. Polym. Sci.* **2006,** *31* (3), 277-357.

52. Calderaro, A.; Arcangeletti, M. C.; Rodighiero, I.; Buttrini, M.; Montecchini, S.; Vasile Simone, R.; Medici, M. C.; Chezzi, C.; De Conto, F., Identification of different respiratory viruses, after a cell culture step, by matrix assisted laser desorption/ionization time of flight mass spectrometry (MALDI-TOF MS). *Sci. Rep.* **2016,** *6* (1), 36082.

53. Xiu, L.; Zhang, C.; Wu, Z.; Peng, J., Establishment and Application of a Universal Coronavirus Screening Method Using MALDI-TOF Mass Spectrometry. *Front. Microbiol.* **2017,** *8* (1510).

54. Holle, A.; Haase, A.; Kayser, M.; Höhndorf, J., Optimizing UV laser focus profiles for improved MALDI performance. *Journal of Mass Spectrometry* **2006,** *41* (6), 705-716.

55. Beavis, R. C.; Chaudhary, T.; Chait, B. T., α-Cyano-4-hydroxycinnamic acid as a matrix for matrix assisted laser desorption mass spectromtry. *Org. Mass Spec.* **1992,** *27* (2), 156-158.

56. Strupat, K.; Kampmeier, J.; Horneffer, V., Investigations of 2,5-DHB and succinic acid as matrices for UV and IR MALDI. Part II: Crystallographic and mass spectrometric analysis. *Int. J. Mass Spectrom. Ion Processes* **1997,** *169-170*, 43-50.

57. Schiller, J.; Süß, R.; Fuchs, B.; Müller, M.; Petković, M.; Zschörnig, O.; Waschipky, H., The suitability of different DHB isomers as matrices for the MALDI-TOF MS analysis of phospholipids: which isomer for what purpose? *Eur. Biophys. J.* **2007,** *36* (4), 517-527.

58. Cohen, L. H.; Gusev, A. I., Small molecule analysis by MALDI mass spectrometry. *Anal. Bioanal. Chem.* **2002,** *373* (7), 571-586.

59. Beavis, R. C.; Bridson, J. N., Epitaxial protein inclusion in sinapic acid crystals. *J. Phys. D: Appl. Phys.* **1993,** *26* (3), 442-447.

60. Thomas, A.; Charbonneau, J. L.; Fournaise, E.; Chaurand, P., Sublimation of new matrix candidates for high spatial resolution imaging mass spectrometry of lipids: enhanced information in both positive and negative polarities after 1,5-diaminonapthalene deposition. *Anal. Chem.* **2012,** *84* (4), 2048-54.

61. Leszyk, J. D., Evaluation of the new MALDI matrix 4-chloro-alpha-cyanocinnamic acid. *J. Biomol. Tech.* **2010,** *21* (2), 81-91.

62. Laugesen, S.; Roepstorff, P., Combination of two matrices results in improved performance of maldi ms for peptide mass mapping and protein analysis. *J. Am. Soc. Mass. Spectrom.* **2003,** *14* (9), 992-1002.

63. Vorm, O.; Roepstorff, P.; Mann, M., Improved Resolution and Very High Sensitivity in MALDI TOF of Matrix Surfaces Made by Fast Evaporation. *Anal. Chem.* **1994,** *66* (19), 3281-3287.

64. Kussmann, M.; Nordhoff, E.; Rahbek-Nielsen, H.; Haebel, S.; Rossel-Larsen, M.; Jakobsen, L.; Gobom, J.; Mirgorodskaya, E.; Kroll-Kristensen, A.; Palm ‖ , L.; Roepstorff, P., Matrix-assisted Laser Desorption/Ionization Mass Spectrometry Sample Preparation Techniques Designed for Various Peptide and Protein Analytes. *Journal of Mass Spectrometry* **1997,** *32* (6), 593-601.

65. Xiang, F.; Beavis, R. C., Growing protein-doped sinapic acid crystals for laser desorption: An alternative preparation method for difficult samples. *Org. Mass Spec.* **1993,** *28* (12), 1424-1429.

66. Garcia, B. A.; Heaney, P. J.; Tang, K., Improvement of the MALDI-TOF Analysis of DNA with Thin-Layer Matrix Preparation. *Anal. Chem.* **2002,** *74* (9), 2083-2091.

67. Keller, B. O.; Li, L., Three-Layer Matrix/Sample Preparation Method for MALDI MS Analysis of Low Nanomolar Protein Samples. *J. Am. Soc. Mass. Spectrom.* **2006,** *17* (6), 780-785.

68. Lehmann, E.; Knochenmuss, R.; Zenobi, R., Ionization mechanisms in matrix-assisted laser desorption/ionization mass spectrometry: contribution of pre-formed ions. *Radid Commun. Mass Sp.* **1997,** *11* (14), 1483-1492.

69. Zenobi, R.; Knochenmuss, R., Ion formation in MALDI mass spectrometry. *Mass Spectrom Rev.* **1998,** *17* (5), 337-366.

70. Karas, M.; Bachmann, D.; Bahr, U.; Hillenkamp, F., Matrix-assisted ultraviolet laser desorption of non-volatile compounds. *Int. J. Mass Spectrom. Ion Processes* **1987,** *78*, 53-68.

71. Bae, Y. J.; Shin, Y. S.; Moon, J. H.; Kim, M. S., Degree of Ionization in MALDI of Peptides: Thermal Explanation for the Gas-Phase Ion Formation. *J. Am. Soc. Mass. Spectrom.* **2012,** *23* (8), 1326-1335.

72. Jaskolla, T. W.; Karas, M., Compelling Evidence for Lucky Survivor and Gas Phase Protonation: The Unified MALDI Analyte Protonation Mechanism. *J. Am. Soc. Mass. Spectrom.* **2011,** *22* (6), 976-988.

73. Stephens, W. E., A pulsed mass spetrometer with time dispersion. *Phys. Rev.* **1946,** *69* (11-12), 691.

74. Cameron, A. E.; Jr., D. F. E., An Ion ``Velocitron''. *Rev. Sci. Instrum.* **1948,** *19* (9), 605-607.

75. Alihanov, S., G., A new impulse method of measuring ion masses. *J. Exp. Theor. Phys.* **1956,** *31*, 517.

76. Grix, R.; Kutscher, R.; Li, G.; Grüner, U.; Wollnik, H.; Matsuda, H., A time-of-flight mass analyzer with high resolving power. *Radid Commun. Mass Sp.* **1988,** *2* (5), 83-85.

77. Mamyrin, B. A., Laser assisted reflectron time-of-flight mass spectrometry. *Int. J. Mass Spectrom. Ion Processes* **1994,** *131*, 1-19.

78. Radionova, A.; Filippov, I.; Derrick, P. J., In pursuit of resolution in time-of-flight mass spectrometry: A historical perspective. *Mass Spectrom Rev.* **2016,** *35* (6), 738-757.

79. Weidmann, S.; Zenobi, R., High-Mass MALDI-MS Using Ion Conversion Dynode Detectors: Influence of the Conversion Voltage on Sensitivity and Spectral Quality. *J. Am. Soc. Mass. Spectrom.* **2014,** *25* (6), 950-954.

80. Kraeling, M. E. K.; Topping, V. D.; Belgrave, K. R.; Schlick, K.; Simanek, E.; Man, S.; Dadiboyena, S.; Patri, A. K.; Sprando, R. L.; Yourick, J. J., In Vitro Skin Penetration of Dendrimer Nanoparticles. *Appl. In Vitro Toxicol.* **2019,** *5* (3), 134-149.

81. Brown, R. S.; Lennon, J. J., Mass Resolution Improvement by Incorporation of Pulsed Ion Extraction in a Matrix-Assisted Laser Desorption/Ionization Linear Time-of-Flight Mass Spectrometer. *Anal. Chem.* **1995,** *67* (13), 1998-2003.

82. Vestal, M.; Juhasz, P., Resolution and mass accuracy in matrix-assisted laser desorption ionization- time-of-flight. *J. Am. Soc. Mass. Spectrom.* **1998,** *9* (9), 892-911.

83. Wiley, W. C.; McLaren, I. H., Time ‐ of ‐ Flight Mass Spectrometer with Improved Resolution. *Rev. Sci. Instrum.* **1955,** *26* (12), 1150-1157.

84. Bahr, U.; Stahl-Zeng, J.; Gleitsmann, E.; Karas, M., Delayed extraction time-of-flight

MALDI mass spectrometry of proteins above 25000 Da. *Journal of Mass Spectrometry* **1997,** *32* (10), 1111-1116.

85. Sukhdev, B.; Towers, M.; Murray, P.; Lareau, N.; Jarvis, S.; Caprioli, R. M.; Claude, E. In *A Novel Prototype MALDI Source on a OA-TOF Mass Spectrometer Combined with Ion Mobility Sepearation*, 66th ASMS Conference on Mass Spectrometry and Allied Topics, San Diego, CA, June 4, 2018; San Diego, CA, 2018.

86. Chernushevich, I. V.; Merenbloom, S. I.; Liu, S.; Bloomfield, N., A W-Geometry Ortho-TOF MS with High Resolution and Up to 100% Duty Cycle for MS/MS. *J. Am. Soc. Mass. Spectrom.* **2017,** *28* (10), 2143-2150.

87. Verentchikov, A. N.; Yavor, M.; Mitchell, J. C.; Artaev, V. Multi Reflecting Time-of-Flight Mass Spectrometer and A Method of Use. 2005.

88. Satoh, T.; Sato, T.; Tamura, J., Development of a high-Performance MALDI-TOF mass spectrometer utilizing a spiral ion trajectory. *J. Am. Soc. Mass. Spectrom.* **2007,** *18* (7), 1318-1323.

89. Eng, J. K.; McCormack, A. L.; Yates, J. R., An approach to correlate tandem mass spectral data of peptides with amino acid sequences in a protein database. *J. Am. Soc. Mass. Spectrom.* **1994,** *5* (11), 976-989.

90. Pappin, D. J. C.; Hojrup, P.; Bleasby, A. J., Rapid identification of proteins by peptide-mass fingerprinting. *Curr. Biol.* **1993,** *3* (6), 327-332.

91. Smith, C. A.; O'Maille, G.; Want, E. J.; Qin, C.; Trauger, S. A.; Brandon, T. R.; Custodio, D. E.; Abagyan, R.; Siuzdak, G., METLIN: A Metabolite Mass Spectral Database. *Ther. Drug Monit.* **2005,** *27* (6), 747-751.

92. Fahy, E.; Subramaniam, S.; Brown, H. A.; Glass, C. K.; Merrill, A. H., Jr.; Murphy, R. C.; Raetz, C. R.; Russell, D. W.; Seyama, Y.; Shaw, W.; Shimizu, T.; Spener, F.; van Meer, G.; VanNieuwenhze, M. S.; White, S. H.; Witztum, J. L.; Dennis, E. A., A comprehensive classification system for lipids. *J. Lipid Res.* **2005,** *46* (5), 839-61.

93. Fahy, E.; Sud, M.; Cotter, D.; Subramaniam, S., LIPID MAPS online tools for lipid research. *Nucleic Acids Res* **2007,** *35* (Web Server issue), W606-W612.

94. Yan, Y.; Ubukata, M.; Cody, R. B.; Holy, T. E.; Gross, M. L., High-Energy Collision-Induced Dissociation by MALDI TOF/TOF Causes Charge-Remote Fragmentation of Steroid Sulfates. *J. Am. Soc. Mass. Spectrom.* **2014,** *25* (8), 1404-1411.

95. Yergey, A. L.; Coorssen, J. R.; Backlund, P. S.; Blank, P. S.; Humphrey, G. A.; Zimmerberg, J.; Campbell, J. M.; Vestal, M. L., De novo sequencing of peptides using MALDI/TOF-TOF. *J. Am. Soc. Mass. Spectrom.* **2002,** *13* (7), 784-791.

96. Suckau, D.; Resemann, A.; Schuerenberg, M.; Hufnagel, P.; Franzen, J.; Holle, A., A novel MALDI LIFT-TOF/TOF mass spectrometer for proteomics. *Anal. Bioanal. Chem.* **2003,** *376* (7), 952-965.

97. Hsu, F.-F.; Turk, J., Electrospray ionization multiple-stage linear ion-trap mass spectrometry for structural elucidation of triacylglycerols: Assignment of fatty acyl groups on the glycerol backbone and location of double bonds. *J. Am. Soc. Mass. Spectrom.* **2010,** *21* (4), 657-669.

98. Burinsky, D. J.; Cooks, R. G.; Chess, E. K.; Gross, M. L., Consecutive reactions in triple analyzer mass spectrometry and applications to mixture analysis. *Anal. Chem.* **1982,** *54* (2), 295-299.

99. Chen, G.; Pramanik, B. N.; Bartner, P. L.; Saksena, A. K.; Gross, M. L., Multiple-stage mass spectrometric analysis of complex oligosaccharide antibiotics (everninomicins) in a quadrupole ion trap. *J. Am. Soc. Mass. Spectrom.* **2002,** *13* (11), 1313-1321.

100. Zeller, L. C.; Farrell, J. T.; Kenttämaa, H. I.; Kuivalainen, T., Multiple-stage mass spectrometry in structural characterization of organophosphorus compounds. *J. Am. Soc. Mass. Spectrom.* **1993,** *4* (2), 125-134.

101. Liebl, H., Ion Microprobe Mass Analyzer. *J. Appl. Phys.* **1967,** *38* (13), 5277-5283.

102. Takáts, Z.; Wiseman, J. M.; Gologan, B.; Cooks, R. G., Mass Spectrometry Sampling Under Ambient Conditions with Desorption Electrospray Ionization. *Science* **2004,** *306* (5695), 471-473.

103. Spengler, B.; Hubert, M.; Kaufmann, R. In *MALDI Ion Imaging and Biological Ion Imaging with a new Scanning UV-Laser Microprobe*, 42nd ASMS Conference on Mass Spectrometry and Allied Topics, Chicago, Illinois, June 2, 1994; Ross, M. M., Ed. Chicago, Illinois, 1994; p 1041.

104. Spengler, B.; Hubert, M., Scanning microprobe matrix-assisted laser desorption ionization (SMALDI) mass spectrometry: Instrumentation for sub-micrometer resolved LDI and MALDI surface analysis. *J. Am. Soc. Mass. Spectrom.* **2002,** *13* (6), 735-748.

105. Caprioli, R. M.; Farmer, T. B.; Gile, J., Molecular Imaging of Biological Samples: Localization of Peptides and Proteins Using MALDI-TOF MS. *Anal. Chem.* **1997,** *69* (23), 4751-4760.

106. Hochart, G.; Bonnel, D.; Stauber, J.; Stamatas, G. N., Biomarker Mapping on Skin Tape Strips Using MALDI Mass Spectrometry Imaging. *J. Am. Soc. Mass. Spectrom.* **2019,** *30* (10), 2082-2091.

107. Anderson, D. M. G.; Ablonczy, Z.; Koutalos, Y.; Spraggins, J.; Crouch, R. K.; Caprioli, R. M.; Schey, K. L., High Resolution MALDI Imaging Mass Spectrometry of Retinal Tissue Lipids. *J. Am. Soc. Mass. Spectrom.* **2014,** *25* (8), 1394-1403.

108. Han, J.; Permentier, H.; Bischoff, R.; Groothuis, G.; Casini, A.; Horvatovich, P., Imaging of protein distribution in tissues using mass spectrometry: An interdisciplinary challenge. *TrAC Trend. Anal. Chem.* **2019,** *112*, 13-28.

109. Chaurand, P.; Cornett, D. S.; Angel, P. M.; Caprioli, R. M., From Whole-body Sections Down to Cellular Level, Multiscale Imaging of Phospholipids by MALDI Mass Spectrometry. *Mol. Cell. Proteomics* **2011,** *10* (2), 11.

110. Stoeckli, M.; Chaurand, P.; Hallahan, D. E.; Caprioli, R. M., Imaging mass spectrometry: a new technology for the analysis of protein expression in mammalian tissues. *Nat. Med.* **2001,** *7* (4), 493-6.

111. Groseclose, M. R.; Massion, P. P.; Chaurand, P.; Caprioli, R. M., High-throughput proteomic analysis of formalin-fixed paraffin-embedded tissue microarrays using MALDI imaging mass spectrometry. *Proteomics* **2008,** *8* (18), 3715-3724.

112. Khatib-Shahidi, S.; Andersson, M.; Herman, J. L.; Gillespie, T. A.; Caprioli, R. M., Direct Molecular Analysis of Whole-Body Animal Tissue Sections by Imaging MALDI Mass Spectrometry. *Anal. Chem.* **2006,** *78* (18), 6448-6456.

113. Stoeckli, M.; Staab, D.; Schweitzer, A., Compound and metabolite distribution measured by MALDI mass spectrometric imaging in whole-body tissue sections. *Int. J. Mass Spectrom.* **2007,** *260* (2), 195-202.

114. Spraggins, J. M.; Rizzo, D. G.; Moore, J. L.; Rose, K. L.; Hammer, N. D.; Skaar, E. P.; Caprioli, R. M., MALDI FTICR IMS of Intact Proteins: Using Mass Accuracy to Link Protein Images with Proteomics Data. *J. Am. Soc. Mass. Spectrom.* **2015,** *26* (6), 974-985.

115. Chaurand, P.; Schwartz, S. A.; Caprioli, R. M., Imaging mass spectrometry: a new tool to investigate the spatial organization of peptides and proteins in mammalian tissue sections. *Curr. Opin. Chem. Biol.* **2002,** *6* (5), 676-81.

116. Todd, P. J.; Schaaff, T. G.; Chaurand, P.; Caprioli, R. M., Organic ion imaging of biological tissue with secondary ion mass spectrometry and matrix-assisted laser desorption/ionization. *Journal of Mass Spectrometry* **2001,** *36* (4), 355-369.

117. Barry, J. A.; Groseclose, M. R.; Robichaud, G.; Castellino, S.; Muddiman, D. C., Assessing drug and metabolite detection in liver tissue by UV-MALDI and IR-MALDESI mass spectrometry imaging coupled to FT-ICR MS. *Int. J. Mass Spectrom.* **2015,** *377*, 448-455.

118. Chaurand, P.; Schwartz, S. A.; Billheimer, D.; Xu, B. J.; Crecelius, A.; Caprioli, R. M., Integrating Histology and Imaging Mass Spectrometry. *Anal. Chem.* **2004,** *76* (4), 1145-1155.

119. Fuchs, B.; Schiller, J., Application of MALDI-TOF mass spectrometry in lipidomics. *Eur. J. Lipid Sci. Tech.* **2009,** *111* (1), 83-98.

120. Goto-Inoue, N.; Hayasaka, T.; Zaima, N.; Setou, M., Imaging mass spectrometry for lipidomics. *Biochim. Biophys. Acta Mol. Cell. Biol. Lipids* **2011,** *1811* (11), 961-969.

121. Touboul, D.; Kollmer, F.; Niehuis, E.; Brunelle, A.; Laprévote, O., Improvement of biological time-of-flight-secondary ion mass spectrometry imaging with a bismuth cluster ion source. *J. Am. Soc. Mass. Spectrom.* **2005,** *16* (10), 1608-1618.

122. Harvey, D. J., Matrix-assisted laser desorption/ionization mass spectrometry of sphingo- and glycosphingo-lipids. *Journal of Mass Spectrometry* **1995,** *30* (9), 1311-1324.

123. Harvey, D. J., Matrix-assisted laser desorption/ionization mass spectrometry of phospholipids. *Journal of Mass Spectrometry* **1995,** *30* (9), 1333-1346.

124. Estrada, R.; Yappert, M. C., Alternative approaches for the detection of various phospholipid classes by matrix-assisted laser desorption/ionization time-of-flight mass spectrometry. *Journal of Mass Spectrometry* **2004,** *39* (4), 412-422.

125. Petković, M.; Schiller, J.; Müller, M.; Benard, S.; Reichl, S.; Arnold, K.; Arnhold, J., Detection of Individual Phospholipids in Lipid Mixtures by Matrix-Assisted Laser Desorption/Ionization Time-of-Flight Mass Spectrometry: Phosphatidylcholine Prevents the Detection of Further Species. *Anal. Biochem.* **2001,** *289* (2), 202-216.

126. Hankin, J. A.; Barkley, R. M.; Murphy, R. C., Sublimation as a method of matrix application for mass spectrometric imaging. *J. Am. Soc. Mass. Spectrom.* **2007,** *18* (9), 1646-1652.

127. Gemperline, E.; Rawson, S.; Li, L., Optimization and Comparison of Multiple MALDI Matrix Application Methods for Small Molecule Mass Spectrometric Imaging. *Anal. Chem.* **2014,** *86* (20), 10030-10035.

128. Zhang, J.; Rector, J.; Lin, J. Q.; Young, J. H.; Sans, M.; Katta, N.; Giese, N.; Yu, W.; Nagi, C.; Suliburk, J.; Liu, J.; Bensussan, A.; DeHoog, R. J.; Garza, K. Y.; Ludolph, B.; Sorace, A. G.; Syed, A.; Zahedivash, A.; Milner, T. E.; Eberlin, L. S., Nondestructive tissue analysis for ex vivo and in vivo cancer diagnosis using a handheld mass spectrometry system. *Sci. Transl. Med.* **2017,** *9* (406), eaan3968.

129. Vickerman, J. C., Molecular imaging and depth profiling by mass spectrometry—SIMS, MALDI or DESI? *Analyst* **2011,** *136* (11), 2199-2217.

130. Singer, S. J.; Nicolson, G. L., The Fluid Mosaic Model of the Structure of Cell Membranes. *Science* **1972,** *175* (4023), 720-731.

131. Wymann, M. P.; Schneiter, R., Lipid signalling in disease. *Nat. Rev. Mol.* **2008,** *9* (2), 162-176.

132. Alamri, H.; Patterson, N. H.; Yang, E.; Zoroquiain, P.; Lazaris, A.; Chaurand, P.; Metrakos, P., Mapping the triglyceride distribution in NAFLD human liver by MALDI imaging mass spectrometry reveals molecular differences in micro and macro steatosis. *Anal. Bioanal. Chem.* **2019,** *411* (4), 885-894.

133. Semenkovich, C. F., Insulin resistance and atherosclerosis. *J. Clin. Invest.* **2006,** *116* (7), 1813-1822.

134. Ariga, T.; McDonald, M. P.; Robert, K. Y., Thematic Review Series: Sphingolipids. Role of ganglioside metabolism in the pathogenesis of Alzheimer's disease—a review. *J. Lipid Res.* **2008,** *49* (6), 1157-1175.

135. Di Paolo, G.; Kim, T.-W., Linking lipids to Alzheimer's disease: cholesterol and beyond. *Nat. Rev. Neurosci.* **2011,** *12* (5), 284-296.

136. Gómez-Muñoz, A., Ceramide 1-phosphate/ceramide, a switch between life and death. *Biochim Biophys Acta Biomembr* **2006,** *1758* (12), 2049-2056.

137. Baenke, F.; Peck, B.; Miess, H.; Schulze, A., Hooked on fat: the role of lipid synthesis in cancer metabolism and tumour development. *Dis. Model. Mech.* **2013,** *6* (6), 1353-1363.

138. Liu, X.; Wang, H.; Liang, X.; Roberts, M. S., Chapter 30 - Hepatic Metabolism in Liver Health and Disease. In *Liver Pathophysiology*, Muriel, P., Ed. Academic Press: Boston, 2017; pp 391-400.

139. Hara, T.; Kimura, I.; Inoue, D.; Ichimura, A.; Hirasawa, A., Free Fatty Acid Receptors and Their Role in Regulation of Energy Metabolism. In *Reviews of Physiology, Biochemistry and Pharmacology, Vol. 164*, Nilius, B.; Amara, S. G.; Lill, R.; Offermanns, S.; Gudermann, T.; Petersen, O. H.; Jahn, R., Eds. Springer International Publishing: Cham, 2013; pp 77-116.

140. Ayorinde, F. O.; Garvin, K.; Saeed, K., Determination of the fatty acid composition of saponified vegetable oils using matrix-assisted laser desorption/ionization time-of-flight mass spectrometry. *Radid Commun. Mass Sp.* **2000,** *14* (7), 608-615.

141. Shroff, R.; Svatoš, A., 1,8-Bis(dimethylamino)naphthalene: a novel superbasic matrix for matrix-assisted laser desorption/ionization time-of-flight mass spectrometric analysis of fatty acids. *Radid Commun. Mass Sp.* **2009,** *23* (15), 2380-2382.

142. Shroff, R.; Muck, A.; Svatoš, A., Analysis of low molecular weight acids by negative mode matrix-assisted laser desorption/ionization time-of-flight mass spectrometry. *Radid Commun. Mass Sp.* **2007,** *21* (20), 3295-3300.

143. Cerruti, C. D.; Benabdellah, F.; Laprévote, O.; Touboul, D.; Brunelle, A., MALDI Imaging and Structural Analysis of Rat Brain Lipid Negative Ions with 9-Aminoacridine Matrix. *Anal. Chem.* **2012,** *84* (5), 2164-2171.

144. Ibrahim, H.; Jurcic, K.; Wang, J. S. H.; Whitehead, S. N.; Yeung, K. K. C., 1,6-Diphenyl-1,3,5-hexatriene (DPH) as a Novel Matrix for MALDI MS Imaging of Fatty Acids, Phospholipids, and Sulfatides in Brain Tissues. *Anal. Chem.* **2017,** *89* (23), 12828-12836.

145. Guan, M.; Zhang, Z.; Li, S.; Liu, J. a.; Liu, L.; Yang, H.; Zhang, Y.; Wang, T.; Zhao, Z., Silver nanoparticles as matrix for MALDI FTICR MS profiling and imaging of diverse lipids in brain. *Talanta* **2018,** *179*, 624-631.

146. Dufresne, M.; Thomas, A.; Breault-Turcot, J.; Masson, J. F.; Chaurand, P., Silver-assisted laser desorption ionization for high spatial resolution imaging mass spectrometry of olefins from thin tissue sections. *Anal. Chem.* **2013,** *85* (6), 3318-24.

147. Simons, K.; Ikonen, E., How Cells Handle Cholesterol. *Science* **2000,** *290* (5497), 1721-1726.

148. Björkhem, I.; Meaney, S., Brain Cholesterol: Long Secret Life Behind a Barrier. *Arterioscler. Thromb. Vasc. Biol.* **2004,** *24* (5), 806-815.

149. Tosi, M. R.; Tugnoli, V., Cholesteryl esters in malignancy. *Clin. Chim. Acta* **2005,** *359* (1), 27-45.

150. Miller, W. L., Molecular Biology of Steroid Hormone Synthesis*. *Endocr. Rev.* **1988,** *9* (3), 295-318.

151. Javitt, N. B., Bile acid synthesis from cholesterol: regulatory and auxiliary pathways. *FASEB J.* **1994,** *8* (15), 1308-1311.

152. McNamara, D. J., Dietary cholesterol and atherosclerosis. *Biochim. Biophys. Acta Mol. Cell. Biol. Lipids* **2000,** *1529* (1), 310-320.

153. Ansell, B. J., Cholesterol, stroke risk, and stroke prevention. *Curr. Atheroscler. Rep.* **2000,** *2* (2), 92-96.

154. Radišauskas, R.; Kuzmickienė, I.; Milinavičienė, E.; Everatt, R., Hypertension, serum lipids and cancer risk: A review of epidemiological evidence. *Medicina* **2016,** *52* (2), 89-98.

155. Pacholski, M. L.; Cannon Jr., D. M.; Ewing, A. G.; Winograd, N., Static time-of-flight secondary ion mass spectrometry imaging of freeze-fractured, frozen-hydrated biological membranes. *Radid Commun. Mass Sp.* **1998,** *12* (18), 1232-1235.

156. Zemski Berry, K. A.; Hankin, J. A.; Barkley, R. M.; Spraggins, J. M.; Caprioli, R. M.; Murphy, R. C., MALDI Imaging of Lipid Biochemistry in Tissues by Mass Spectrometry. *Chem. Rev.* **2011,** *111* (10), 6491-6512.

157. Ostrowski, S. G.; Kurczy, M. E.; Roddy, T. P.; Winograd, N.; Ewing, A. G., Secondary Ion MS Imaging To Relatively Quantify Cholesterol in the Membranes of Individual Cells from Differentially Treated Populations. *Anal. Chem.* **2007,** *79* (10), 3554-3560.

158. Nygren, H.; Malmerg, P., Silver deposition on freeze-dried cells allows subcellular localization of cholesterol with imaging TOF-SIMS. *J. Microsc* **2004,** *215* (2), 156-161.

159. Dufresne, M.; Patterson, N. H.; Norris, J. L.; Caprioli, R. M., Combining Salt Doping and Matrix Sublimation for High Spatial Resolution MALDI Imaging Mass Spectrometry of Neutral Lipids. *Anal. Chem.* **2019,** *91* (20), 12928-12934.

160. Murphy, R. C.; Hankin, J. A.; Barkley, R. M., Imaging of lipid species by MALDI mass spectrometry. *J. Lipid Res.* **2009,** *50* (Supplement), S317-S322.

161. Helmkamp, G. M.; Harvey, M. S.; Wirtz, K. W. A.; van Deenen, L. L. M., Phospholipid exchange between membranes. Purification of bovine brain proteins that preferentially catalyze the transfer of phosphatidylinositol. *J Biol Chem.* **1974,** *249* (20), 6382-6389.

162. Vitrac, H.; MacLean, D. M.; Jayaraman, V.; Bogdanov, M.; Dowhan, W., Dynamic

membrane protein topological switching upon changes in phospholipid environment. *Proc Natl Acad Sci U S A.* **2015,** *112* (45), 13874-13879.

163. Dowhan, W., Understanding phospholipid function: Why are there so many lipids? *J Biol Chem.* **2017,** *292* (26), 10755-10766.

164. Li, B.; Sun, R.; Gordon, A.; Ge, J.; Zhang, Y.; Li, P.; Yang, H., 3-Aminophthalhydrazide (Luminol) As a Matrix for Dual-Polarity MALDI MS Imaging. *Anal. Chem.* **2019,** *91* (13), 8221-8228.

165. Yang, E.; Gamberi, C.; Chaurand, P., Mapping the fly Malpighian tubule lipidome by imaging mass spectrometry. *Journal of Mass Spectrometry* **2019,** *54* (6), 557-566.

166. Kaya, I.; Brinet, D.; Michno, W.; Başkurt, M.; Zetterberg, H.; Blenow, K.; Hanrieder, J., Novel Trimodal MALDI Imaging Mass Spectrometry (IMS3) at 10 μm Reveals Spatial Lipid and Peptide Correlates Implicated in Aβ Plaque Pathology in Alzheimer's Disease. *ACS Chem. Neurosci.* **2017,** *8* (12), 2778-2790.

167. Pi, J.; Wu, X.; Feng, Y., Fragmentation patterns of five types of phospholipids by ultra-high-performance liquid chromatography electrospray ionization quadrupole time-of-flight tandem mass spectrometry. *Anal. Methods* **2016,** *8* (6), 1319-1332.

168. Kuo, T.-H.; Chung, H.-H.; Chang, H.-Y.; Lin, C.-W.; Wang, M.-Y.; Shen, T.-L.; Hsu, C.-C., Deep Lipidomics and Molecular Imaging of Unsaturated Lipid Isomers: A Universal Strategy Initiated by mCPBA Epoxidation. *Anal. Chem.* **2019,** *91* (18), 11905-11915.

169. Bednařík, A.; Bölsker, S.; Soltwisch, J.; Dreisewerd, K., An On-Tissue Paternò–Büchi Reaction for Localization of Carbon–Carbon Double Bonds in Phospholipids and Glycolipids by Matrix-Assisted Laser-Desorption–Ionization Mass-Spectrometry Imaging. *Angew. Chem. Int. Ed. Engl.* **2018,** *57* (37), 12092-12096.

170. Zaima, N.; Goto-Inoue, N.; Hayasaka, T.; Setou, M., Application of imaging mass spectrometry for the analysis of Oryza sativa rice. *Radid Commun. Mass Sp.* **2010,** *24* (18), 2723-2729.

171. Horn, P. J.; Korte, A. R.; Neogi, P. B.; Love, E.; Fuchs, J.; Strupat, K.; Borisjuk, L.; Shulaev, V.; Lee, Y.-J.; Chapman, K. D., Spatial Mapping of Lipids at Cellular Resolution in Embryos of Cotton. *Plant Cell* **2012,** *24* (2), 622-636.

172. Khalil, S. M.; Römpp, A.; Pretzel, J.; Becker, K.; Spengler, B., Phospholipid Topography of Whole-Body Sections of the Anopheles stephensi Mosquito, Characterized by High-Resolution Atmospheric-Pressure Scanning Microprobe Matrix-Assisted Laser Desorption/Ionization Mass Spectrometry Imaging. *Anal. Chem.* **2015,** *87* (22), 11309-11316.

173. Urban, P. L.; Chang, C.-H.; Wu, J.-T.; Chen, Y.-C., Microscale MALDI Imaging of Outer-Layer Lipids in Intact Egg Chambers from Drosophila melanogaster. *Anal. Chem.* **2011,** *83* (10), 3918-3925.

174. Bier, E., Drosophila, the golden bug, emerges as a tool for human genetics. *Nat. Rev. Genet.* **2005,** *6*, 9.

175. Chien, S.; Reiter, L. T.; Bier, E.; Gribskov, M., Homophila: human disease gene cognates in Drosophila. *Nucleic Acids Res* **2002,** *30* (1), 149-51.

176. Gamberi, C.; Hipfner, D. R.; Trudel, M.; Lubell, W. D., Bicaudal C mutation causes myc and TOR pathway up-regulation and polycystic kidney disease-like phenotypes in Drosophila. *PLoS Genet.* **2017,** *13* (4), e1006694.

177. Piper, M. D. W.; Skorupa, D.; Partridge, L., Diet, metabolism and lifespan in Drosophila. *Exp. Hematol.* **2005,** *40* (11), 857-862.

178. Pandey, U. B.; Nichols, C. D., Human Disease Models in Drosophila melanogaster and the Role of the Fly in Therapeutic Drug Discovery. *Pharmacol. Rev.* **2011,** *63* (2), 411-436.

179. Niehoff, A.-C.; Kettling, H.; Pirkl, A.; Chiang, Y. N.; Dreisewerd, K.; Yew, J. Y., Analysis of Drosophila Lipids by Matrix-Assisted Laser Desorption/Ionization Mass Spectrometric Imaging. *Anal. Chem.* **2014,** *86* (22), 11086-11092.

180. Khalil, S. M.; Pretzel, J.; Becker, K.; Spengler, B., High-resolution AP-SMALDI mass spectrometry imaging of Drosophila melanogaster. *Int. J. Mass Spectrom.* **2017,** *416*, 1-19.

181. Svennerholm, L., The gangliosides. *J. Lipid Res.* **1964,** *5* (2), 145-155.

182. Sonnino, S.; Mauri, L.; Chigorno, V.; Prinetti, A., Gangliosides as components of lipid membrane domains. *Glycobiology* **2007,** *17* (1), 1R-13R.

183. Cavdarli, S.; Groux-Degroote, S.; Delannoy, P., Gangliosides: The Double-Edge Sword of Neuro-Ectodermal Derived Tumors. *Biomolecules* **2019,** *9* (8), 311.

184. Schnaar, R. L.; Gerardy-Schahn, R.; Hildebrandt, H., Sialic Acids in the Brain: Gangliosides and Polysialic Acid in Nervous System Development, Stability, Disease, and Regeneration. *Physiol. Rev.* **2014,** *94* (2), 461-518.

185. Schneider, J. S.; Sendek, S.; Daskalakis, C.; Cambi, F., GM1 ganglioside in Parkinson's disease: Results of a five year open study. *J. Neurol. Sci.* **2010,** *292* (1-2), 45-51.

186. Caughlin, S.; Hepburn, J. D.; Park, D. H.; Jurcic, K.; Yeung, K. K. C.; Cechetto, D. F.; Whitehead, S. N., Increased Expression of Simple Ganglioside Species GM2 and GM3 Detected by MALDI Imaging Mass Spectrometry in a Combined Rat Model of Aβ Toxicity and Stroke. *PLoS One* **2015,** *10* (6), e0130364.

187. Svennerholm, L., Gangliosides -- A new therapeutic agent against stroke and Alzheimer's disease. *Life Sci.* **1994,** *55* (25), 2125-2134.

188. Lee, D.; Cha, S., 5-Methoxysalicylic Acid Matrix for Ganglioside Analysis with Matrix-Assisted Laser Desorption/Ionization Mass Spectrometry. *J. Am. Soc. Mass. Spectrom.* **2015,** *26*

(3), 522-525.

189. Zhang, Y.; Wang, J.; Liu, J. a.; Han, J.; Xiong, S.; Yong, W.; Zhao, Z., Combination of ESI and MALDI mass spectrometry for qualitative, semi-quantitative and in situ analysis of gangliosides in brain. *Sci. Rep.* **2016,** *6*, 25289.

190. Chan, K.; Lanthier, P.; Liu, X.; Sandhu, J. K.; Stanimirovic, D.; Li, J., MALDI mass spectrometry imaging of gangliosides in mouse brain using ionic liquid matrix. *Anal. Chim. Acta* **2009,** *639* (1–2), 57-61.

191. Colsch, B.; Woods, A. S., Localization and imaging of sialylated glycosphingolipids in brain tissue sections by MALDI mass spectrometry. *Glycobiology* **2010,** *20* (6), 661-667.

192. Sekiya, S.; Wada, Y.; Tanaka, K., Derivatization for Stabilizing Sialic Acids in MALDI-MS. *Anal. Chem.* **2005,** *77* (15), 4962-4968.

193. de Haan, N.; Reiding, K. R.; Haberger, M.; Reusch, D.; Falck, D.; Wuhrer, M., Linkage-Specific Sialic Acid Derivatization for MALDI-TOF-MS Profiling of IgG Glycopeptides. *Anal. Chem.* **2015,** *87* (16), 8284-8291.

194. O'Connor, P. B.; Mirgorodskaya, E.; Costello, C. E., High pressure matrix-assisted laser desorption/ionization fourier transform mass spectrometry for minimization of ganglioside fragmentation1. *J. Am. Soc. Mass. Spectrom.* **2002,** *13* (4), 402-407.

195. Zhang, J.; LaMotte, L.; Dodds, E. D.; Lebrilla, C. B., Atmospheric Pressure MALDI Fourier Transform Mass Spectrometry of Labile Oligosaccharides. *Anal. Chem.* **2005,** *77* (14), 4429-4438.

196. Jackson, S. N.; Colsch, B.; Egan, T.; Lewis, E. K.; Schultz, J. A.; Woods, A. S., Gangliosides' analysis by MALDI-ion mobility MS. *Analyst* **2011,** *136* (3), 463-466.

197. Škrášková, K.; Claude, E.; Jones, E. A.; Towers, M.; Ellis, S. R.; Heeren, R. M. A., Enhanced capabilities for imaging gangliosides in murine brain with matrix-assisted laser desorption/ionization and desorption electrospray ionization mass spectrometry coupled to ion mobility separation. *Methods* **2016,** *104*, 69-78.

198. Eberlin, L. S.; Ferreira, C. R.; Dill, A. L.; Ifa, D. R.; Cooks, R. G., Desorption electrospray ionization mass spectrometry for lipid characterization and biological tissue imaging. *Biochim. Biophys. Acta Mol. Cell. Biol. Lipids* **2011,** *1811* (11), 946-960.

199. Orth, A.; Ghosh, R. N.; Wilson, E. R.; Doughney, T.; Brown, H.; Reineck, P.; Thompson, J. G.; Gibson, B. C., Super-multiplexed fluorescence microscopy via photostability contrast. *Biomed. Opt. Express* **2018,** *9* (7), 2943-2954.

200. Hofman, P.; Badoual, C.; Henderson, F.; Berland, L.; Hamila, M.; Long-Mira, E.; Lassalle, S.; Roussel, H.; Hofman, V.; Tartour, E.; Ilié, M., Multiplexed Immunohistochemistry for Molecular and Immune Profiling in Lung Cancer-Just About Ready for Prime-Time? *Cancers* **2019,** *11* (3), 283.

201. Goltsev, Y.; Samusik, N.; Kennedy-Darling, J.; Bhate, S.; Hale, M.; Vazquez, G.; Black, S.; Nolan, G. P., Deep Profiling of Mouse Splenic Architecture with CODEX Multiplexed Imaging. *Cell* **2018,** *174* (4), 968-981.e15.

202. Baharlou, H.; Canete, N. P.; Cunningham, A. L.; Harman, A. N.; Patrick, E., Mass Cytometry Imaging for the Study of Human Diseases—Applications and Data Analysis Strategies. *Frontiers in Immunology* **2019,** *10* (2657).

203. Buchberger, A. R.; DeLaney, K.; Johnson, J.; Li, L., Mass Spectrometry Imaging: A Review of Emerging Advancements and Future Insights. *Anal. Chem.* **2018,** *90* (1), 240-265.

204. Chaurand, P.; Schwartz, S. A.; Reyzer, M. L.; Caprioli, R. M., Imaging Mass Spectrometry: Principles and Potentials. *Toxicol. Pathol.* **2005,** *33* (1), 92-101.

205. Dufresne, M.; Guneysu, D.; Patterson, N. H.; Marcinkiewicz, M. M.; Regina, A.; Demeule, M.; Chaurand, P., Multimodal detection of GM2 and GM3 lipid species in the brain of mucopolysaccharidosis type II mouse by serial imaging mass spectrometry and immunohistochemistry. *Anal. Bioanal. Chem.* **2017,** *409* (5), 1425-1433.

206. Prentice, B. M.; Caprioli, R. M., The Need for Speed in Matrix-Assisted Laser Desorption/Ionization Imaging Mass Spectrometry. *Postdoc J.* **2016,** *4* (3), 3-13.

207. Boughton, B. A.; Thomas, O. R. B.; Demarais, N. J.; Trede, D.; Swearer, S. E.; Grey, A. C., Detection of small molecule concentration gradients in ocular tissues and humours. *Journal of Mass Spectrometry* **2020,** *55* (5), e4460.

208. Sans, M.; Feider, C. L.; Eberlin, L. S., Advances in mass spectrometry imaging coupled to ion mobility spectrometry for enhanced imaging of biological tissues. *Curr. Opin. Chem. Biol.* **2018,** *42*, 138-146.

209. Gessel, M. M.; Norris, J. L.; Caprioli, R. M., MALDI imaging mass spectrometry: Spatial molecular analysis to enable a new age of discovery. *J. Proteomics* **2014,** *107*, 71-82.

210. Garden, R. W.; Sweedler, J. V., Heterogeneity within MALDI Samples As Revealed by Mass Spectrometric Imaging. *Anal. Chem.* **2000,** *72* (1), 30-36.

211. Zavalin, A.; Todd, E. M.; Rawhouser, P. D.; Yang, J.; Norris, J. L.; Caprioli, R. M., Direct imaging of single cells and tissue at sub-cellular spatial resolution using transmission geometry MALDI MS. *Journal of Mass Spectrometry* **2012,** *47* (11), i-i.

212. Heien, M. L.; Piehowski, P. D.; Winograd, N.; Ewing, A. G., Lipid Detection, Identification, and Imaging Single Cells with SIMS. In *Mass Spectrometry Imaging: Principles and Protocols*, Rubakhin, S. S.; Sweedler, J. V., Eds. Humana Press: Totowa, NJ, 2010; pp 85-97.

213. Niehaus, M.; Soltwisch, J.; Belov, M. E.; Dreisewerd, K., Transmission-mode MALDI-2 mass spectrometry imaging of cells and tissues at subcellular resolution. *Nat. Methods* **2019,** *16* (9), 925-931.

214. Chaurand, P.; Norris, J. L.; Cornett, D. S.; Mobley, J. A.; Caprioli, R. M., New Developments in Profiling and Imaging of Proteins from Tissue Sections by MALDI Mass Spectrometry. *J. Proteome Res.* **2006,** *5* (11), 2889-2900.

215. Angel, P. M.; Spraggins, J. M.; Baldwin, H. S.; Caprioli, R., Enhanced Sensitivity for High Spatial Resolution Lipid Analysis by Negative Ion Mode Matrix Assisted Laser Desorption Ionization Imaging Mass Spectrometry. *Anal. Chem.* **2012,** *84* (3), 1557-1564.

216. Wang, H.-Y. J.; Post, S. N. J. J.; Woods, A. S., A minimalist approach to MALDI imaging of glycerophospholipids and sphingolipids in rat brain sections. *Int. J. Mass Spectrom.* **2008,** *278* (2), 143-149.

217. Huang, X.; Zhan, L.; Sun, J.; Xue, J.; Liu, H.; Xiong, C.; Nie, Z., Utilizing a Mini-Humidifier To Deposit Matrix for MALDI Imaging. *Anal. Chem.* **2018,** *90* (14), 8309-8313.

218. Puolitaival, S. M.; Burnum, K. E.; Cornett, D. S.; Caprioli, R. M., Solvent-free matrix dry-coating for MALDI imaging of phospholipids. *J. Am. Soc. Mass. Spectrom.* **2008,** *19* (6), 882-886.

219. Van Nuffel, S.; Elie, N.; Yang, E.; Nouet, J.; Touboul, D.; Chaurand, P.; Brunelle, A., Insights into the MALDI Process after Matrix Deposition by Sublimation Using 3D ToF-SIMS Imaging. *Anal. Chem.* **2018,** *90* (3), 1907-1914.

220. Spraggins, J. M.; Rizzo, D. G.; Moore, J. L.; Noto, M. J.; Skaar, E. P.; Caprioli, R. M., Next-generation technologies for spatial proteomics: Integrating ultra-high speed MALDI-TOF and high mass resolution MALDI FTICR imaging mass spectrometry for protein analysis. *Proteomics* **2016,** *16* (11-12), 1678-1689.

221. Perry, W. J.; Patterson, N. H.; Prentice, B. M.; Neumann, E. K.; Caprioli, R. M.; Spraggins, J. M., Uncovering matrix effects on lipid analyses in MALDI imaging mass spectrometry experiments. *Journal of Mass Spectrometry* **2020,** *55* (4), e4491.

222. Thiele, H.; Heldmann, S.; Trede, D.; Strehlow, J.; Wirtz, S.; Dreher, W.; Berger, J.; Oetjen, J.; Kobarg, J. H.; Fischer, B.; Maass, P., 2D and 3D MALDI-imaging: Conceptual strategies for visualization and data mining. *Biochim. Biophys. Acta Proteins Protemocis* **2014,** *1844* (1, Part A), 117-137.

223. Schramm, T.; Hester, Z.; Klinkert, I.; Both, J.-P.; Heeren, R. M. A.; Brunelle, A.; Laprévote, O.; Desbenoit, N.; Robbe, M.-F.; Stoeckli, M.; Spengler, B.; Römpp, A., imzML — A common data format for the flexible exchange and processing of mass spectrometry imaging data. *J. Proteomics* **2012,** *75* (16), 5106-5110.

224. Bemis, K. D.; Harry, A.; Eberlin, L. S.; Ferreira, C.; van de Ven, S. M.; Mallick, P.; Stolowitz, M.; Vitek, O., Cardinal: an R package for statistical analysis of mass spectrometry-based imaging experiments. *Bioinformatics* **2015,** *31* (14), 2418-2420.

225. Bokhart, M. T.; Nazari, M.; Garrard, K. P.; Muddiman, D. C., MSiReader v1.0: Evolving Open-Source Mass Spectrometry Imaging Software for Targeted and Untargeted Analyses. *J. Am. Soc. Mass. Spectrom.* **2018,** *29* (1), 8-16.

226. Källback, P.; Nilsson, A.; Shariatgorji, M.; Andrén, P. E., msIQuant – Quantitation Software for Mass Spectrometry Imaging Enabling Fast Access, Visualization, and Analysis of Large Data Sets. *Anal. Chem.* **2016,** *88* (8), 4346-4353.

227. Chaurand, P.; Fouchécourt, S.; DaGue, B. B.; Xu, B. J.; Reyzer, M. L.; Orgebin-Crist, M.-C.; Caprioli, R. M., Profiling and imaging proteins in the mouse epididymis by imaging mass spectrometry. *Proteomics* **2003,** *3* (11), 2221-2239.

228. OuYang, C.; Chen, B.; Li, L., High Throughput In Situ DDA Analysis of Neuropeptides by Coupling Novel Multiplex Mass Spectrometric Imaging (MSI) with Gas-Phase Fractionation. *J. Am. Soc. Mass. Spectrom.* **2015,** *26* (12), 1992-2001.

229. Zhang, Y.; Buchberger, A.; Muthuvel, G.; Li, L., Expression and distribution of neuropeptides in the nervous system of the crab Carcinus maenas and their roles in environmental stress. *Proteomics* **2015,** *15* (23-24), 3969-3979.

230. Cerruti, C. D.; Touboul, D.; Guérineau, V.; Petit, V. W.; Laprévote, O.; Brunelle, A., MALDI imaging mass spectrometry of lipids by adding lithium salts to the matrix solution. *Anal. Bioanal. Chem.* **2011,** *401* (1), 75-87.

231. Hankin, J. A.; Murphy, R. C., Relationship between MALDI IMS Intensity and Measured Quantity of Selected Phospholipids in Rat Brain Sections. *Anal. Chem.* **2010,** *82* (20), 8476-8484.

232. Wang, H.-Y. J.; Liu, C. B.; Wu, H.-W., A simple desalting method for direct MALDI mass spectrometry profiling of tissue lipids. *J. Lipid Res.* **2011,** *52* (4), 840-849.

233. Meisenbichler, C.; Doppler, C.; Bernhard, D.; Müller, T., Improved matrix coating for positive- and negative-ion-mode MALDI-TOF imaging of lipids in blood vessel tissues. *Anal. Bioanal. Chem.* **2019,** *411* (15), 3221-3227.

234. Sugiura, Y.; Setou, M., Selective imaging of positively charged polar and nonpolar lipids by optimizing matrix solution composition. *Radid Commun. Mass Sp.* **2009,** *23* (20), 3269-3278.

235. Griffiths, R. L.; Bunch, J., A survey of useful salt additives in matrix-assisted laser desorption/ionization mass spectrometry and tandem mass spectrometry of lipids: introducing nitrates for improved analysis. *Radid Commun. Mass Sp.* **2012,** *26* (13), 1557-1566.

236. Jackson, S. N.; Wang, H.-Y. J.; Woods, A. S., In situ structural characterization of phosphatidylcholines in brain tissue using MALDI-MS/MS. *J. Am. Soc. Mass. Spectrom.* **2005,** *16* (12), 2052-2056.

237. Penn, S. G.; Cancilla, M. T.; Green, M. K.; Lebrilla, C. B., Direct Comparison of Matrix-Assisted Laser Desorption/Ionisation and Electrospray Ionisation in the Analysis of Gangliosides by Fourier Transform Mass Spectrometry. *Eur J Mass Spectrom (Chichester).* **1997,** *3* (1), 67-79.

238. Sun, G.; Yang, K.; Zhao, Z.; Guan, S.; Han, X.; Gross, R. W., Matrix-Assisted Laser Desorption/Ionization Time-of-Flight Mass Spectrometric Analysis of Cellular Glycerophospholipids Enabled by Multiplexed Solvent Dependent Analyte−Matrix Interactions.

Anal. Chem. **2008,** *80* (19), 7576-7585.

239. Dufresne, M.; Masson, J.-F.; Chaurand, P., Sodium-Doped Gold-Assisted Laser Desorption Ionization for Enhanced Imaging Mass Spectrometry of Triacylglycerols from Thin Tissue Sections. *Anal. Chem.* **2016,** *88* (11), 6018-6025.

240. Acter, T.; Solihat, N. N.; Kim, S.; Uddin, N.; Mustafa, A. I.; Shamsuddin, S. M.; Kim, S., Application of silver-assisted laser desorption ionization ultrahigh-resolution mass spectrometry for the speciation of sulfur compounds. *Anal. Bioanal. Chem.* **2020,** *412* (1), 243-255.

241. Jaber, A. J.; Wilkins, C. L., Hydrocarbon Polymer Analysis by External MALDI Fourier Transform and Reflectron Time of Flight Mass Spectrometry. *J. Am. Soc. Mass. Spectrom.* **2005,** *16* (12), 2009-2016.

242. Choi, S.-S.; Ha, S.-H., Influence of sample preparation method and silver salt types on MALDI-TOFMS analysis of polybutadiene. *Macromol. Res.* **2008,** *16* (2), 108-112.

243. Ding, F.; Qian, Y.; Deng, Z.; Zhang, J.; Zhou, Y.; Yang, L.; Wang, F.; Wang, J.; Zhou, Z.; Shen, J., Size-selected silver nanoparticles for MALDI-TOF mass spectrometry of amyloid-beta peptides. *Nanoscale* **2018,** *10* (46), 22044-22054.

244. Kliman, M.; Vijayakrishnan, N.; Wang, L.; Tapp, J. T.; Broadie, K.; McLean, J. A., Structural mass spectrometry analysis of lipid changes in a Drosophila epilepsy model brain. *Mol. Biosyst.* **2010,** *6* (6), 958-966.

245. Lloyd, T. E.; Taylor, J. P., Flightless Flies: Drosophila models of neuromuscular disease. *Ann. N. Y. Acad. Sci.* **2010,** *1184*, e1-20.

246. Bharucha, K. N., The Epicurean Fly: Using Drosophila Melanogaster to Study Metabolism. *Pediatr. Res.* **2009,** *65*, 132.

247. Perrimon, N.; Pitsouli, C.; Shilo, B. Z., Signaling mechanisms controlling cell fate and embryonic patterning. *Cold Spring Harb. Perspect. Biol.* **2012,** *4* (8), a005975.

248. Amstalden van Hove, E. R.; Smith, D. F.; Heeren, R. M. A., A concise review of mass spectrometry imaging. *J. Chromatogr. A* **2010,** *1217* (25), 3946-3954.

249. DeLaney, K.; Buchberger, A.; Li, L., Identification, Quantitation, and Imaging of the Crustacean Peptidome. In *Peptidomics: Methods and Strategies*, Schrader, M.; Fricker, L., Eds. Springer New York: New York, NY, 2018; pp 247-269.

250. Norris, J. L.; Caprioli, R. M., Analysis of Tissue Specimens by Matrix-Assisted Laser Desorption/Ionization Imaging Mass Spectrometry in Biological and Clinical Research. *Chem. Rev.* **2013,** *113* (4), 2309-2342.

251. DeKeyser, S. S.; Kutz-Naber, K. K.; Schmidt, J. J.; Barrett-Wilt, G. A.; Li, L., Imaging Mass Spectrometry of Neuropeptides in Decapod Crustacean Neuronal Tissues. *J. Proteome Res.* **2007,** *6* (5), 1782-1791.

252. McDonnell, L. A.; Piersma, S. R.; Altelaar, A. F. M.; Mize, T. H.; Luxembourg, S. L.; Verhaert, P. D. E. M.; van Minnen, J.; Heeren, R. M. A., Subcellular imaging mass spectrometry of brain tissue. *Journal of Mass Spectrometry* **2005,** *40* (2), 160-168.

253. Ye, H.; Greer, T.; Li, L., Probing neuropeptide signaling at the organ and cellular domains via imaging mass spectrometry. *J. Proteomics* **2012,** *75* (16), 5014-5026.

254. Bhandari, D. R.; Schott, M.; Römpp, A.; Vilcinskas, A.; Spengler, B., Metabolite localization by atmospheric pressure high-resolution scanning microprobe matrix-assisted laser desorption/ionization mass spectrometry imaging in whole-body sections and individual organs of the rove beetle Paederus riparius. *Anal. Bioanal. Chem.* **2015,** *407* (8), 2189-2201.

255. Verhaert, P. D. E. M.; Pinkse, M. W. H.; Strupat, K.; Conaway, M. C. P., Imaging of Similar Mass Neuropeptides in Neuronal Tissue by Enhanced Resolution MALDI MS with an Ion Trap – OrbitrapTM Hybrid Instrument. In *Mass Spectrometry Imaging: Principles and Protocols*, Rubakhin, S. S.; Sweedler, J. V., Eds. Humana Press: Totowa, NJ, 2010; pp 433-449.

256. Wang, T.-H.; Jian, C.-H.; Hsieh, Y.-K.; Wang, F.-N.; Wang, C.-F., Spatial Distributions of Inorganic Elements in Honeybees (Apis mellifera L.) and Possible Relationships to Dietary Habits and Surrounding Environmental Pollutants. *J. Agric. Food Chem.* **2013,** *61* (21), 5009-5015.

257. Millet-Boureima, C.; Porras Marroquin, J.; Gamberi, C., Modeling Renal Disease "On the Fly". *BioMed Res. Int.* **2018,** *2018*, 13.

258. Chen, R.; Hui, L.; Sturm, R. M.; Li, L., Three Dimensional Mapping of Neuropeptides and Lipids in Crustacean Brain by Mass Spectral Imaging. *J. Am. Soc. Mass. Spectrom.* **2009,** *20* (6), 1068-1077.

259. Bemis, K. D.; Harry, A.; Eberlin, L. S.; Ferreira, C. R.; van de Ven, S. M.; Mallick, P.; Stolowitz, M.; Vitek, O., Probabilistic Segmentation of Mass Spectrometry (MS) Images Helps Select Important Ions and Characterize Confidence in the Resulting Segments. *Mol. Cell. Proteomics* **2016,** *15* (5), 1761-1772.

260. Patterson, N. H.; Yang, E.; Kranjec, E. A.; Chaurand, P., Co-registration and analysis of multiple imaging mass spectrometry datasets targeting different analytes. *Bioinformatics* **2019,** *35* (7), 1261-1262.

261. Shaler, T. A.; Wickham, J. N.; Sannes, K. A.; Wu, K. J.; Becker, C. H., Effect of Impurities on the Matrix-Assisted Laser Desorption Mass Spectra of Single-Stranded Oligodeoxynucleotides. *Anal. Chem.* **1996,** *68* (3), 576-579.

262. Zimmerman, T. A.; Rubakhin, S. S.; Sweedler, J. V., MALDI Mass Spectrometry Imaging of Neuronal Cell Cultures. *J. Am. Soc. Mass. Spectrom.* **2011,** *22* (5), 828.

263. Chintapalli, V. R.; Al Bratty, M.; Korzekwa, D.; Watson, D. G.; Dow, J. A. T., Mapping an Atlas of Tissue-Specific Drosophila melanogaster Metabolomes by High Resolution Mass Spectrometry. *PLoS One* **2013,** *8* (10), e78066.

264. Brand, A. H.; Perrimon, N., Targeted gene expression as a means of altering cell fates and generating dominant phenotypes. *Development* **1993,** *118* (2), 401-15.

265. Patterson, N. H.; Thomas, A.; Chaurand, P., Monitoring time-dependent degradation of phospholipids in sectioned tissues by MALDI imaging mass spectrometry. *Journal of Mass spectrometry* **2014,** *49* (7), 622-7.

266. Kolter, T., Ganglioside Biochemistry. *ISRN Biochem.* **2012,** *2012*, 36.

267. Lopez, P. H. H.; Schnaar, R. L., Gangliosides in cell recognition and membrane protein regulation. *Curr. Opin. Chem. Biol.* **2009,** *19* (5), 549-557.

268. Chen, Y.; Allegood, J.; Liu, Y.; Wang, E.; Cachón-González, B.; Cox, T. M.; Merrill, A. H.; Sullards, M. C., Imaging MALDI Mass Spectrometry Using an Oscillating Capillary Nebulizer Matrix Coating System and Its Application to Analysis of Lipids in Brain from a Mouse Model of Tay−Sachs/Sandhoff Disease. *Anal. Chem.* **2008,** *80* (8), 2780-2788.

269. Walkley, S. U., Secondary accumulation of gangliosides in lysosomal storage disorders. *Semin. Cell Dev. Biol.* **2004,** *15* (4), 433-444.

270. Kolter, T.; Sandhoff, K., Sphingolipid metabolism diseases. *Biochim Biophys Acta Biomembr* **2006,** *1758* (12), 2057-2079.

271. Yanagisawa, K., GM1 ganglioside and Alzheimer's disease. *Glycoconj. J.* **2015,** *32* (3), 87-91.

272. Kaya, I.; Brinet, D.; Michno, W.; Syvänen, S.; Sehlin, D.; Zetterberg, H.; Blennow, K.; Hanrieder, J., Delineating Amyloid Plaque Associated Neuronal Sphingolipids in Transgenic Alzheimer's Disease Mice (tgArcSwe) Using MALDI Imaging Mass Spectrometry. *ACS Chem. Neurosci.* **2017,** *8* (2), 347-355.

273. Robert, K. Y.; Usuki, S.; Ariga, T., Ganglioside molecular mimicry and its pathological roles in Guillain-Barre syndrome and related diseases. *Infect. Immun.* **2006,** *74* (12), 6517-6527.

274. Navid, F.; Santana, V. M.; Barfield, R. C., Anti-GD2 Antibody Therapy for GD2-expressing Tumors. *Curr Cancer Drug Targets* **2010,** *10* (2), 200-209.

275. Ravindranath, M. H.; Muthugounder, S.; Presser, N., Ganglioside signatures of primary and nodal metastatic melanoma cell lines from the same patient. *Melanoma Res.* **2008,** *18* (1), 47-55.

276. Battula, V. L.; Shi, Y.; Evans, K. W.; Wang, R.-Y.; Spaeth, E. L.; Jacamo, R. O.; Guerra, R.; Sahin, A. A.; Marini, F. C.; Hortobagyi, G., Ganglioside GD2 identifies breast cancer stem cells and promotes tumorigenesis. *J. Clin. Invest.* **2012,** *122* (6), 2066-2078.

277. Chen, Y.; Allegood, J.; Liu, Y.; Wang, E.; Cachon-Gonzalez, B.; Cox, T. M.; Merrill, A. H., Jr.; Sullards, M. C., Imaging MALDI mass spectrometry using an oscillating capillary nebulizer matrix coating system and its application to analysis of lipids in brain from a mouse

model of Tay-Sachs/Sandhoff disease. *Anal. Chem.* **2008,** *80* (8), 2780-8.

278. Weishaupt, N.; Caughlin, S.; Yeung, K. K. C.; Whitehead, S. N., Differential Anatomical Expression of Ganglioside GM1 Species Containing d18:1 or d20:1 Sphingosine Detected by MALDI Imaging Mass Spectrometry in Mature Rat Brain. *Front. Neuroanat.* **2015,** *9*, 155.

279. Zarei, M.; Bindila, L.; Souady, J.; Dreisewerd, K.; Berkenkamp, S.; Müthing, J.; Peter‐Katalinić, J., A sialylation study of mouse brain gangliosides by MALDI a‐TOF and o‐TOF mass spectrometry. *Journal of Mass Spectrometry* **2008,** *43* (6), 716-725.

280. Nagahori, N.; Abe, M.; Nishimura, S.-I., Structural and functional glycosphingolipidomics by glycoblotting with an aminooxy-functionalized gold nanoparticle. *Biochemistry* **2008,** *48* (3), 583-594.

281. Colsch, B.; Jackson, S. N.; Dutta, S.; Woods, A. S., Molecular Microscopy of Brain Gangliosides: Illustrating their Distribution in Hippocampal Cell Layers. *ACS Chem. Neurosci.* **2011,** *2* (4), 213-222.

282. Caughlin, S.; Park, D. H.; Yeung, K. K.; Cechetto, D. F.; Whitehead, S. N., Sublimation of DAN Matrix for the Detection and Visualization of Gangliosides in Rat Brain Tissue for MALDI Imaging Mass Spectrometry. *J. Vis. Exp.* **2017,** (121).

283. Karlsson, O.; Michno, W.; Ransome, Y.; Hanrieder, J., MALDI imaging delineates hippocampal glycosphingolipid changes associated with neurotoxin induced proteopathy following neonatal BMAA exposure. *Biochim. Biophys. Acta Proteins Protemocis* **2016**.

284. Whitehead, S. N.; Chan, K. H. N.; Gangaraju, S.; Slinn, J.; Li, J.; Hou, S. T., Imaging Mass Spectrometry Detection of Gangliosides Species in the Mouse Brain following Transient Focal Cerebral Ischemia and Long-Term Recovery. *PLoS One* **2011,** *6* (6), e20808.

285. Dowlatshahi Pour, M.; Malmberg, P.; Ewing, A., An investigation on the mechanism of sublimed DHB matrix on molecular ion yields in SIMS imaging of brain tissue. *Anal. Bioanal. Chem.* **2016,** *408* (12), 3071-3081.

286. Svennerholm, L.; Fredman, P., A procedure for the quantitative isolation of brain gangliosides. *Biochim. Biophys. Acta Lipids Lipid Metab.* **1980,** *617* (1), 97-109.

287. Domon, B.; Costello, C. E., Structure elucidation of glycosphingolipids and gangliosides using high-performance tandem mass spectrometry. *Biochemistry* **1988,** *27* (5), 1534-1543.

288. Manzanares-Meza, L. D.; Gutiérrez-Román, C. I.; Medina-Contreras, O., MALDI imaging: beyond classic diagnosis. *Boletín Médico del Hospital Infantil de México* **2017,** *74* (3), 212-218.

289. Yang, E.; Dufresne, M.; Chaurand, P., Enhancing ganglioside species detection for MALDI-TOF imaging mass spectrometry in negative reflectron mode. *Int. J. Mass Spectrom.* **2019,** *437*, 3-9.

290. Chen, C.-T.; Chen, Y.-C., Molecularly Imprinted TiO2-Matrix-Assisted Laser

Desorption/Ionization Mass Spectrometry for Selectively Detecting α-Cyclodextrin. *Anal. Chem.* **2004,** *76* (5), 1453-1457.

291. Cheng, Y.-H.; Chen, W.-C.; Chang, S. Y., Rapid determination of rivaroxaban in human urine and serum using colloidal palladium surface-assisted laser desorption/ionization mass spectrometry. *Radid Commun. Mass Sp.* **2015,** *29* (21), 1977-1983.

292. McAlpin, C. R.; Voorhees, K. J., Extension of metal oxide laser ionization mass spectrometry to analytes with varied chemical functionalities. *Radid Commun. Mass Sp.* **2013,** *27* (15), 1763-1768.

293. Li, Z.; Zhang, Y.-W.; Xin, Y.-L.; Bai, Y.; Zhou, H.-H.; Liu, H.-W., A lithium-rich composite metal oxide used as a SALDI-MS matrix for the determination of small biomolecules. *Chem. Commun.* **2014,** *50* (97), 15397-15399.

294. Ozawa, T.; Osaka, I.; Hamada, S.; Murakami, T.; Miyazato, A.; Kawasaki, H.; Arakawa, R., Direct Imaging Mass Spectrometry of Plant Leaves Using Surface-assisted Laser Desorption/Ionization with Sputter-deposited Platinum Film. *Anal. Sci.* **2016,** *32* (5), 587-591.

295. Shi, C. Y.; Deng, C. H., Recent advances in inorganic materials for LDI-MS analysis of small molecules. *Analyst* **2016,** *141* (10), 2816-2826.

296. Francis, A. W., Liquid Complexes of Lower Olefins with Anhydrous Metal Salts1. *J. Am. Chem. Soc.* **1951,** *73* (8), 3709-3713.

297. Seal, J. R.; Porter, N. A., Liquid chromatography coordination ion-spray mass spectrometry (LC–CIS–MS) of docosahexaenoate ester hydroperoxides. *Anal. Bioanal. Chem.* **2004,** *378* (4), 1007-1013.

298. Kahr, M. S.; Wilkins, C. L., Silver nitrate chemical ionization for analysis of hydrocarbon polymers by laser desorption fourier transform mass spectrometry. *J. Am. Chem. Soc.* **1993,** *4* (6), 453-460.

299. Rentel, C.; Strohschein, S.; Albert, K.; Bayer, E., Silver-Plated Vitamins: A Method of Detecting Tocopherols and Carotenoids in LC/ESI-MS Coupling. *Anal. Chem.* **1998,** *70* (20), 4394-4400.

300. Havrilla, C. M.; Hachey, D. L.; Porter, N. A., Coordination (Ag+) Ion Spray−Mass Spectrometry of Peroxidation Products of Cholesterol Linoleate and Cholesterol Arachidonate: High-Performance Liquid Chromatography−Mass Spectrometry Analysis of Peroxide Products from Polyunsaturated Lipid Autoxidation. *J. Am. Chem. Soc.* **2000,** *122* (33), 8042-8055.

301. Milne, G. L.; Porter, N. A., Separation and identification of phospholipid peroxidation products. *Lipids* **2001,** *36* (11), 1265-1275.

302. Boutreau, L.; Léon, E.; Salpin, J.-Y.; Amekraz, B.; Moulin, C.; Tortajada, J., Gas-Phase Reactivity of Silver and Copper Coordinated Monosaccharide Cations Studied by Electrospray Ionization and Tandem Mass Spectrometry. *Eur J Mass Spectrom (Chichester).* **2003,** *9* (4), 377-

390.

303. Zhang, J.; Brodbelt, J. S., Silver Complexation and Tandem Mass Spectrometry for Differentiation of Isomeric Flavonoid Diglycosides. *Anal. Chem.* **2005,** *77* (6), 1761-1770.

304. Lorente, E.; Berrueco, C.; Herod, A. A.; Millan, M.; Kandiyoti, R., The detection of high-mass aliphatics in petroleum by matrix-assisted laser desorption/ionisation mass spectrometry. *Radid Commun. Mass Sp.* **2012,** *26* (14), 1581-1590.

305. Jackson, A. U.; Shum, T.; Sokol, E.; Dill, A.; Cooks, R. G., Enhanced detection of olefins using ambient ionization mass spectrometry: Ag+ adducts of biologically relevant alkenes. *Anal. Bioanal. Chem.* **2011,** *399* (1), 367-376.

306. Duncan, K. D.; Fang, R.; Yuan, J.; Chu, R. K.; Dey, S. K.; Burnum-Johnson, K. E.; Lanekoff, I., Quantitative Mass Spectrometry Imaging of Prostaglandins as Silver Ion Adducts with Nanospray Desorption Electrospray Ionization. *Anal. Chem.* **2018,** *90* (12), 7246-7252.

307. Patti, G. J.; Shriver, L. P.; Wassif, C. A.; Woo, H. K.; Uritboonthai, W.; Apon, J.; Manchester, M.; Porter, F. D.; Siuzdak, G., Nanostructure-initiator mass spectrometry (NIMS) imaging of brain cholesterol metabolites in Smith-Lemli-Opitz syndrome. *Neuroscience* **2010,** *170* (3), 858-864.

308. Patterson, N. H.; Doonan, R. J.; Daskalopoulou, S. S.; Dufresne, M.; Lenglet, S.; Montecucco, F.; Thomas, A.; Chaurand, P., Three-dimensional imaging MS of lipids in atherosclerotic plaques: Open-source methods for reconstruction and analysis. *Proteomics* **2016,** *16* (11-12), 1642-1651.

309. Gustafsson, O. J. R.; Guinan, T. M.; Rudd, D.; Kobus, H.; Benkendorff, K.; Voelcker, N. H., Metabolite mapping by consecutive nanostructure and silver-assisted mass spectrometry imaging on tissue sections. *Radid Commun. Mass Sp.* **2017,** *31* (12), 991-1000.

310. Leclerc, D.; Christensen, K. E.; Cauvi, O.; Yang, E.; Fournelle, F.; Bahous, R. H.; Malysheva, O. V.; Deng, L.; Wu, Q.; Zhou, Z.; Gao, Z.-H.; Chaurand, P.; Caudill, M. A.; Rozen, R., Mild Methylenetetrahydrofolate Reductase Deficiency Alters Inflammatory and Lipid Pathways in Liver. *Mol. Nutr. Food Res.* **2019,** *63* (3), 1801001.

311. Lauzon, N.; Dufresne, M.; Beaudoin, A.; Chaurand, P., Forensic analysis of latent fingermarks by silver-assisted LDI imaging MS on nonconductive surfaces. *Journal of Mass Spectrometry* **2017,** *52* (6), ii-ii.

312. Lauzon, N.; Chaurand, P., Detection of exogenous substances in latent fingermarks by silver-assisted LDI imaging MS: perspectives in forensic sciences. *Analyst* **2018,** *143* (15), 3586-3594.

313. Moule, E. C.; Guinan, T. M.; Gustafsson, O. J. R.; Kobus, H.; Kirkbride, K. P.; Voelcker, N. H., Silver-assisted development and imaging of fingermarks on non-porous and porous surfaces. *Int. J. Mass Spectrom.* **2017,** *422*, 27-31.

314. Schnapp, A.; Niehoff, A.-C.; Koch, A.; Dreisewerd, K., Laser desorption/ionization mass spectrometry of lipids using etched silver substrates. *Methods* **2016,** *104*, 194-203.

315. Hayasaka, T.; Goto-Inoue, N.; Zaima, N.; Shrivas, K.; Kashiwagi, Y.; Yamamoto, M.; Nakamoto, M.; Setou, M., Imaging mass spectrometry with silver naeoparticles reveals the distribution of fatty acids in mouse retinal sections. *J. Am. Soc. Mass. Spectrom.* **2010,** *21* (8), 1446-1454.

316. Jackson, S. N.; Baldwin, K.; Muller, L.; Womack, V. M.; Schultz, J. A.; Balaban, C.; Woods, A. S., Imaging of lipids in rat heart by MALDI-MS with silver nanoparticles. *Anal. Bioanal. Chem.* **2014,** *406* (5), 1377-1386.

317. Muller, L.; Baldwin, K.; Barbacci, D. C.; Jackson, S. N.; Roux, A.; Balaban, C. D.; Brinson, B. E.; McCully, M. I.; Lewis, E. K.; Schultz, J. A.; Woods, A. S., Laser Desorption/Ionization Mass Spectrometric Imaging of Endogenous Lipids from Rat Brain Tissue Implanted with Silver Nanoparticles. *J. Am. Soc. Mass. Spectrom.* **2017,** *28* (8), 1716-1728.

318. Groseclose, M. R.; Castellino, S., A Mimetic Tissue Model for the Quantification of Drug Distributions by MALDI Imaging Mass Spectrometry. *Anal. Chem.* **2013,** *85* (21), 10099-10106.

319. Gibb, S.; Strimmer, K., MALDIquant: a versatile R package for the analysis of mass spectrometry data. *Bioinformatics* **2012,** *28* (17), 2270-2271.

320. Heath, R. R.; Tumlinson, J. H.; Doolittle, R. E.; Duncan, J. H., Analytical and Preparative Separation of Geometrical Isomers by High Efficiency Silver Nitrate Liquid Chromatography1. *J. Chromatogr. Sci.* **1977,** *15* (1), 10-13.

321. Takino, M.; Daishima, S.; Yamaguchi, K.; Nakahara, T., Determination of polycyclic aromatic hydrocarbons by liquid chromatography–electrospray ionization mass spectrometry using silver nitrate as a post-column reagent. *J. Chromatogr. A* **2001,** *928* (1), 53-61.

322. Morita, M.; Mihashi, S.; Itokawa, H.; Hara, S., Silver nitrate impregnation of preparative silica gel columns for liquid chromatography. *Anal. Chem.* **1983,** *55* (2), 412-414.

323. Adlof, R.; List, G., Analysis of triglyceride isomers by silver-ion high-performance liquid chromatography: Effect of column temperature on retention times. *J. Chromatogr. A* **2004,** *1046* (1), 109-113.

324. Herling, J.; Shabtai, J.; Gil-Av, E., Gas chromatography with stationary phases containing silver nitrate: III. Isomeric C8 and C9 cyclohexenes and p-menthenes. *J. Chromatogr. A* **1962,** *8*, 349-354.

325. Muhs, M. A.; Weiss, F. T., Determination of Equilibrium Constants of Silver-Olefin Complexes Using Gas Chromatography. *J. Am. Chem. Soc.* **1962,** *84* (24), 4697-4705.

326. Moreda, W.; Pérez-Camino, M. C.; Cert, A., Gas and liquid chromatography of hydrocarbons in edible vegetable oils. *J. Chromatogr. A* **2001,** *936* (1), 159-171.

327. O'Rourke, M. B.; Djordjevic, S. P.; Padula, M. P., The quest for improved reproducibility in MALDI mass spectrometry. *Mass Spectrom Rev.* **2018,** *37* (2), 217-228.

328. McDonnell, L. A.; Angel, P. M.; Lou, S.; Drake, R. R., Chapter Eleven - Mass Spectrometry Imaging in Cancer Research: Future Perspectives. In *Advances in Cancer Research*, Drake, R. R.; McDonnell, L. A., Eds. Academic Press: 2017; Vol. 134, pp 283-290.

329. Arentz, G.; Mittal, P.; Zhang, C.; Ho, Y. Y.; Briggs, M.; Winderbaum, L.; Hoffmann, M. K.; Hoffmann, P., Chapter Two - Applications of Mass Spectrometry Imaging to Cancer. In *Advances in Cancer Research*, Drake, R. R.; McDonnell, L. A., Eds. Academic Press: 2017; Vol. 134, pp 27-66.

330. Goodwin, R. J. A.; Bunch, J.; McGinnity, D. F., Chapter Six - Mass Spectrometry Imaging in Oncology Drug Discovery. In *Advances in Cancer Research*, Drake, R. R.; McDonnell, L. A., Eds. Academic Press: 2017; Vol. 134, pp 133-171.

331. Ntshangase, S.; Mdanda, S.; Singh, S. D.; Naicker, T.; Kruger, H. G.; Baijnath, S.; Govender, T., Mass Spectrometry Imaging Demonstrates the Regional Brain Distribution Patterns of Three First-Line Antiretroviral Drugs. *ACS Omega* **2019,** *4* (25), 21169-21177.

332. Angel, P. M.; Mehta, A.; Norris-Caneda, K.; Drake, R. R., MALDI Imaging Mass Spectrometry of N-glycans and Tryptic Peptides from the Same Formalin-Fixed, Paraffin-Embedded Tissue Section. In *Tissue Proteomics: Methods and Protocols*, Sarwal, M. M.; Sigdel, T. K., Eds. Springer New York: New York, NY, 2018; pp 225-241.

333. Spraggins, J. M.; Djambazova, K. V.; Rivera, E. S.; Migas, L. G.; Neumann, E. K.; Fuetterer, A.; Suetering, J.; Goedecke, N.; Ly, A.; Van de Plas, R.; Caprioli, R. M., High-Performance Molecular Imaging with MALDI Trapped Ion-Mobility Time-of-Flight (timsTOF) Mass Spectrometry. *Anal. Chem.* **2019,** *91* (22), 14552-14560.

334. Barry, J. A.; Groseclose, M. R.; Castellino, S., Quantification and assessment of detection capability in imaging mass spectrometry using a revised mimetic tissue model. *Bioanalysis* **2019,** *11* (11), 1099-1116.

335. Villatoro, J.; Zühlke, M.; Riebe, D.; Riedel, J.; Beitz, T.; Löhmannsröben, H.-G., IR-MALDI ion mobility spectrometry. *Anal. Bioanal. Chem.* **2016,** *408* (23), 6259-6268.

336. Laremore, T. N.; Linhardt, R. J., Improved matrix-assisted laser desorption/ionization mass spectrometric detection of glycosaminoglycan disaccharides as cesium salts. *Radid Commun. Mass Sp.* **2007,** *21* (7), 1315-1320.

337. Kéki, S.; Deák, G.; Zsuga, M., Copper(I) chloride: a simple salt for enhancement of polystyrene cationization in matrix-assisted laser desorption/ionization mass spectrometry. *Radid Commun. Mass Sp.* **2001,** *15* (9), 675-678.

338. Harris, A.; Roseborough, A.; Mor, R.; Yeung, K. K. C.; Whitehead, S. N., Ganglioside Detection from Formalin-Fixed Human Brain Tissue Utilizing MALDI Imaging Mass Spectrometry. *J. Am. Soc. Mass. Spectrom.* **2020,** *31* (3), 479-487.

339. Patterson, N. H.; Tuck, M.; Van de Plas, R.; Caprioli, R. M., Advanced Registration and Analysis of MALDI Imaging Mass Spectrometry Measurements through Autofluorescence Microscopy. *Anal. Chem.* **2018,** *90* (21), 12395-12403.

340. Jones, M. A.; Cho, S. H.; Patterson, N. H.; Van de Plas, R.; Spraggins, J. M.; Boothby, M. R.; Caprioli, R. M., Discovering new lipidomic features using cell type specific fluorophore expression to provide spatial and biological specificity in a multimodal workflow with MALDI Imaging Mass Spectrometry. *Anal. Chem.* **2020**.

341. Erich, K.; Sammour, D. A.; Marx, A.; Hopf, C., Scores for standardization of on-tissue digestion of formalin-fixed paraffin-embedded tissue in MALDI-MS imaging. *Biochim. Biophys. Acta Proteins Protemocis* **2017,** *1865* (7), 907-915.

342. Palmer, A.; Phapale, P.; Chernyavsky, I.; Lavigne, R.; Fay, D.; Tarasov, A.; Kovalev, V.; Fuchser, J.; Nikolenko, S.; Pineau, C.; Becker, M.; Alexandrov, T., FDR-controlled metabolite annotation for high-resolution imaging mass spectrometry. *Nat. Methods* **2017,** *14* (1), 57-60.